

ISTANBUL TECHNICAL UNIVERSITY ★ INFORMATICS INSTITUTE

**COMPRESSED SENSING BASED
3D IMAGE RECONSTRUCTION IN DIGITAL BREAST TOMOSYNTHESIS
AND MICRO-BIOIMAGING**



Ph.D. THESIS

Adem POLAT

Department of Communication Systems

Satellite Communication and Remote Sensing Programme

MARCH 2018

ISTANBUL TECHNICAL UNIVERSITY ★ INFORMATICS INSTITUTE

**COMPRESSED SENSING BASED
3D IMAGE RECONSTRUCTION IN DIGITAL BREAST TOMOSYNTHESIS
AND MICRO-BIOIMAGING**



Ph.D. THESIS

**Adem POLAT
(705122001)**

Department of Communication Systems

Satellite Communication and Remote Sensing Programme

Thesis Advisor: Assoc. Prof. Dr. İsa YILDIRIM

MARCH 2018

İSTANBUL TEKNİK ÜNİVERSİTESİ ★ BİLİŞİM ENSTİTÜSÜ

**SAYISAL MEME TOMOSENTEZİNDE VE MİKRO BİYOGÖRÜNTÜLEMEDE
SIKIŞTIRILMIŞ ALGILAMA TABANLI 3B GÖRÜNTÜ GERİ ÇATMA**



DOKTORA TEZİ

**Adem POLAT
(705122001)**

İletişim Sistemleri Anabilim Dalı

Uydu Haberleşmesi ve Uzaktan Algılama Programı

Tez Danışmanı: Doç. Dr. İsa YILDIRIM

MART 2018

Adem Polat, a **Ph.D.** student of ITU **Institute of Informatics** student ID 705122001, successfully defended the **thesis/dissertation** entitled “**COMPRESSED SENSING BASED 3D IMAGE RECONSTRUCTION IN DIGITAL BREAST TOMOSYNTHESIS AND MICRO-BIOIMAGING**”, which he prepared after fulfilling the requirements specified in the associated legislations, before the jury whose signatures are below.

Thesis Advisor : **Assoc. Prof. Dr. İsa YILDIRIM**
İstanbul Technical University

Jury Members : **Prof. Dr. Ahmet H. KAYRAN**
İstanbul Technical University

Assoc.Prof. Dr. E. Mete EKŞİOĞLU
İstanbul Technical University

Prof. Dr. Aydın AKAN
İzmir Kâtip Çelebi University

Prof. Dr. Nizamettin AYDIN
Yıldız Technical University

Date of Submission : 12 February 2018

Date of Defense : 23 March 2018





To my dad and my son,



FOREWORD

I wish to express my sincere gratitude to my supervisor, Assoc. Prof. Dr. İsa Yıldırım for trusting me with the assignment of this Ph.D. dissertation and for the opportunity to work with him with great expertise and long research activity in the field of breast tomosynthesis. I am grateful for his scientific guidance and support throughout my entire thesis.

I would like to express my great appreciation to steering committee and defense jury members Prof. Dr. Ahmet Hamdi Kayran, Assoc. Prof. Dr. Ender Mete Ekşiođlu, Prof. Dr. Aydın Akan, and Prof. Dr. Nizamettin Aydın for sharing with me their knowledge and experience.

I also would like to express my deepest gratitude to Prof. Dr. Ali Khademhosseini, for providing me working with international scientists from various disciplinary at Harvard Medical School and Harvard-MIT Health Science and Technology. In particular, I would like to thank Asst. Prof. Dr. Yu Shrike Zhang and Dr. Shabir Hassan for the insightful discussions on the project and giving me the chance to conduct the experimental work during the time I spent at Harvard Medical School and Harvard-MIT Health Science and Technology in Cambridge, Massachusetts, USA. I would also like to thank the members of the project, Luis Eduardo Oliver, Maryam Mostafaei, Siddharth Kumar, Dr. Xia Cao, Dr. Guoliang Ying, Milad Eyvazi Hesar, and Dr. Sasha Hoshian for their valuable contributions to the development of the project.

I am also grateful to Asst. Prof. Dr. Nuno Matela and Prof. Dr. Pedro Almeida, for inviting me to their research group to work with real breast phantoms and arranging me various raw data, images and projections of the real breast acquired via tomosynthesis equipment, and sharing knowledge with me during the time I spent at Institute of Biophysics and Biomedical Engineering (IBEB) of the University of Lisbon, Portugal.

I am also grateful to Dr. Metin Ertaş and Dr. Ana Margarida Mota for their valuable help and exchange of ideas.

Since this work was supported by TUBITAK, the Scientific and Research Council of Turkey, under the grant 1059B141600590, many thanks to all the members of the International Research Fellowship Program in TUBITAK.

Of course, I offer my endless thanks to Istanbul Technical University, always glad to be a member of this family, which has signature in every phase of my life.

Lastly and most of all I am very grateful to my all family, particularly to my deceased dad Fahri Polat (rest in peace), my mom Güllü Polat, my wife Buket Polat, and my son Çınar Ege Polat for their precious, endless and unique support of this Ph.D. thesis, as it is in every field of my whole life.

March 2018

Adem POLAT
(Ph.D., Electronics and
Communication Engineer)



TABLE OF CONTENTS

	<u>Page</u>
FOREWORD	ix
TABLE OF CONTENTS	xi
ABBREVIATIONS	xiii
LIST OF TABLES	xv
LIST OF FIGURES	xvii
SUMMARY	xxi
ÖZET	xxv
1. INTRODUCTION	1
1.1 Medical Imaging	1
1.1.1 Structural and functional imaging	1
1.1.2 Ionizing and non-ionizing imaging	2
1.1.3 Projection and tomography techniques in imaging.....	3
1.2 X-ray Technology	4
1.3 Computed Tomography (CT).....	5
1.4 Breast Cancer	6
1.4.1 Mammography	9
1.4.2 Digital breast tomosynthesis (DBT)	10
1.4.3 Radiation dose.....	13
2. AIM AND OBJECTIVE	15
3. LITERATURE REVIEW	17
4. THEORETICAL AND MATHEMATICAL BACKGROUND	21
4.1 The Mathematical Basis of Projections.....	21
4.1.1 Line integral	21
4.1.2 Radon transform.....	23
4.1.3 Siddon algorithm.....	25
4.2 Reconstruction Methods.....	30
4.2.1 Algebraic reconstruction technique (ART).....	30
4.3 Improvement and Optimization Methods	35
4.3.1 Compressed sensing	35
4.3.2 Total Variation (TV) minimization	38
4.3.3 Majorization-Minimization algorithm	41
5. DATA AND METHODOLOGY	43
5.1 Data and Methodology for Digital Breast Tomosynthesis (DBT)	43
5.1.1 A numeric matrix model and an analytical phantom	43
5.1.2 Real breast phantom and images.....	46
5.1.3 Algorithms to overcome out of memory and speed problems	48
5.2 Data and Methodology for Micro-Bioimaging (MBI)	50
5.2.1 Introduction to bioimaging.....	50
5.2.2 Imaging system for micro-bioimaging (MBI)	51
5.2.3 Creating the manual scanning 3D bioimaging tool.....	54
5.2.4 Creating the robotic 3D micro-bioimaging (MBI) tool	55
5.2.4.1 Mechanical design.....	56

5.2.4.2 Electronics design	56
5.2.4.3 Software implementation	57
5.2.5 Lab-on-a-chip	58
5.2.6 Biological phantoms.....	58
5.3 The Metrics for Quantitative Evaluation	59
6. RESULTS AND DISCUSSION.....	63
6.1 Results and Discussion for Digital Breast Tomosynthesis (DBT)	63
6.1.1 The results of IRT methods (ART, ART+TV _{3D} , and ART+TV _{3D} +MM) for an analytical phantom	63
6.1.2 The results of IRT methods (ART, ART+TV _{3D} , ART+TV _{3D} +MM) and FBP for the real breast phantom images.....	66
6.1.2.1 Reconstruction of 100 mAs-dose images.....	66
6.1.2.2 Visual analysis of 100 mAS-dose images.....	68
6.1.2.3 Metric analysis of 100 mAS-dose images.....	70
6.1.2.4 Reconstruction of 12 dose-level-images	72
6.1.2.5 Visual analysis of 12 dose-level-images	72
6.1.2.6 Metric analysis of 12 dose-level-images.....	75
6.2 Results and Discussion for Micro-Bioimaging (MBI)	79
6.2.1 Reconstruction by manual scanning 3D bioimaging tool	79
6.2.2 Reconstruction by robotic 3D micro-bioimaging (MBI) tool	80
7. CONCLUSION.....	83
8. FUTURE WORKS	85
REFERENCES	87
APPENDICES	93
APPENDIX A.....	95
CURRICULUM VITAE.....	101

ABBREVIATIONS

ACR	: American College of Radiology
ACS	: American Cancer Society
App	: Appendix
ART	: Algebraic Reconstruction Technique
ART+TV_{3D}	: Algebraic Reconstruction Technique + 3-Dimensional Total Variation
ART+TV_{3D}+MM	: Algebraic Reconstruction Technique + 3-Dimensional Total Variation + Majorization-Minimization
BP	: Back Projection
BT	: Bilgisayarlı Tomografi
CAD	: Computer-Aided Detection
CAT	: Computed Axial Tomography
CDP	: Contrast Detail Performance
CDS	: Contrast Detail Studies
CLMS	: Confocal Laser Scanning Microscopes
CMOS	: Complementary Metal Oxide Semiconductor
CNC	: Computer Numerical Control
CNR	: Contrast to Noise Ratio
CS	: Compressed Sensing
CT	: Computed Tomography
DBT	: Digital Breast Tomosynthesis
DQE	: Detective Quantum Efficiency
DRLs	: Diagnostic Reference Levels
EJR	: European Journal of Radiology
EM	: Expectation-Maximization
FBP	: Filtered Back Projection
FDA	: Food and Drug Administration
FDM	: Fused Deposition Modeling
FFDM	: Full-Field Digital Mammography
FL	: Focal Length
fMRI	: Functional Magnetic Resonance Imaging
FOV	: Field of View
GUI	: Graphical User Interface
HRRT	: High Resolution Research Tomograph
IARC	: International Agency for Research on Cancer
ICRP	: International Commission on Radiological Protection
LED	: Light Emitted Diode
LOC	: Lab-on-a-chip
LOI	: Layer of Interest
MA	: Massachusetts
mA	: milliamper
mAs	: milliamper-second
MBG	: Mikro-Biyogörüntüleme
MBI	: Micro-Bioimaging

MEG	: Magnetoencephalography
MIT	: Massachusetts Institute of Technology
μm	: micrometer
mGy	: milligray
ML	: Maximum-Likelihood
MM	: Majorization-Minimization
MQSA	: Mammography Quality Standard Act
MRG	: Manyetik Rezonans Görüntüleme
MRI	: Magnetic Resonance Imaging
MSSIM	: Mean Structure SIMilarity
MTF	: Modulation Transfer Function
NBCF	: National Breast Cancer Foundation
nm	: nanometer
OOI	: Object of Interest
PDMS	: Polydimethylsiloxane
PET	: Positron Emission Tomography
PICCS	: Prior Image Constrained Compressed Sensing
PMMA	: Polymethylmethacrylate
PSNR	: Peak Signal to Noise Ratio
ROF	: Rudin, Osher, and Fatemi
ROI	: Region of Interest
SAA	: Shift and Add
SART	: Simultaneous Algebraic Reconstruction Technique
SD	: Standard-definition
SEER	: The Surveillance, Epidemiology, and End Results
SIRT	: Simultaneous Iterative Reconstruction Technique
SMT	: Sayısal Meme Tomosentezi
SNR	: Signal to Noise Ratio
SPECT	: Single Photon Emission Computed Tomography
SSIM	: Structural SIMilarity
TV	: Total Variation
TV_{3D}	: 3-Dimensional Total Variation
USA	: The United States of America
V	: Volts
VGA	: Video Graphics Array
WHO	: World Health Organization
1D	: 1-Dimensional
2D	: 2-Dimensional
3D	: 3-Dimensional

LIST OF TABLES

	<u>Page</u>
Table 5.1 : The basic specifications of the lens.....	53
Table 5.2 : The specifications of Logitech C160 CMOS.....	54
Table 6.1 : The CNR values of FBP and the three methods of IRT at 100 mAs	70
Table A.1: The types of iterative reconstruction techniques.....	99





LIST OF FIGURES

	<u>Page</u>
Figure 1.1 : Ionizing (X-ray, computed tomography, mammography, nuclear scintigraphy) and non-ionizing (magnetic resonance) imaging.....	2
Figure 1.2 : Projection (radiography, angiography, planar scintigraphy) and tomographic (magnetic resonance, computed tomography, echocardiography) techniques	3
Figure 1.3 : A model of computed tomography (left), a real computed tomography (right)	6
Figure 1.4 : Normal breast tissue	8
Figure 1.5 : Incidence of the most common 10 types of cancer in women, Turkey, 2006-2008	8
Figure 1.6 : The illustration of mammography (left); a picture of mammography implementation (right)	10
Figure 1.7 : Schematic view of digital breast tomosynthesis.....	11
Figure 1.8 : A tomosynthesis equipment	12
Figure 1.9 : Tissues that overlap in conventional mammography (left) and hide pathologies (blue lesion) are less likely to be obscured using DBT (right)	12
Figure 1.10 : Principle of shift-and-add (SAA) tomosynthesis	13
Figure 4.1 : The 1D projection at angle θ	22
Figure 4.2 : Parallel beam geometry. Each projection is made up of the set of line integrals through the object.....	22
Figure 4.3 : Projections of the object taken from different angles.....	23
Figure 4.4 : The pixels of CT array (left), the intersection areas of orthogonal sets of equally spaced parallel lines (right)	25
Figure 4.5 : Geometric representation of a ray on the 2D image grid	26
Figure 4.6 : Reconstruction methods.	31
Figure 4.7 : A schematic view of the iterative reconstruction process	31
Figure 4.8 : The illustration of calculating of weight factor a_{ij} in ART algorithm ..	33
Figure 4.9 : Improvement and optimization methods	35
Figure 4.10 : Flowcart of the CS-based algorithm (ART+TV _{3D}) for DBT reconstruction.....	40
Figure 4.11 : Convergence criterion for inner iteration of MM algorithm	42
Figure 5.1 : The schematic of the simulation of Siddon's matlab implementation .	44
Figure 5.2 : The geometry of DBT system of Siemens MAMMOMAT.	47
Figure 5.3 : 3D image reconstruction of biological applications.....	51
Figure 5.4 : The concept of 3D bioimaging system for micro-scale biological applications. The acquisition of projections was done between -25 and +25 degrees with 5-degree angle step.....	52
Figure 5.5 : Optical imaging design.....	52
Figure 5.6 : Achromatic lens.....	53
Figure 5.7 : Logitech C160 CMOS.....	53

Figure 5.8 : Manual scanning tool. Between -45 and +45 degrees with 5 degree angle step.....	54
Figure 5.9 : The animation (left) and photo (right) of the robotic 3D micro-bioimaging (MBI) tool	55
Figure 5.10 : a. Arduino Mega 2560 R3 (ATMEGA1280 combo) and RAMPS 1.4 board, b. stepper motor, c. linear motor and d. power supply.....	55
Figure 5.11 : A4988 stepper motor driver.....	57
Figure 5.12 : A variety of biological phantoms in transparent media produced by PDMS.....	58
Figure 5.13 : Sylgard-184 kit	59
Figure 6.1 : Nine layers of the mimic of a 3D breast (61x61x9)	63
Figure 6.2 : a. Original LOI, b. the reconstructed LOI via ART, c. the reconstructed LOI via ART+TV _{3D} , and d. the reconstructed LOI via ART+TV _{3D} +MM	64
Figure 6.3 : SNR values (dB) of 3D volume for ART, ART+TV _{3D} , and ART+TV _{3D} +MM	65
Figure 6.4 : SSIM values of ART, ART+TV _{3D} , and ART+TV _{3D} +MM	66
Figure 6.5 : The reference projection (601x472 pixels), the four OOIs and 1D profiles at 100 mAs-dose level at the angle of 0.29°	67
Figure 6.6 : 1st projection at angle of -25.19° (left), 14th projection at angle of 0.29° (center), and 25th projection at angle of 21.77° (right).....	67
Figure 6.7 : a. FBP, b-d. IRT (b. ART, c. ART+TV _{3D} , and d. ART+TV _{3D} +MM) at 100 mAs	68
Figure 6.8 : Zoom in OOI-1 at 100 mAs-reconstructed images; FBP and IRT (ART, ART+TV _{3D} , and ART+TV _{3D} +MM).....	69
Figure 6.9 : Zoom in OOI-2 at 100 mAs-reconstructed images; FBP and IRT (ART, ART+TV _{3D} , and ART+TV _{3D} +MM).....	70
Figure 6.10 : ROI-1 (yellow), background of ROI-1 (black), ROI-2 (red), and background of ROI-2 (green).....	71
Figure 6.11 : 1D profiles-A of FBP and IRT (ART, ART+TV _{3D} , and ART+TV _{3D} +MM)	72
Figure 6.12 : FBP (1st row), ART (2nd row), ART+TV _{3D} (3rd row), and ART+TV _{3D} +MM (4th row) at 56 mAs (left column) and 199 mAs (right column).	73
Figure 6.13 : Enlarged views of OOIs-2; FBP (1st column), ART (2nd column), ART+TV _{3D} (3rd column), and ART+TV _{3D} +MM (4th column) at three dose levels in mAs values of (56 (1st row), 100 (2nd row), and 199 (3rd row))	74
Figure 6.14 : Enlarged views of OOIs-4; FBP (1st column), ART (2nd column), ART+TV _{3D} (3rd column), and ART+TV _{3D} +MM (4th column) at three dose levels in mAs values of (56 (1st row), 100 (2nd row), and 199 (3rd row))	75
Figure 6.15 : CNR values of ROI-1 of FBP, ART, ART+TV _{3D} , and ART+TV _{3D} +MM at 12 dose levels	76
Figure 6.16 : CNR values of ROI-2 of FBP, ART, ART+TV _{3D} , and ART+TV _{3D} +MM at 12 dose levels	77
Figure 6.17 : 1D profiles-B at three dose levels for ART (dash) and ART+TV _{3D} (solid); highest dose-199 mAs (dark blue), lowest dose-56 mAs (light blue), and middle dose-100 mAs (red).....	78

Figure 6.18: 1D profiles-B at three dose levels for FBP (dash) and ART+TV _{3D} +MM (solid); highest dose-199 mAs (dark blue), lowest dose-56 mAs (light blue), and middle dose-100 mAs (red)	78
Figure 6.19: Reference projection of the PDMS phantom.....	79
Figure 6.20: Phantom looking from two different directions. Layer-3 and layer-38 of reconstructed images of the PDMS phantom.....	80
Figure 6.21: A biological phantom consisting of two different layers. Left: acquisition via CMOS with a mounted lens and ambient light; right: acquisition via CMOS with a separate lens and a light source.....	80
Figure 6.22: Layer 22 (left column) and Layer 34 (right column) of the reconstructed images of the biological phantom. Figures in the first row are the results of Matlab, in the second row are the results of ImageJ	81
Figure 6.23: 3D models of the reconstructed images of the biological phantom	82
Figure 8.1 : The demonstration of the ultimate goal of the project in MBI.....	85
Figure A.1 : FBP at 12 doses	95
Figure A.2 : ART at 12 doses	96
Figure A.3 : ART+TV _{3D} at 12 doses.....	97
Figure A.4 : ART+TV _{3D} +MM at 12 doses	98



COMPRESSED SENSING BASED 3D IMAGE RECONSTRUCTION IN DIGITAL BREAST TOMOSYNTHESIS AND MICRO-BIOIMAGING

SUMMARY

Breast cancer is the most commonly seen cancer type among women. Early diagnosis of breast cancer is considered as the best strategy to increase the lifetime and to reduce the mortality rate, treatment duration, and the cost. In the last two decades, mammography has been the most efficient and effective tool for early diagnosis of breast cancer. However, 2-dimensional (2D) mammography increases the false-positive and false-negative rates due to the limitation of overlapping tissues. Tomosynthesis has been introduced to reduce these limitations with its ability to provide (3-dimensional) 3D images of the breast. Recently, tomosynthesis has been actively in use clinically with a possible replacement of mammography in the near future. In literature, there have been numerous studies published on digital breast tomosynthesis (DBT).

DBT is a linear imaging modality which can be expressed as $\mathbf{Y}=\mathbf{A}\mathbf{X}$ in linear algebraic equation form that is a linear combination of the voxels which build up \mathbf{X} . In $\mathbf{Y}=\mathbf{A}\mathbf{X}$ form, \mathbf{Y} is the observed data or projection in vector form, \mathbf{A} is the system matrix that models ray tracing geometry in matrix form, and \mathbf{X} is the object that is desired to be reconstructed in vector form. The coefficients of the linear equations must be computed before any iterative reconstruction algorithm is applied. To implement algebraic reconstruction technique (ART), one of iterative reconstruction technique (IRT) or any IRT, Siddon's 3D ray tracing algorithm can be used to build up the matrix \mathbf{A} in 3D image reconstruction.

The reconstruction methods used in DBT can be split into analytical and iterative techniques. Filtered back projection (FBP) which is an analytical and a conventional tomographic reconstruction technique shows inefficient results due to the lack of a number of projections though it is computationally very efficient. IRTs have been proposed in order to overcome this problem. In addition to the IRTs, regularization terms have been proposed in order to achieve the unique solution due to the highly under-determined problem in DBT reconstruction arose from limited view angle imaging geometry. Total variation (TV) has been the most commonly used term among these regularizations. Compressed sensing based application, TV_{3D} (3-dimensional total variation), is applied to ART ($ART+TV_{3D}$) to enhance the quality of the reconstructed image.

In this Ph.D. thesis, as the first project, we proposed an effective application of majorization-minimization (MM) based on 3D TV, called $ART+TV_{3D}+MM$ (compressed sensing based application) in iterative image reconstruction of DBT, and the effectiveness of the work has been shown using an analytical phantom and a real DBT images obtained at 12 different doses by Siemens MAMMOMAT.

Using a Siemens MAMMOMAT Inspiration system (Siemens AG, Healthcare Sector, Erlangen, Germany), we acquired 25 projections of the real breast phantom, CD Pasmam 1054 phantom (Southern Scientific Ltd, West Sussex, United Kingdom) at Hospital da Luz S.A., Lisbon, Portugal. The equipment acquired the projections with

short X-ray pulses at angles of the range of 47° with 28 kVp at 12 different levels of radiation doses in mAs.

We reconstructed the images of the analytical phantom with three iterative reconstruction methods: ART, ART+TV_{3D}, and ART+TV_{3D}+MM and compared the results both qualitatively and quantitatively. We then reconstructed the images of the real breast phantom with ART, ART+TV_{3D}, and ART+TV_{3D}+MM (IRT methods) and compared the results of the IRT methods with the results of MAMMOMAT's FBP method both qualitatively and quantitatively as well. Siemens MAMMOMAT reconstructs via its know-how unknown filtered back projection (FBP) method. We further aimed to investigate if compressed sensing based methods, ART+TV_{3D} and ART+TV_{3D}+MM, could help decrease the radiation dose which is one of the most critical limitations of DBT. We evaluated the performance of the methods for each experiment and phantom using visual assessment and quantitative metrics such as signal to noise ratio (SNR), structural similarity (SSIM), CNR (contrast to noise ratio), and 1-dimensional (1D) profiles. The visual interpretation was done by focusing on the different object of interests (OOIs) and region of interests (ROIs).

The first project of the Ph.D. thesis was performed at both Istanbul Technical University and Lisbon University.

3D imaging of the biological structures such as bioreactors, lab-on-a-chips (LOCs), cancer tissues, organoids, and spheroids is desired in many applications of the biomedical field such as bioimaging. However, in general, 2D microscopy techniques are used in bioimaging. Confocal microscopy, a promising method to produce 3D images, suffers from being very expensive, very difficult to access, and not easy to use. Having the intense experience of 3D image reconstruction in DBT has inspired us for creating a robotic 3D micro-bioimaging (MBI) tool.

For this purpose, which is the second project of this Ph.D. thesis, we developed the software algorithms for 3D image reconstruction and created a hardware, robotic 3D MBI tool, which is portable, cost-effective, and easy to use. We also manufactured several biological phantoms using polydimethylsiloxane (PDMS) as a transparent media to test the 3D image reconstruction performance of the tool.

The imaging and scanning tool for MBI had mainly three parts as modeling DBT: a complementary metal oxide semiconductor (CMOS) detector with a lens, a light source (can be a light emitted diode (LED)), and a holder or mini table for the biological sample. As CMOS image detector, Logitech C160 CMOS was used. Before creating the robotic 3D MBI tool, the manual imaging and scanning tool was built using PMMA (polymethylmethacrylate) by a laser cutter. It was able to manually rotated between maximum -45° and $+45^\circ$ with 5° angle steps, which means it was able to acquire maximum 19 projections in an examination. After getting promising results via manual scanning imaging tool, we designed a robotic imaging and scanning tool (robotic 3D MBI tool) controlled automatically.

The mechanical part of the robotic 3D MBI tool was built from scratch according to the specifications that were needed for a smooth and precise image acquisition. The chassis of the structure was built from 20mm T-slotted black anodized aluminum, which provided enough support for the rotating axis. The T-slots were joint using aluminum corner brackets to ensure the integrity of the chassis and to have versatility in case the structure had to be changed. The design was based on a mix between a computer numerical control (CNC) machine and a 3D printer. The size of the robotic 3D MBI tool was 35cmx35cmx30cm. It was able to manually rotated between maximum -45° and $+45^\circ$ with 5° angle steps, which means it was able to acquire maximum 19 projections in an examination in a similar manner as the manual one.

The electronics part of the robotic 3D MBI tool was done by Arduino board/software and motor controls. It comprised of one CMOS imager, one lens, one Arduino Mega 2560 R3 board, one RAMPS 1.4 board, three motor drivers, one light source, two stepper motors, one linear motor, and one power supply. We also designed a more advanced optical imaging setup using a combination of optical table and tools compared to that of manual scanning tool. The microcontroller programming of motor control was done using both a C++ code compiler and Matlab™ Graphical User Interface (GUI).

Whereby this tool, we improved the precision of the geometry and the resolution quality of the acquired projections. We also reconstructed 3D images of the projections acquired via robotic 3D MBI tool using ART+TV_{3D} that we developed and suggested to investigate if the layers of a biological phantom and/or a biological sample such as bioreactor fabricated by PDMS could be distinguished.

This second project of the Ph.D. thesis was performed at Harvard Medical School and Harvard-MIT Health Science and Technology, Massachusetts Institute of Technology, MA, USA.

The ultimate goal of this research for MBI by developing advanced robotic 3D MBI tool will be to investigate how morphology differentiation and proliferation of the tumor is attained by the cells after putting in the hydrogel and to visualize the 3D images of the tumor slice by slice. We will study the changes that happen on a morphological level after the interaction of the tumor tissue with drugs inside a gel by 3D imaging layer by layer as well.



SAYISAL MEME TOMOSENTEZİNDE VE MİKRO BİYOGÖRÜNTÜLEMEDE SIKIŞTIRILMIŞ ALGILAMA TABANLI 3B GÖRÜNTÜ GERİ ÇATMA

ÖZET

Meme kanseri, dünyada kadınlar arasında görülen en yaygın kanser türüdür. Kanserlin erken teşhisi hastalığın tedavisinde çok önemli bir yer tutmaktadır. Erken teşhis araçlarından biri de görüntülemedir. Elektronik Mühendisliği açısından görüntüleme, görüntü geri çatma teknikleri ve görüntü işleme olarak ele alınmaktadır. Bu doktora tezinde, hızla gelişen görüntü geri çatma teknikleri ve görüntü işleme metodlarındaki yeni yaklaşımların kanserli hücre ve doku (örneğin meme kanseri) üzerine yapılan çalışma alanlarına uygulanması kapsamında iki ana proje çalışılmıştır. İlk proje olarak mevcut görüntü geri çatma algoritmalarının limitasyonları ve tıkanıklıkları göz önünde bulundurularak 12 radyasyon doz seviyesinde gerçek meme fantomu kullanılarak sayısal meme tomosentezinde (SMT) (digital breast tomosynthesis-DBT) sıkıştırılmış algılama tabanlı 3-boyutlu (3B) görüntü geri çatma yöntemleri geliştirilmiş ve önerilmiştir. İkinci proje kapsamında mikro biyogörüntüleme (micro-bioimaging) kanserli hücre kolonisi, tümör, kanserli doku, biyopsi, lab-on-a-chip gibi çeşitli biyolojik örnekleri açısız tarama yaparak 3B görüntüleyebilen 3B biyogörüntüleme cihazı (robotic 3D micro-bioimaging tool) geliştirilmiştir.

Hastalık tanı ve teşhisinde medikal görüntüleme önemli bir teknolojidir. Yapısal ve fonksiyonel görüntüleme olarak adlandırılan ve farklı amaçlar için kullanılan iki ana medikal görüntüleme sınıfı mevcuttur. Yapısal görüntüleme ile anatomik yapılar incelenir. Manyetik rezonans görüntüleme (MRG), Röntgen ve bilgisayarlı tomografi (BT) yapısal görüntüleme tekniklerinin en önemlileridir. Fonksiyonel görüntüleme ise insan vücudundaki özel bir fonksiyonu analiz eden bir tekniktir. En önemlileri Single Photon Emission Computed Tomography (SPECT) ve Positron Emission Tomography (PET)'dir.

Tomografi Yunan kökenli "tomos" (dilim) ve "graph" (tanımlama) kelimelerinin birleşiminden oluşmuştur. İngiliz mühendis Godfrey Hounsfield ve Güney Afrika doğumlu fizikçi Allan Cormack tarafından 1972 yılında geliştirilmiştir. Bu sebeple Hounsfield ve Cormack 1979 yılında Nobel Tıp Ödülü'ne layık görülmüşlerdir. Bilgisayarlı tomografi (BT), vücut içine girmeksizin vücut içini görüntülemek suretiyle çeşitli hastalıkların tanı ve teşhisinde kullanılmasıyla tıpta devrim yaratmıştır. Radyografinin bir formu olan BT günümüzde çok yaygın bir medikal görüntüleme uygulamasıdır. X-ışın kaynağının bir eksen etrafında döndürülmesiyle toplanan 2-boyutlu (2B) radyografik görüntülerden nesnenin 3B görüntüsü elde edilebilmektedir.

Ulusal Meme Kanseri Vakfının (NBCF: National Breast Cancer Foundation, Inc.) 2010 yılında yapmış olduğu araştırmaya göre her yıl kadınlar arasında 200.000 yeni meme kanseri vakası ve 40.000 ölüm yaşanmaktadır. Türkiye'de Sağlık Bakanlığının 2008 verilerine göre meme kanseri %41.6 oranıyla kadınlar arasında en sık görülen hastalık olmuştur. Bunu %15.3 ile tiroid, %13.5 ile kolorektal, %8.7 ile uterus korpusu, %8.4 ile trakea, akciğer ve bronş, %8 ile mide, %6.5 ile over, %4.7 ile non-hodgking

lenfoma, %4.4 ile uterus serviksi, %4.2 ile beyin ve diğer sinir sistemi kanserleri takip etmektedir.

Kadın meme dokusu süt üretme bezleri (lobules), süt taşıma kanalları (ducts) ve bağ dokusu (stroma) olmak üzere üç ana kısımdan meydana gelir. Bağ dokusu kan damarları, lenfatik damarlar ve yağ dokusunu çevreler. Bazı kanserler süt üretme bezlerinden başlarken (lobular cancers), çoğunluğu süt taşıma kanallarında (ductal cancers) meydana gelir.

Mamografi yönteminin, birçok avantajlarının yanında tanı görüntülemesinde yaklaşık %20 oranında kanserli hücreyi kaçırdığı tahmin edilmektedir. 2B görüntülemeden kaynaklı dokunun üst üste binme problemi mamografinin en büyük kısıtlarındandır. Sayısal meme tomosentezi (SMT) ise yüksek çözünürlüklü 3B görüntü elde etme imkânı sunan yeni görüntüleme yaklaşımıdır. Bu sayede SMT ile geleneksel mamografide karşılaşılan dokunun üst üste binme problemi nedeniyle dokular arasına gizlenen kanserli hücreler daha kolay algılanabilmektedir.

SMT'de plakalarla sıkıştırılan meme etrafında bir yay şeklinde ve genellikle 50 derecelik tarama açısı ile hareket eden X-ışın tüpünden gönderilen radyasyon meme altındaki detektöre düşürülerek memenin 2B projeksiyonları elde edilir. Uygulamalarda yaygın olarak SMT'de 11-60 derece tarama açısı ile 9-25 arasında projeksiyon elde edilir. Bu projeksiyonlar daha sonra çeşitli görüntü geri çatma yöntemleriyle geri çatılarak dilim dilim 3B geri çatılmış meme görüntüsü elde edilir. Böylece doku üst üste binmesi problemi nedeniyle meydana gelen yanlış pozitif ve yanlış negatif oranları azaltılabilir. SMT'nin radyasyon nedeniyle sınırlı açıda ve sınırlı sayıda tarama yapması ise dezavantajdır.

SMT $Y=AX$ lineer cebirsel denklem formu ile yazılabilen hedef nesnenin (X) 3B geri çatılmış görüntüsünü elde eden yenilikçi bir görüntüleme modelidir. $Y=AX$ formunda Y gözlenen veri (projeksiyon) vektörü, A ışın izleme geometrisini modelleyen sistem matrisi, X ise 3B görüntülenmesi istenen nesnenin vektör formunu göstermektedir. Lineer denklem katsayılarını içeren A sistem matrisi yinelemeli geri çatma algoritmasının uygulanması için elde edilmelidir. Geri çatılan 3B görüntü, sınırlı açıda ve sınırlı sayıda taramayla elde edilen 2B projeksiyonlardan elde edildiğinden *eksik veri problemi* olarak adlandırılan önemli bir kısıt ortaya çıkmaktadır. Bu kısıtı aşmak için ileri düzey 3B görüntü geri çatma algoritmalarının geliştirilmesine ihtiyaç duyulmaktadır.

Literatürde bir yinelemeli yöntem olan cebirsel geri çatma tekniğinin (algebraic reconstruction technique (ART)) ve bir analitik yöntem olan filtrelenmiş geri izdüşüm tekniğinin (filtered back projection (FBP)) SMT gibi ileri tıp teknolojisinde uygulandığından bahsedilmektedir.

Bu doktora tezinde ART ile 3B görüntü geri çatılmıştır. ART algoritmasında, $Y=AX$ formundaki, ışın izleme geometrisini modelleyen sistem matrisini (A) elde etmek için Siddon'un 3B ışın izleme algoritması kullanılmıştır. ART ile elde edilmiş geri çatılmış 3B görüntünün kalitesini arttırmak için sıkıştırılmış algılama tabanlı bir uygulama olan (compressed sensing based application) 3B toplam değişinti algoritması TV_{3D} (3-dimensional total variation) ART sonrası elde edilen geri çatılmış 3B görüntüye uygulanmıştır.

İlk projede iki ayrı alt çalışma yapılmıştır. İlk olarak 3B toplam değişinti temelli maksimizasyon-minimizasyon algoritması (majorization-minimization (MM) based on 3D total variation) yinelemeli görüntü geri çatma literatüründe yenilikçi bir yaklaşım olarak sunulmuştur (ART+ TV_{3D} +MM). İkinci olarak ART, ART+ TV_{3D} ve ART+ TV_{3D} +MM yöntemleri ile elde edilen geri çatılmış görüntüler 12 farklı radyasyon dozu için elde edilerek, sıkıştırılmış algılama tabanlı yinelemeli görüntü

geri çatma teknikleri olan ART+TV_{3D} algoritmasının ve bizim önerdiğimiz yeni ART+TV_{3D}+MM yönteminin hastaya uygulanan radyasyon dozunun azaltılabilmesi noktasında uygulanabilirliği araştırılmıştır. İlk proje kapsamında, Lizbon Üniversitesi da Luz S.A. hastanesinde Siemens MAMMOMAT Inspiration system (Siemens AG, Healthcare Sector, Erlangen, Germany) kullanılarak 12 farklı doz seviyesinde yaklaşık 47° açısal tarama aralığında 25 projeksiyonu alınan gerçek meme fantomu (CD Pasmam 1054) için ART, ART+TV_{3D} ve ART+TV_{3D}+MM uygulanarak 3B görüntüler elde edilmiş ve aynı fantomun Siemens MAMMOMAT cihazının filtrelenmiş geri izdüşüm tekniğiyle (FBP) elde edilen geri çatılmış görüntüleri ile kıyaslanmıştır. Siemens MAMMOMAT cihazında know-how'ı bilinmeyen bir filtreleme yöntemine sahip FBP kullanılmaktadır.

Sonuçların performansını karşılaştırmak amacıyla önce yinelemeli görüntü geri çatma tekniği olan (iterative reconstruction technique: IRT) ART, ART+TV_{3D} ve ART+TV_{3D}+MM bir analitik fantom için test edilmiştir. Sonuçlar niteliksel ve niceliksel olarak değerlendirilmiştir. Niceliksel değerlendirmede iki metrik olan sinyal-gürültü oranı (signal-to-noise ratio: SNR) ve yapısal benzerlik (structural similarity: SSIM) kullanılmıştır. Daha sonra, 12 dozda alınan CD Pasmam 1054 gerçek meme fantomu projeksiyonları için yinelemeli görüntü geri çatma tekniğinin üç yöntemi (ART, ART+TV_{3D} ve ART+TV_{3D}+MM) kullanılarak elde edilen geri çatılmış görüntüler ile Siemens MAMMOMAT cihazının filtrelenmiş geri izdüşüm tekniğiyle (FBP) elde edilen geri çatılmış görüntüler kıyaslanmıştır. Bu kısımdaki sonuçlar ise hem niteliksel hem de karşıtlık gürültü oranı (contrast to noise ratio (CNR) ve 1B profil değişimi metrikleriyle niceliksel olarak değerlendirilmiştir. İlk proje İstanbul Teknik Üniversitesi ve Lizbon Üniversitesi'nde gerçekleştirilmiştir.

İkinci projede, SMT'deki çalışmalardan elde ettiğimiz umut verici sonuçların verdiği ilhamla kanserli hücre kolonisi, tümör, kanserli doku, biyopsi, lab-on-a-chip gibi çeşitli biyolojik örnekleri 3B görüntüleyebilen robotik 3B biyogörüntüleme cihazı (robotic 3D micro-bioimaging tool) geliştirilmiştir. Tıp ve biyoloji alanlarında bilimsel araştırma yapılan merkezlerde kullanılabilecek olan cihazın avantajları arasında, ucuz, taşınabilir ve kullanımı kolay olması sıralanabilir. Bu cihaz donanım (mekanik, elektronik ve robotik kontrol kısımları) ve yazılım (robotik kontrol yazılımı ve 3B görüntü geri çatma yazılımı) olmak üzere iki aşamalı tasarlanmıştır.

Donanımsal olarak robotik 3B biyogörüntüleme cihazının ana mekanik çatkısı, dönme eksenine yeterli güç ve desteği sağlamak için 20 mm'lik T-oluklu eloksallı alüminyumdan 35cmx35cmx30cm boyutlarında üretilmiştir. Hassas hareket ve ölçümler için bazı parçalar 3B yazıcı ile üretilirken, bazıları ise polymethylmethacrylate (PMMA) malzeme kullanılarak CNC makine ve lazer kesici ile üretilmiştir. Elektronik ve robotik kontrol kısmı, bir Arduino Mega 2560 R3 kartı, bir RAMPS 1.4 kartı, Arduino yazılımla kontrol edilen iki adım motoru, bir lineer motor, üç motor sürücü ve bir güç kaynağından meydana gelmiştir. Optik görüntüleme kısmı ise bir metal oksit yarı iletken dedektör (complementary metal oxide semiconductor (CMOS) görüntüleyici, bir lens ve bir ışık kaynağından meydana gelmiştir. CMOS görüntüleyici dedektör olarak Logitech C160 kullanılmıştır. Optik görüntülemede hassas optik masa tasarımı sayesinde projeksiyon elde etme geometrisi ve görüntüleme kalitesi iyileştirilmiştir. -45° ve +45° açı aralığında tarama yapabilme yeteneğine sahip cihaz ile bu projede -25° ve +25° açı aralığında 5° açı adımıyla 11 projeksiyon elde edilmiş ve geri çatılmıştır.

Yazılımsal olarak ise açısal tarama ve üç boyutlu düzlemde eksen hareketlerini yapan robotik motor kontrollerin mikrokontrolör programlanması C++ kod derleyici ve Matlab grafiksel kullanıcı arayüzü ile yazılmıştır. 3B görüntüleme için ise sıkıştırılmış

algılama tabanlı yinelemeli 3B görüntü geri çatma yazılımı (ART+TV_{3D}) mikro-biyogörüntüleme (micro-bioimaging (MBI)) arařtırmalarında kullanılmak üzere revize edilerek geliştirilmiřtir.

Testlerde kullanılan biyolojik fantomlar transparan ortam saęlayan polydimethylsiloxane (PDMS) kullanılarak üretilmiřtir.

İkinci proje Harvard Medical School, Harvard-MIT Health Science and Technology ve Massachusetts Institute of Technology'de gerekleřtirilmiřtir.

Sonuç olarak, ilk projenin ilk kısmında ART+TV_{3D}+MM yönteminde analitik fantom için elde edilen sonuçların SSIM ve SNR deęerleri on iterasyon sonunda ART+TV_{3D} ve ART yöntemleriyle elde edilen aynı deęerlerden yüksek çıkmıřtır. Onuncu iterasyonda ART+TV_{3D}+MM'in SSIM ve SNR deęerleri sırasıyla 0.9814 ve 24.56 olurken, ART+TV_{3D}'in 0.9771 ve 24.32; ART'in ise 0.9208 ve 22.48 olmuřtur. Ayrıca ROI ve object of interest (OOI)'ler FBP ve ART'ye göre ART+TV_{3D} ve ART+TV_{3D}+MM yöntemlerinde görsel olarak daha net bir řekilde ayırt edilebilmiřtir. İlk projenin ikinci kısmında, 12 farklı doz seviyesi için ART+TV_{3D} ile elde edilen görüntülerde CNR deęerleri hem doz arttıkça artmıř, hem de aynı doz seviyesindeki ART'nin CNR deęerlerinden genel olarak yüksek çıkmıřtır. Örneęin en yüksek doz seviyesi olan 199 mAs doz seviyesinde, ROI-1 için FBP, ART, ART+TV_{3D} ve ART+TV_{3D}+MM'in CNR deęerleri sırasıyla 1.203, 54.621, 55.894 ve 56.443 olurken; ROI-2 için yine sırasıyla 2.188, 2.292, 2.364 ve 2.473 olmuřtur.

İkinci projede ise tasarlanan robotik 3B biyogörüntüleme cihazıyla laboratuvar ortamında üretilen biyolojik fantomların projeksiyonları deęiřik açılardan başarıyla alınmıřtır. ART+TV_{3D} yöntemiyle, bu projeksiyonlar 3B görüntü řeklinde geri çatılmıř ve bu biyolojik fantomlar başarılı bir řekilde dilim dilim görüntülenebilmiřtir. İki projede de alınan olumlu sonuçların gerek yinelemeli 3B görüntü geri çatmada yeni yaklařımların arařtırılması ve geliştirilmesi noktasında; gerekse tasarlanan robotik 3B biyogörüntüleme cihazının bilimsel arařtırma laboratuvarlarında, kanserli hücre ve doku alıřmaları ile bunlara karřı ilaç vb. geliřtirmek için yapılan tıbbi ve biyolojik arařtırmalarda kullanılan eřitli biyolojik numunelerin 3B görüntülenmesinin geliştirilmesi noktasında gelecekteki alıřmalara ışık tutacaęı düşünölmektedir.

1. INTRODUCTION

Medical imaging modalities can be classified based on different criteria as summarized in the following section.

1.1 Medical Imaging

Medical imaging is an important modality that visualizes invisible inner part of the body for medical diagnostic. Medical imaging can be grouped according to different scope of windows such as structural/functional (in terms of technologies), ionizing/nonionizing (using radiation), projection/tomographic (as techniques).

1.1.1 Structural and functional imaging

1. Structural imaging modalities show anatomical structures obtained from:

- *Magnetic Resonance Imaging (MRI)* is accepted as one of the most accurate imaging method and uses the magnetic field properties for the diagnosis.
- *X-rays* or the *radiography* uses the ionizing electromagnetic radiation.
- *Computed Tomography (CT)* uses the X-rays to acquire a slice image in a two-dimensional (2D) or a volume in a three-dimensional (3D) structure.

2. Functional imaging is a nuclear medicine technique that analyzes a specific function handled in a specific area of the human body.

- *Single Photon Emission Computed Tomography (SPECT)* uses γ -rays emitted after injection of a low dose radioactive agent into the patient for acquiring the image sections of the organs and tissues.
- *Positron Emission Tomography (PET)* produces a 3D image of functional changes occurring in organs and tissues followed by injecting radioactive agents in the body.

Each device has its advantages. MRI and CT give structural information whereas SPECT and PET provide functional information at the expense of low spatial resolution.

Nowadays, new modalities such as functional MRI (fMRI-used in neuroimaging) provide both structural and functional information. The goals of all imaging modalities are similar in general sense, for instance, to achieve getting medical images with high resolution and to reduce the number of artifacts (Ntalampeki, 2007).

1.1.2 Ionizing and non-ionizing imaging

Some of medical imaging techniques use ionizing radiation, whereas others use non-ionizing radiation. In the techniques, which use ionizing radiation, the images are created by the use of X-rays or gamma rays. Both X-rays and gamma rays are high energy, high frequency, and short wavelength (less than an angstrom) electromagnetic radiation that is capable of penetrating and passing through most tissues. (See Figure 1.1) (Url-1, 2015).

Tissues of greater thickness or higher atomic mass absorb differentially ionizing radiation, as it passes through the body (e.g. calcium has a higher atomic weight than hydrogen which is a major component of tissue water). Different portions of the body tissues attenuate differing amounts of the incident radiation. Attenuation of the ionizing radiation through the body makes the tissue atoms chemically reactive and damages the cells. Non-ionizing radiation techniques mainly use either radio waves combined with high-field magnets (e.g. magnetic resonance imaging) or acoustic pulses (ultrasound) for echo-ranging imaging (e.g. radar) (Url-1, 2015).

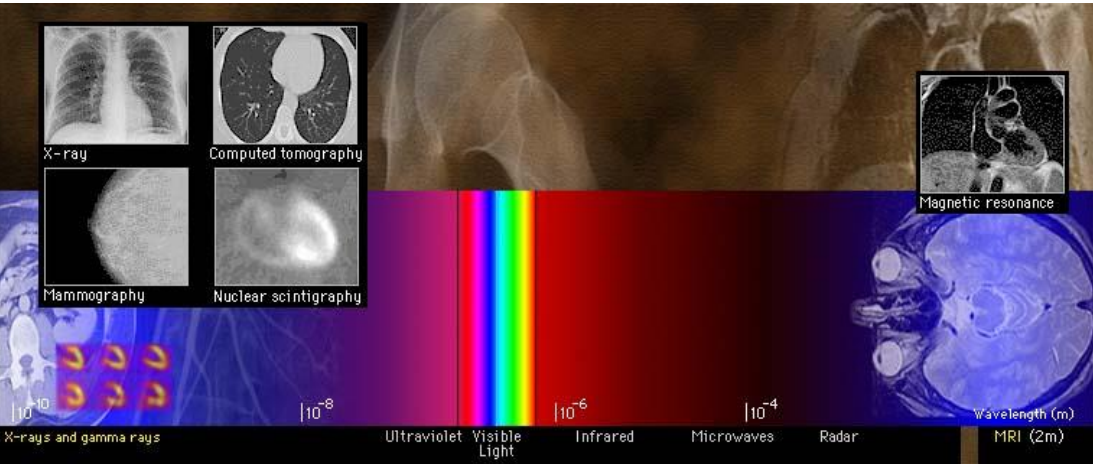


Figure 1.1 : Ionizing (X-ray, computed tomography, mammography, nuclear scintigraphy) and non-ionizing (magnetic resonance) imaging (Url-1, 2015).

1.1.3 Projection and tomography techniques in imaging

Medical images can be classified as tomographic techniques (magnetic resonance imaging (MRI), computed tomography (CT), and echocardiography) or projection techniques (radiography, angiography, and planar scintigraphy) based on volumetric and planar imaging (see Figure 1.2). Because of various tissues at different depths are overlapping each other and often need multiple views, the body needs to be transilluminated by projection techniques such as X-ray films which are shadowgram. Tomography is a slicing of the body into various sections with various view planes, and tomographic images are thin slices, which allow understanding the anatomy more clearly with less artifacts by avoiding the overlapping structures.

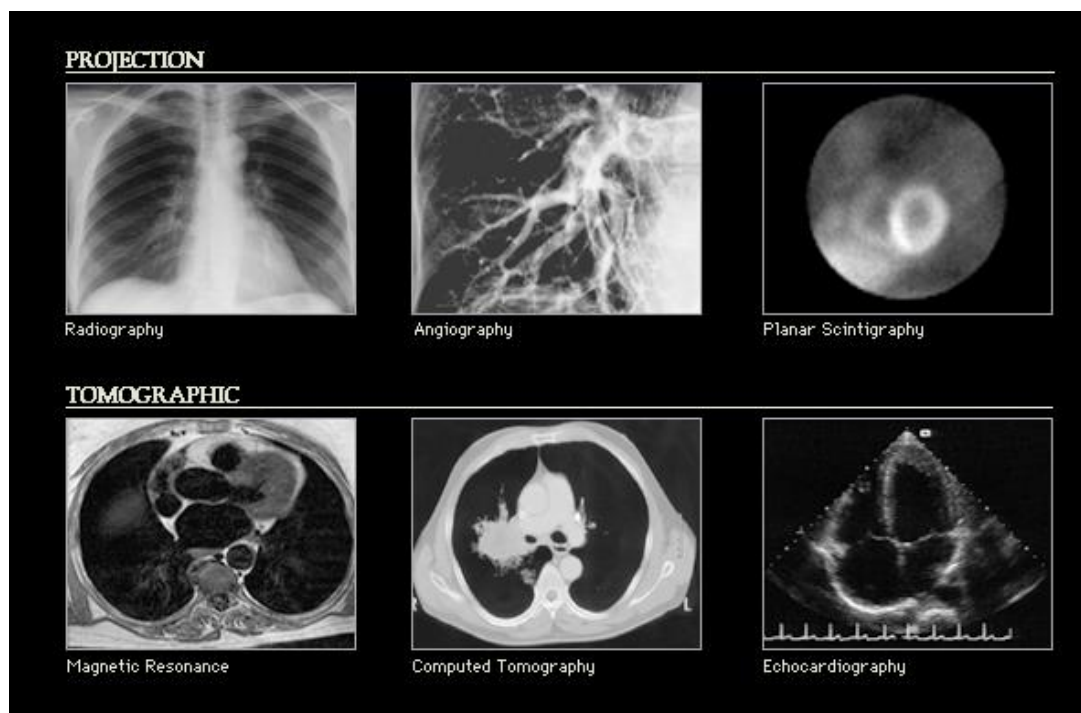


Figure 1.2 : Projection (radiography, angiography, planar scintigraphy) and tomographic (magnetic resonance, computed tomography, echocardiography) techniques (Url-1, 2015).

Tomographic sections are generated by X-rays in the case of computed tomography or ultrasound in the case of echocardiography, and then they are processed by a computer to allow the display and understanding of 3D anatomy (Url-1, 2015). Some of these modalities are used for screening purposes and some for diagnostic purposes. These imaging modalities are continually being developed to diagnose fatal diseases such as breast cancer as early as possible (Sree et al., 2011).

The currently used modalities to detect breast cancer include mammography, breast ultrasound, thermography, magnetic resonance imaging (MRI), positron emission tomography (PET), scintimammography, optical imaging, electrical impedance based imaging, and computed tomography (CT). Since cancer is a complex disease with various pathologies, many variations of the detection technique have been used in performing to improve the detection efficiency over the years (Sree et al., 2011).

Additionally, according to Yıldırım and Kamasak (2014) referenced by Edell and Eisen (1999) and Bick and Diekmann (2010), mammography is a medical imaging system which is mainly used in breast imaging today.

An ultrasound was a reference method for breast cancer diagnosis before mammography at early ages because it was a cheap and harmless technique. Since MRI is often used for the display of soft tissue; it may not give certain results to detect cancerous tissue. Likewise, although CT and PET devices potentially may be used in large amounts for breast imaging, they are not being able to use for diagnostic purposes due to high rate X-ray dose (Yıldırım & Kamasak, 2014). X-ray technology is described in Section 1.2 X-ray Technology.

Since mammography and digital breast tomosynthesis (DBT) are the most common modalities for detecting breast cancer, these methods are briefly explained in Section 1.4. Breast cancer.

CT is also briefly explained in Section 1.3 Computed Tomography (CT) since the fundamental of mathematical theory of tomography is applied to mammography and DBT as well.

1.2 X-ray Technology

X-rays have been highly useful diagnostically and backbone of medical imaging by both computed tomography and Roentgen films. X-ray imaging is a method of illuminating the body with a penetrating high-energy ionizing radiation. The different tissues of body that have various densities attenuate different amounts of this radiation. Less dense and lower atomic weight structures, such as lung, allow transmission of more radiation, and cause black areas on the film, while higher atomic weight structures (bone) absorb and block the radiation, and these areas appear white

(transparent) on the film. The differential pattern of X-ray radiation escaping the body creates the shadowgram on an X-ray film. Since overlapping nature of body structures is the main limitation of the projection techniques, in X-ray imaging often at least two views (e.g. PA and lateral) are required. (Url-1, 2015).

1.3 Computed Tomography (CT)

Tomography is from the Greek word "tomos" meaning slice or section and "graphia" meaning describing. British engineer Sir Godfrey Hounsfield and South Africa-born physicist Allan Cormack invented Computed Tomography (CT) in 1972 (Url-2, 2014).

Hounsfield and Cormack were awarded the Nobel Prize for their contributions to medicine and science in 1979. The Nobel Assembly of Karolinska Institutet decided to award the Nobel Prize in Physiology or Medicine for 1979 jointly to Allan M. Cormack and Godfrey Newbold Hounsfield for the "development of computer assisted tomography" (Url-2, 2014).

In terms of inspecting the body noninvasively, the invention of CT was a great revolution in diagnostic medicine. The 2D slice-based CT has been the most commonly used of CT technique in clinical operations for many years. However, the need for better visualization and more accuracy of the 3D or volumetric CT imaging have been motivating the science world to develop more efficient reconstruction approaches (Ntalampeki, 2007). CT was also called computerized tomography or computed axial tomography (CAT). X-ray CT consists of detectors, motorized table and an X-ray tube that rotates around the body (Figure 1.3). Specialized and computer processed X-ray equipment is used to produce cross-sectional images (tomographic images) of the body which represent slices of the patient being imaged allowing the user to see inside of the body without cutting. These tomographic images are used for various purposes such as intervention and screening, diagnosis, treatment planning, and therapy (Url-3, 2014). There is a picture of a real CT in Figure 1.3.

X-ray CT that is a form of radiography is the most common medical imaging application. A series of 2D radiographic images taken around a single axis of rotation are used to create a 3D image of an object by applying digital geometry processing. A volume of data produced by CT can be manipulated to demonstrate various structures of the body according to their ability to block the X-ray beam (Url-4, 2014).

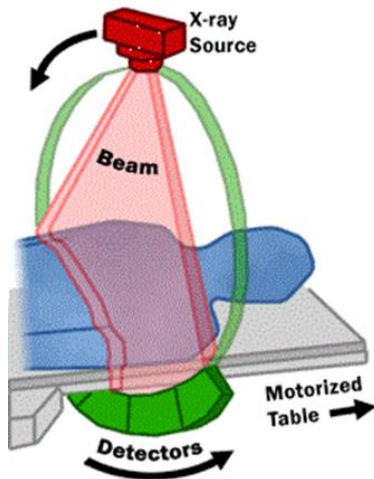


Figure 1.3 : A model of computed tomography (left), a real computed tomography (right) (Url-3, 2014).

1.4 Breast Cancer

Today, since the most common type of disease in women is breast cancer, researches about breast cancer are increasing rapidly. Because of high disease incidence among women, most of these researches are done in medical area.

According to World Health Organization (WHO) International Agency for Research on Cancer (IARC), 2008 (Available from: [http://globocan.iarc.fr/factsheets/populations/factsheet.asp? uno=900](http://globocan.iarc.fr/factsheets/populations/factsheet.asp?uno=900)) and WHO Fact sheet N297, 2009 (Available from: <http://www.who.int/mediacentre/factsheets/fs297/en/index.html>) referenced by Sree et.al., 2011, worldwide, breast cancer has 10.9% of cancer incidence in both men and women which is on second order of cancer types after lung cancer. Breast cancer is also the fifth common cause of cancer death (Sree et al., 2011).

National Breast Cancer Foundation, Inc. (NBCF), 2010 (Available from: <http://www.nationalbreastcancer.org/about-breast-cancer/what-is-breast-cancer.aspx>) is also referenced by Sree et.al., 2011 that it is estimated that around 200000 new breast cancer cases and 40000 deaths every year in women. In men, these statistics are 1700 and 450, respectively (Sree et al., 2011).

According to the statistics of the Surveillance, Epidemiology, and End Results (SEER) Cancer Statistics Review, 1975-2007, National Cancer Institute (Available from: http://seer.cancer.gov/csr/1975_2007/) referenced by Sree et.al., 2011 that it was estimated that 207090 new cases and 39840 deaths from breast cancer (only women)

were expected to occur in the United States, despite recent advances in treatment (Sree et al., 2011). The statistics inform that the early diagnosis of breast cancer was considered vital, because a five-year survival rate of 96% for those whose cancer was detected in the early stages (Sree et al., 2011).

According to some other researches, one of per 9 women is under the risk of breast cancer and breast cancer constitutes 23% of all female cancer that causes of women death. Breast cancer is a tumor genesis in mammary glands and milk ducts and starts in the breast cells. It is estimated that gene mutations and hereditary causes are the reasons of breast cancer (Sener, 2013; Sree et al., 2011). To comprehend the basics of breast cancer, the structure of the normal breast tissue must be understood clearly.

A female breast tissue includes three main sections, which are lobules, ducts, and stroma, shown in Figure 1.4. The lobules are milk-producing glands, ducts are tiny tubes that carry the milk from the lobules to the nipple, and stroma is fatty tissue and connective tissue surrounding the ducts and lobules, blood vessels, and lymphatic vessels. A majority of cancer begins in the ducts (ductal cancers), whereas some begins in the lobules (lobular cancers) (ACS, 2014).

The most well known and a reliable technique for detecting breast cancer is mammography. Since the breast is a very sensitive part of the body against radiation, the application time of radiation dose of diagnosis to acquire breast image should be minimum (Sener, 2013).

Physical factors such as system noise, compression of the breast, radiation scattering and motion artifacts affect the imaging quality. Additionally, because of the dense structure of the breast tissue, tumors in the breast may not be detected at younger ages. For these reasons, it is needed to improve the imaging techniques to detect breast tumors much better. Although mammography finds the traditional and wide application areas to sense tumors, due to overlapping of breast tissue, tumors can be hidden and cannot be detected in the processed image. One of the most popular study areas of the new detector technologies is digital breast tomosynthesis (DBT) to overcome these bottlenecks. The principle of 3D breast imaging of DBT is similar to digital mammography with C-Arm CT. DBT system structure is like CT and its imaging that generates cross sectional data sets is done with reconstruction methods in a short time (Sener, 2013).

In Turkey, according to the data taken from Ministry of Health Department of Cancer Control breast cancer has the highest rate as 41.6% incidence among women. The incidence of the other types of cancer is ordered as colorectal 15.3%, thyroid 13.5% and uterine-cervix 8.7% cancer (per 100.000), respectively in 2008 as shown in Figure 1.5 (Can, 2011).

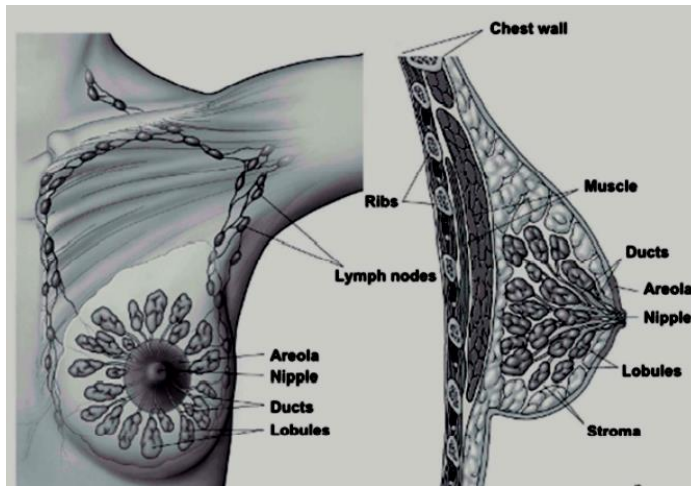


Figure 1.4 : Normal breast tissue (ACS, 2014).

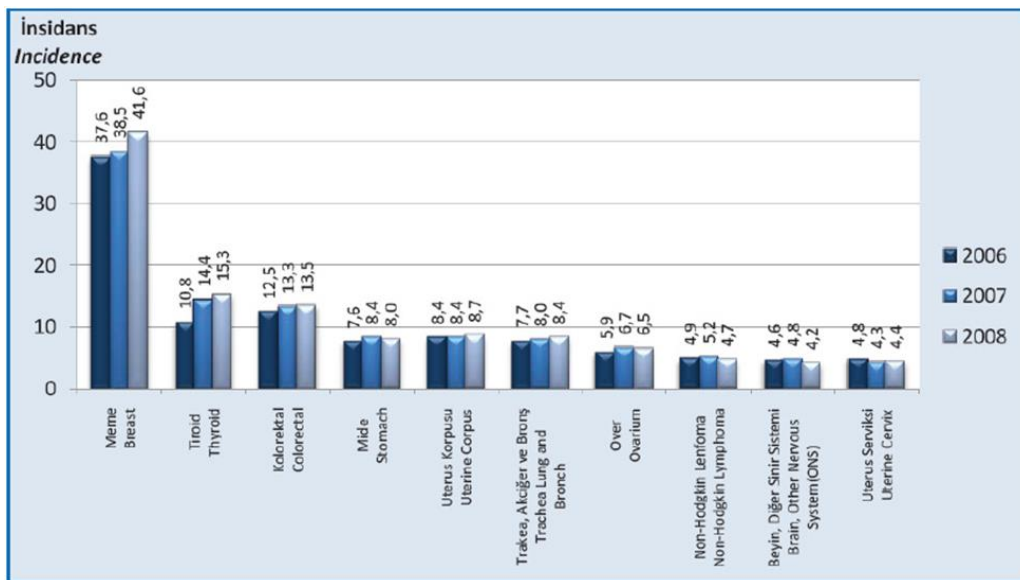


Figure 1.5 : Incidence of the most common 10 types of cancer in women, Turkey, 2006-2008 (Can, 2011).

Before applications of DBT, mammography, ultrasound and magnetic resonance have been recently applied for breast imaging. As an imaging technique, DBT uses a limited viewing angle for scanning the breast. Projections on the detector which are obtained

by scanning of the breast in a limited view are used to produce a 3D image of the breast. This method has an important advantage over 2D mammography to accomplish the overlapping problem, which causes severe artifacts. One of the disadvantages of this technique is that because of the limited view angle, projection number may not be adequate to reconstruct the image completely in the Fourier space (ACS, 2014; Ertas et al., 2012; Ertas et al., 2013a; Helvie, 2010; Wu et al., 2004).

1.4.1 Mammography

Mammography is a specific type of imaging for screening and diagnosis of human breast by using low-energy X-rays (the process usually around 30 kVp). A mammography inspection, which is called mammogram, goals the early detection of breast cancer by detecting of characteristic masses and/or microcalcifications (Lewin & Niklason, 2007; Url-6, 2014).

In Figure 1.6, there are two pictures of mammography; the illustration at left and a real picture of implementation at right. X-ray (radiograph) is the most popular application form of medical imaging and it is a noninvasive tool that helps physicians diagnose. X-ray emits a small dose of ionizing radiation to produce pictures of the inside of body. Digital mammography, computer-aided detection and breast tomosynthesis are advances in mammography (Lewin & Niklason, 2007; Url-6, 2014).

In *digital mammography*, solid-state detectors that convert X-rays into electrical signals replaced the X-ray film. The images of the breast are produced by these electrical signals on a computer screen (Url-6, 2014).

Although both digital and conventional mammography use X-ray to produce a breast image, the image is stored directly on film in conventional mammography. On the other hand, in digital mammography, an electronic image of the breast is stored as a computer file (digital information) that can be enhanced or manipulated for further evaluation more easily than the information stored on a film. Furthermore, digital mammography data can be adjusted, stored, and recovered electronically (Lewin & Niklason, 2007; National Cancer Institute [NCI], 2014).

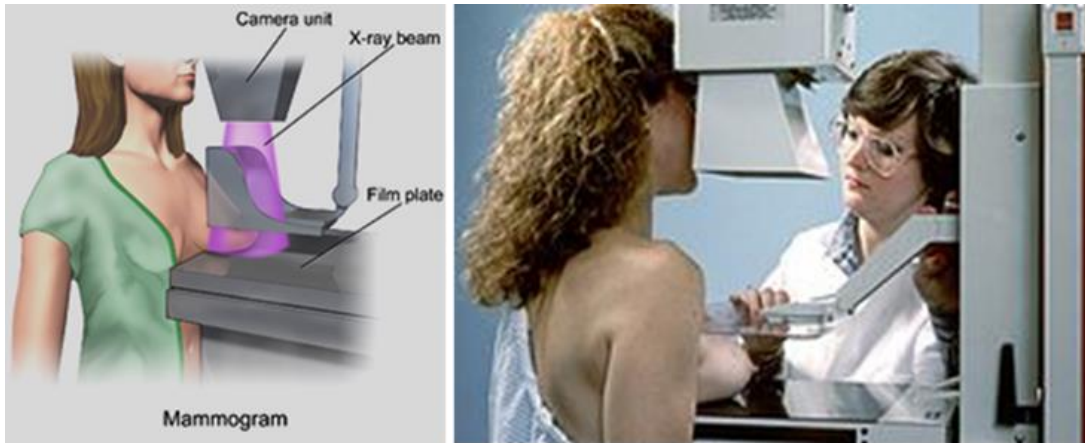


Figure 1.6 : The illustration of mammography (left) (Url-5, 2014); a picture of mammography implementation (right) (Url-6, 2014).

Computer-aided detection (CAD) systems need a digitized mammographic image to search masses or microcalcifications, which are the indicators of the presence of cancer. This digitized mammographic image is accommodated with either a digitally acquired mammogram or a conventional film mammogram (Url-6, 2014).

Breast tomosynthesis is a mammography modality, which uses a moving X-ray tube to expose in an arc over the breast during the imaging. It is also called 3D breast imaging and creates a series of slices (tomographic images) which may be as thin as 0.5 mm through the breast for image processing (Polat et al., 2016; Polat & Yildirim, 2018; Url-6, 2014).

1.4.2 Digital breast tomosynthesis (DBT)

In conventional digital mammography, the structures and tissues of the 3D breast are projected onto a 2D image plane, resulting in the loss of depth vision. Normal breast tissue may hide malignancies, causing a false-negative result or in some cases, the normal tissue may mimic a tumour, resulting in a false-positive result (Tingberg, et al., 2011).

Despite the many advantages of mammography in the past years, it is estimated that at least 20% of breast cancers are still being missed on digital mammograms. The normal tissues of the breast can hide cancers on standard 2D digital mammography that limits the radiologists' ability to detect them (NCI, 2014).

Tomosynthesis or digital breast tomosynthesis (DBT) is a 3D imaging technology that provides high-resolution acquiring images. Compared to conventional mammography,

DBT performs a higher diagnostic accuracy. Stationary compressing of the breast makes image quality better and decreases radiation dose at multiple angles during a short scan. Collected images of DBT have very high resolution (85 - 160 micron typically) which is much higher than CT. A general DBT system is drawn in Figure 1.7.

A compression plate compresses the breast, and the X-ray tube moves through a narrow arc typically between 11° - 60° scanning angle, which means DBT is a limited view angle imaging modality (some references accept 11° - 60° , others accept 15° - 60° or 15° - 50°) with a limited number of discrete exposures (different references assumptions are 7-51, 9-25, and/or 10-25 projections). This limited angle scanning in DBT causes the incomplete data set problem. Advanced reconstruction techniques are used to avoid this problem. (Helvie, 2010; Polat et al., 2016; Polat & Yildirim, 2018; Smith, 2012).

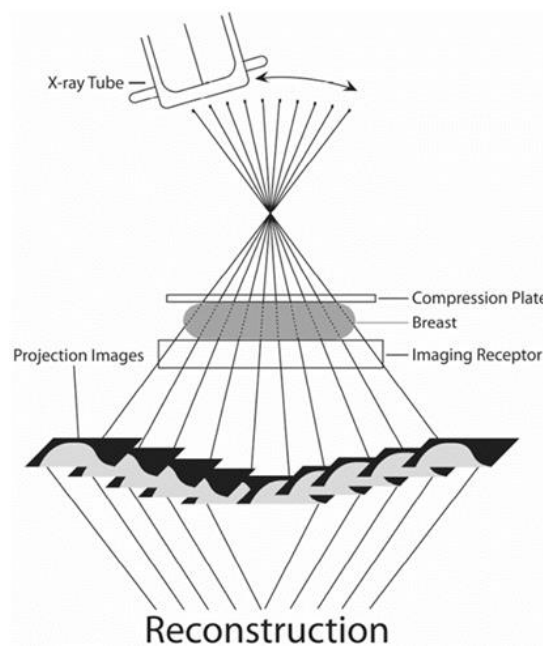


Figure 1.7 : Schematic view of digital breast tomosynthesis (Helvie, 2010).

A few projections are acquired in limited angle scanning, and they are then reconstructed into a series of thin high-resolution slices that can be displayed individually. In single slice 2D mammography imaging tissue overlap and structure noise cause artifacts. These artifacts are eliminated or reduced by reconstructed tomosynthesis slices, and this offers more diagnostic accuracy, fewer recalls, greater radiologist confidence, and 3D lesion localization (Polat et al., 2016; Polat & Yildirim, 2018; Smith, 2012).

In DBT devices (see Figure 1.8), continuous or pulsed exposure, stable or moving detectors, exposure parameters, total dose, effective pixel size, X-ray source, and patient position are taken into account during the design of the device for DBT manufacturers (Helvie, 2010).

The reconstructed images are like pseudo 3D in DBT because of the limited angle of scanning. High-resolution image is arranged on the x-y plane perpendicular to the X-



Figure 1.8 : A tomosynthesis equipment (Sener, 2013).

ray beam. On the other hand, on the parallel plane or z axis, low resolution image is arranged (Helvie, 2010).

Compressed thickness of the breast affects the number of slices to be reviewed. For example, if a 40 cm compressed breast is reconstructed at 1 mm thickness, there will be 40 slices for the physician to review. If the images are reconstructed at 0.5 mm thicknesses, there will be 80 slices to be reviewed. (Helvie, 2010).

In Figure 1.9, overlapping problem is compared for conventional mammography, which provides 2D image (left), and DBT, which provides 2D image (right), and it is clear that in DBT, hidden pathologies (here is as blue lesion) can be detected more easily.

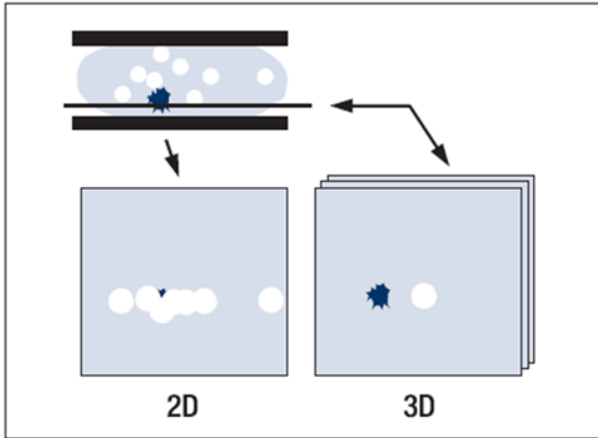


Figure 1.9 : Tissues that overlap in conventional mammography (left) and hide pathologies (blue lesion) are less likely to be obscured using DBT (right) (Smith, 2012).

There are several reconstruction techniques in DBT such as shift-and-add (SAA), tuned aperture computed tomography, filtered back projection (FBP), maximum likelihood reconstruction, and algebraic reconstruction technique (ART), which is one of iterative reconstruction techniques (Helvie, 2010). Principle of SAA tomosynthesis is demonstrated in Figure 1.10.

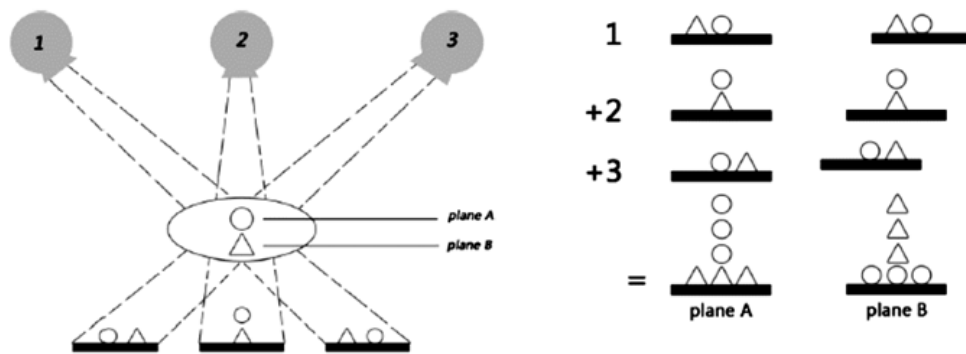


Figure 1.10 : Principle of shift-and-add (SAA) tomosynthesis (Can, 2011).

1.4.3 Radiation dose

A major factor that determines image quality is dose level, therefore manufacturing companies effort to find a balance between dose and image quality. According to current Food and Drug Administration (FDA) exposure limit, all manufacturers design the DBT equipment with dosing parameters less than 300 millirads per exposure. The dose limit per scan is 150-250 millirads in conventional mammography (Helvie, 2010).

The absorbed radiation dose of the breast is a concern because the female breast is so sensitive organ against radiation (Stein et.al., 2014; Svahna et al., 2015). Studies dealing with low-dose imaging with high resolution and low noise have attracted increasing attention in DBT. There are many techniques for reducing imaging dose such as optimization, filtering, and image post-processing (Modulation Transfer Function (MTF), Detective Quantum Efficiency (DQE) or Contrast to Noise Ratio (CNR) and Contrast Detail Studies (CDS)). To evaluate the effect of dose level, the examinations in DBT are generally compared to full-field digital mammography (FFDM) (Svahna et al., 2015; Veldkamp, et. al., 2009; Zhao & Zhao, 2008).

International Commission on Radiological Protection (ICRP) released Diagnostic Reference levels (DRLs), a guideline of patient doses, in radiology. For instance, in

the Mammography Quality Standard Act (MQSA) outlined by FDA restricts a breast dose of 3 mGy per acquisition of the American College of Radiology (ACR) phantom (Svahna et al., 2015).

The cumulative sum of the doses for the sequence of low-dose projections is the total radiation dose in an individual examination of DBT. This dose level is similar to the level used for conventional 2D mammography with 2 mGy per acquisition (Gur et al., 2012; Zhao & Zhao, 2008).

There is a trade-off between increasing and decreasing of the radiation dose. The dose reduction is desired to avoid absorption of the radiation of the patient; however, high imaging dose decreases the electronic noise effects and increases the quality in the individual projections of DBT.



2. AIM AND OBJECTIVE

Digital breast tomosynthesis (DBT) is an innovative imaging modality that provides 3-dimensional (3D) reconstructed images of the breast slice by slice. Missing data in the projections acquired via DBT that arises due to the limited view angle imaging geometry of the modality causes severe artifacts in the reconstructed images. Therefore, advance image reconstruction algorithms need to be developed.

The main objective of this Ph.D. thesis was to develop advanced reconstruction algorithms considering the limitations of the currently available methods in DBT imaging modality and micro-bioimaging (MBI). We compared our methods with the existing methods using both simulated data and real data.

In this study, we mainly had two major purposes. The first purpose was to investigate if compressed sensing based iterative reconstruction technique could decrease the radiation dose applied to the patient. In the scope of the first purpose, we first proposed an effective application of majorization-minimization (MM) based on 3D total variation (TV_{3D}) algebraic reconstruction technique (ART), ART+ TV_{3D} +MM, which is a novel application for DBT, in iterative image reconstruction. In the scope of the first purpose, we secondly proposed to compare ART and compressed sensing based 3D image reconstruction methods (ART+ TV_{3D} and ART+ TV_{3D} +MM) for a real breast phantom at 12 different dose levels. To analyze the performance of the proposed method (ART+ TV_{3D} +MM), we compared the reconstructed images of iterative reconstruction techniques (IRT) (ART, ART+ TV_{3D} , ART+ TV_{3D} +MM) and Siemens MAMMOMAT's FBP at 12 dose levels both qualitatively and quantitatively. The second purpose was to develop algorithms for 3D image reconstruction and to create a robotic scanning tool for imaging system in MBI. In the scope of the second purpose, we created and suggested **the robotic 3D MBI tool** to reconstruct 3D images of various biological samples slice by slice, which means the layers of a biological sample such as a cancerous tumor could be distinguished.



3. LITERATURE REVIEW

The articles and studies about digital breast tomosynthesis (DBT) were investigated in the literature. The basic and the famous article of this subject is Siddon's paper published in 1985. Siddon basically addressed that "a fast calculation of the exact radiological path for a 3D Computed Tomography (CT) array" (Siddon, 1985). Siddon's algorithm should perfectly be comprehended to understand the main logic of image reconstruction.

First, WHO IARC, NBCF, and SEER-based Sree et al. (2011) presented some statistics on cancer and breast cancer (Sree et al., 2011).

Ekstrom (1984) summarized historical improvements and studies of image reconstruction from projections at the end of the Chapter 4 of *Digital Image Processing Techniques*, Academic Press, Orlando-Florida, in 1984 (Ekstrom, 1984) as below;

The first mathematical approach to solve the reconstruction problem was given by Radon in 1917. Bracewell, Oldendorf, Cormack, Kuhl and Edwards, DeRoiser and Klug, Tretiak et al., Rowley, Berry and Gibbs, Ramachandran and Lakshminarayanan, Bender et al., and Bates and Peters examined this problem theoretically and experimentally in chronological order. According to the article of Kak namely "Computerized medical imaging" in 1981, CT (Computed Tomography) imaging studies started before 1979 (Ekstrom, 1984).

Firstly, Bracewell and Riddle and then, independently, Ramachandran and Lakshminarayanan introduced the filtered back projection (FBP) principles. Shepp and Logan first demonstrated that the advantage of FBP algorithm over the algebraic techniques in 1974. Bracewell first derived that a method to reconstruct images by a direct 2D Fourier transformation for radio astronomy in 1956, and later independently DeRoiser and Klug applied this method in electron microscopy in 1968. Dines and Kak, Dreike and Boyd, and Peters and Lewitt developed fast algorithms for ray sorting of fan beam data in 1976, in 1977, and in 1977, respectively. Brooks et al., and

Crawford and Kak studied aliasing artifacts in image reconstruction in 1978, and in 1979, respectively (Ekstrom, 1984).

Polish mathematician Stefan Kaczmarz discovered an iterative algorithm which was named as Kaczmarz method or Kaczmarz's algorithm for solving linear systems of $Ax=b$ equations in 1937 (Kaczmarz, 1937). Gordon et al., Herman et al., Bender et al., and Budinger and Gullberg examined in detail the algebraic techniques to reconstruct images at the first half of the 1970s and rediscovered in the field of image reconstruction from projections, where it was called the algebraic reconstruction technique (ART). Gilbert proposed a new approach for ART which was called simultaneous algebraic reconstruction technique (SART) to improve the convergence features of the algebraic methods in 1972 (Ekstrom, 1984).

Dobbins J. T. III and Godfrey D.J. also summarized the historical background of tomographic imaging in diagnostic radiology at the article *digital X-ray tomosynthesis: current state of the art and clinical potential*, Physics in Medicine and Biology, 48 (2003) R65-R106 (Dobbins J. T. III & Godfrey D.J., 2003) as below;

After Wilhelm Röntgen discovered X-rays in 1895, Radon (1917) provided the mathematical foundation for tomography. In 1932, Ziedses des Plantes introduced tomographic imaging to the medical research community that allowed for the reconstruction of planes from a discrete series of projection images. Garrison et al. who built a prototype '3D roentgenography' device at Johns Hopkins University implemented Ziedses des Plantes' theory for the first time in 1962. Garrison generated a full 3D dataset from a single radiographic scan. Miller et al. (1971) revealed 'photographic laminography' that described the discrete tomography results. Grant published a circular image acquisition geometry based prototype 3D image projector, in 1972. Grant also coined 'tomosynthesis' term referring to create an infinite number of tomograms.

A number of variants of tomosynthesis imaging were developed in the 1970s & 1980s, including *ec-tomography* by Dale and et al., 1985 and flashing tomosynthesis that provided rapid imaging for vascular applications. In the middle of 1980s, several researchers explored methods to decline the blur artifacts associated with tomosynthesis imaging.

Dr. Stein and et al. devised a patent and published evidences about how to reduce dose of tomosynthesis at 2014 that he said one goal of any X-ray imaging system was to gain the highest quality image while minimizing the patient dose. When selecting a radiation dose to use for imaging, a balance must be attained between the image quality and patient safety. As a result, an effort was made to limit the dose of radiation administered during tomosynthesis imaging. In addition the dosage may be controlled by limiting the angle of the scan and or the number of projection images obtained during a scan (Stein et.al., 2014).

Dr. Garrett et al. in their paper published in 2012 concluded using the prior image constrained compressed sensing (PICCS) algorithm to reduce image noise and radiation dose in DBT in the case of the clinical data was possible. Therefore, the PICCS algorithm decreased noise over 35 percent with no loss of diagnostic essential features (such as calcifications / low contrast lesions). According to it, visibility of low contrast lesions was improved with PICCS. Dose reduction of 28 percent was being possible with the phantom data, and the low dose PICCS reconstructions of phantom data showed improved low contrast lesion detectability and lower noise. This indicated potential dose savings in DBT. The diagnostic quality of the phantom reconstructions at 28 percent reduced dose was equivalent to or better than those acquired at full dose (Garrett, et al., 2012).

According to the study done in 2012 by Dr. Wu et al., the patch-based denoising algorithm could decrease the total imaging dose further in DBT by allowing a reduced exposure for each projection view. It was favorable to achieve a proper level of image quality while keeping the radiation dose as low as reasonably achievable. Hence, the patch-based algorithm estimated the true value of a pixel as a weighted average of all pixels in the projection image, where the weights depended on the similarity between the patches that compared with the filtering methods, it could reduce noise while preserving details. The results of Dr. Wu et al. showed image quality of DBT could be potentially improved by the proposed technique by incorporating appropriate denoising into the iterative reconstruction algorithm (Wu et al., 2012).

Dr. Veldkamp et al. in their article published in European Journal of Radiology (EJR) in 2009 described a number of methods about the relationship between the dose and image quality were developed in the last few years. Objective measurements of physical characteristics, such as Modulation Transfer Function (MTF), Detective

Quantum Efficiency (DQE) or Contrast to Noise Ratio (CNR) and Contrast Detail Studies (CDS) were often used.

The CDS could be used to determine dose levels that were related to a desired Contrast Detail Performance (CDP) or could be used to compare different systems or acquisition techniques. An advantage of CDS over objective physical measurements was that CDP includes the performance of human observers. A limitation with both CDP and physical measurements was that the anatomic background was not taken into account.

A number of researchers reported on methods for simulating reduced dose images. A well-established method for reduced dose simulation that was previously described uses DQE at the original and simulated dose levels to create an image containing filtered noise. The method provided for simulated images containing noise in terms of frequency content, agreed very well with original images at the same dose levels (Veldkamp, et. al., 2009).

4. THEORETICAL AND MATHEMATICAL BACKGROUND

4.1 The Mathematical Basis of Projections

Theoretical and mathematical background of medical imaging has two main sections: projections and reconstruction of these projections. The basics of projection and image reconstruction are line integral and inverse problem, respectively.

The fundamentals of computed tomography (CT) are line integral, the Radon transform, and Fourier-Slice theorem (Ntalampeki, 2007). Furthermore, Siddon algorithm is described as a fast and perfect algorithm that calculates the exact radiological path for a 3D CT array in the literature.

The reason of image reconstruction problem that is called inverse problem is described as to reconstruct the region of interest, i.e. to know the function x (unknown density), from its projections taken along the different directions. Here, the distribution of the attenuation coefficient is not directly available; the desired condition is to estimate the object of interest via knowing the projections acquired by a medical imaging equipment. In Figure 4.1, 1-dimensional (1D) projection of a function \mathcal{X} is taken at angle θ means calculating y_θ , which is the integral of distribution of function \mathcal{X} (Duarte, 2009).

4.1.1 Line integral

In tomography, a cross-section in 2D or a volume in 3D is reconstructed from the acquired projections obtained by X-ray attenuation because of intersection of the object's cells. The object function $\mu(x, y)$ which is desired to be reconstructed is modeled as a 2D (or 3D) distribution of the X-ray attenuation function. When a beam of X-ray travels in a straight line through the object the total attenuation of X-rays is represented by a line integral (a projection) (Ntalampeki, 2007; Turbell, 2001). r is calculated at angle θ using the coordinate system in Figure 4.2 by (4.1).

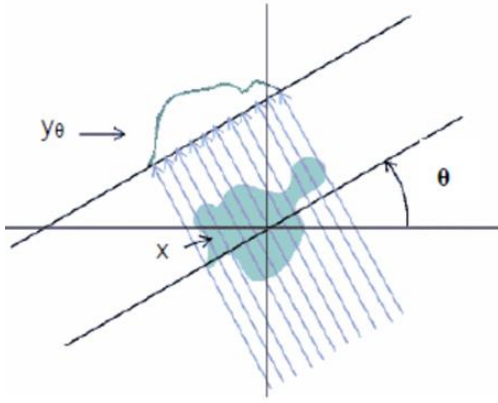


Figure 4.1 : The 1D projection at angle θ .

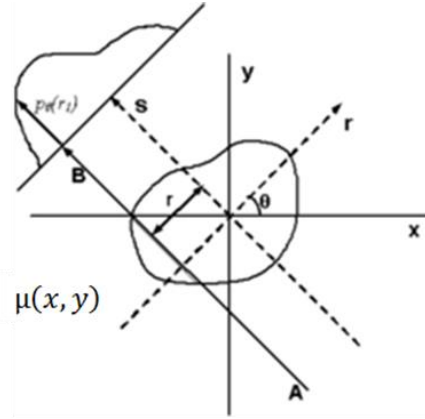


Figure 4.2 : Parallel beam geometry. Each projection is made up of the set of line integrals through the object (Url-7, 2014).

$$x \cos \theta + y \sin \theta = r \quad (4.1)$$

where θ is the angle and r is the smallest distance to the origin of the coordinate system.

The data to be collected is simply considered as a series of parallel rays at position r across a projection at the angle because of the parallel projection system. The line integral (projection, $P_\theta(r)$) of X-ray transmission along a path (L) is given as in (4.2).

$$P_\theta(r) = \int_L \mu(x, y) dl \quad (4.2)$$

$\mu(x, y)$ represents the density (an unknown density) of the 2D object to be reconstructed in (4.2).

This line integral expression can also be explained with the Beer's law (Eq. (4.3)) based on the intensities I_{in} and I_{out} .

$$I_{out} = I_{in} \exp\left(-\int_L \mu(x, y) dl\right) \quad (4.3)$$

I_{in} represents applied intensity from X-ray tube

I_{out} represents attenuated X-ray intensity by the object along the line L .

By taking the logarithm of (4.3), we get the line integral value $P_{\theta}(r)$ of the object function $\mu(x, y)$ as in (4.4).

$$P_{\theta}(r) = -\ln\left(\frac{I_{out}}{I_{in}}\right) = \int_L \mu(x, y) dl \quad (4.4)$$

(Ntalampeki, 2007; Turbell, 2001).

4.1.2 Radon transform

Radon transform has many applications such as medical imaging, radar imaging, and geophysical imaging. In medical imaging, Radon transform is a function, which computes several projections (line integrals) of an image matrix along parallel or cone beams in specified directions. As it can be seen in Figure 4.3, Radon transform takes multiple projections from different angles around the original image, and then the inverse Radon transform is applied to estimate this original image from its projections taken from different angles (Duarte, 2009).

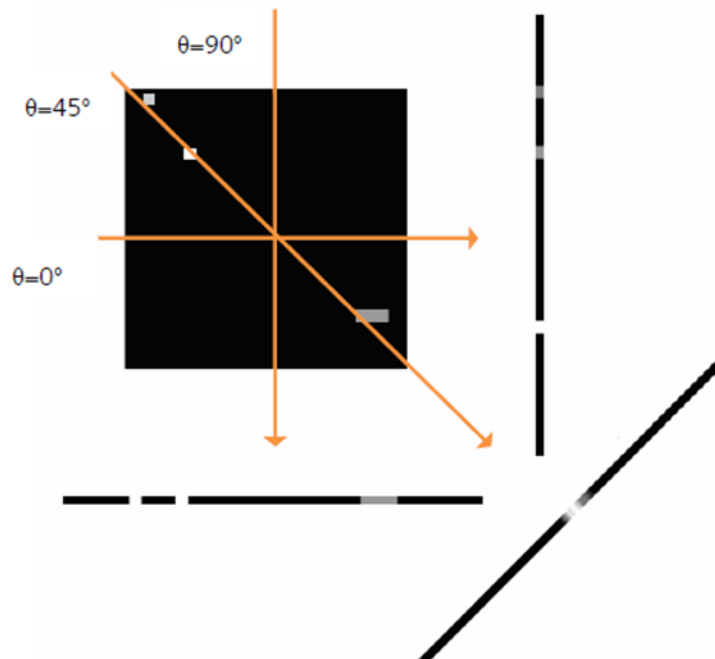


Figure 4.3 : Projections of the object taken from different angles (Duarte, 2009).

Radon transform, the mathematical basis for tomographic imaging, was disclosed by Johann Radon in 1917. It was applied in CT to obtain cross-sectional images of patients. J. Radon proved mathematically that 2D and 3D objects could be reconstructed from their multiple projections (Ntalampeki, 2007; Turbell, 2001). In other words, Radon suggested that a 3D object can be obtained perfectly by using its infinite number sets of 2D projections. Using dirac (δ) function in (4.1), the function $P_\theta(r)$ is described as Radon transform given by (4.5).

$$P_\theta(r) = \int_{-\infty}^{\infty} \int_{-\infty}^{\infty} \mu(x, y) \delta(x \cos \theta + y \sin \theta - r) dx dy \quad (4.5)$$

Since Radon transform of dirac (δ) function is the characteristic function of a sine wave, the term sinogram is used for Radon transform data in the terminology of tomography. The inverse of Radon transform is used for reconstruction of images that means getting $\mu(x, y)$ from (4.5) (Ntalampeki, 2007; Turbell, 2001).

In practice, filtered back projection (FBP) algorithm which is the discretized version of the inverse Radon transform is used for reconstructing because the inverse Radon transform behaves unstable with respect to noisy data (Ntalampeki, 2007; Turbell, 2001).

One of the limitation in the reconstruction of the medical imaging (CT, DBT) is that the projections are acquired in a restricted range of angles such as from -25° to $+25^\circ$ in DBT. Radon transform estimates the attenuation coefficient distribution along the object for each angle projection (Duarte, 2009).

This attenuation coefficient distribution is used to obtain desired object $\hat{\mu}(x, y)$ by evaluating the inverse Radon transform. The substitution of the attenuation coefficient distribution concept is the system matrix in the reconstruction methods such as algebraic reconstruction technique (ART). ART uses a system matrix to obtain a desired image. As it is studied in Section 4.2.1, \mathbf{A} is a system matrix, \mathbf{Y} is the vector of the observed projections, \mathbf{X} is the vector of the desired image in $\mathbf{Y} = \mathbf{AX}$ form of ART. The system matrix \mathbf{A} needed by ART is calculated by Siddon's algorithm.

4.1.3 Siddon algorithm

Siddon's algorithm provides an efficient way to calculate the intersection lengths by following the path of each ray through the volume, using a parametric representation and considering the intersection points with the grid edges in 3D space.

In (Siddon, 1985), Robert L. Siddon described an exact and efficient algorithm for calculating the ray sum that follows a path through a 3D CT. The ray sum, in other words, the radiological path in 3D space is defined by (4.6).

$$d = \sum_i \sum_j \sum_k l(i, j, k) \rho(i, j, k) \quad (4.6)$$

$l(i, j, k)$ defines a part of a certain ray-line intersected by a voxel located in the point (i, j, k) and $\rho(i, j, k)$ is the voxel density (attenuation coefficient). In this algorithm, the crux is that the intersection volumes of equidistant parallel planes build the voxels. The intersection points of the ray with the planes are calculated recursively after determining the intersection point of the ray with the first plane.

Figure 4.4 shows intersection points of the ray with the horizontal lines (filled circles) and the vertical lines (closed circles). A subset of intersections with the lines means the intersections with the pixels of 2D image.

When considering that the pixels are the intersection areas of equally spaced parallel planes, the 2D version of the method is illustrated in Figure 4.4. Figure 4.5 describes the basic parameters of Siddon algorithm, which are the geometric representation of a ray on the 2D image grid.

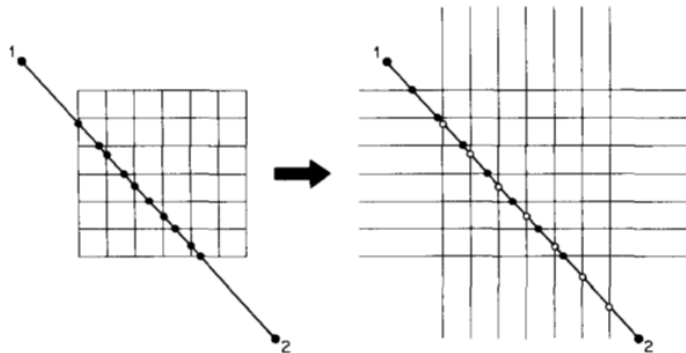


Figure 4.4 : The pixels of CT array (left), the intersection areas of orthogonal sets of equally spaced parallel lines (right) (Siddon, 1985).

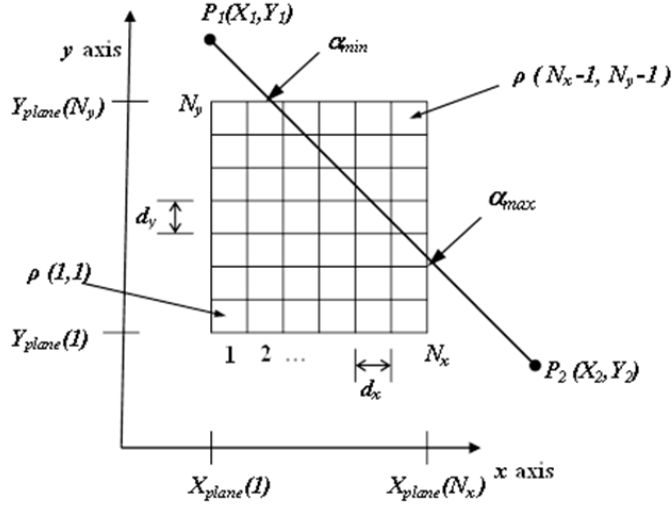


Figure 4.5 : Geometric representation of a ray on the 2D image grid (Can, 2011; Siddon, 1985).

In Siddon's algorithm, a ray from point 1 (P_1) located on (x_1, y_1, z_1) to point 2 (P_2) located on (x_2, y_2, z_2) is defined with the parameter α ($\alpha_1 = 0$ at P_1 and $\alpha_2 = 1$ at P_2) in 3D space. These parametric planes are defined in (4.7).

$$\begin{aligned}
 X(\alpha) &= X_1 + \alpha(X_2 - X_1) \\
 Y(\alpha) &= Y_1 + \alpha(Y_2 - Y_1) \\
 Z(\alpha) &= Z_1 + \alpha(Z_2 - Z_1)
 \end{aligned} \tag{4.7}$$

Each intersection of the ray with each plane has a parameter α in the range of $(\alpha_{\min}, \alpha_{\max})$. If point 1 is inside in the grid, then α_{\min} becomes zero, otherwise α_{\min} is a nonzero value. If point 2 is inside in the grid, then α_{\max} becomes one, otherwise α_{\max} takes a value different than one (see Figure 4.5).

For the number of $(N_x - 1, N_y - 1, N_z - 1)$ voxels of an image array, the orthogonal sets of equidistant parallel planes are written as in (4.8);

$$\begin{aligned}
 X_{plane}(i) &= X_{plane}(1) + (i - 1)dx & i &= 1, 2, \dots, N_x \\
 Y_{plane}(j) &= Y_{plane}(1) + (j - 1)dy & j &= 1, 2, \dots, N_y \\
 Z_{plane}(k) &= Z_{plane}(1) + (k - 1)dz & k &= 1, 2, \dots, N_z
 \end{aligned} \tag{4.8}$$

where dx , dy , and dz are the distances between the x, y, z planes which are the dimensions of the voxel.

The values of α_{\min} and α_{\max} parameters are acquired via intersecting the ray with the in and out sides of the voxel array. The parametric values of the sides are calculated by (4.9) using (4.7) and (4.8).

if $X_2 \neq X_1$,

$$\alpha_x(1) = [X_{plane}(1) - X_1] / (X_2 - X_1) \quad (4.9)$$

$$\alpha_x(N_x) = [X_{plane}(N_x) - X_1] / (X_2 - X_1)$$

Expressions are similar for y and z directions for $\alpha_y(1), \alpha_y(N_y), \alpha_z(1)$, and $\alpha_z(N_z)$. Then α_{\min} and α_{\max} 's quantities are computed by the parametric values of the in and out as in (4.10);

$$\begin{aligned} \alpha_{\min} &= \max \{0, \min[\alpha_x(1), \alpha_x(N_x)], \min[\alpha_y(1), \alpha_y(N_y)], \min[\alpha_z(1), \alpha_z(N_z)]\} \\ \alpha_{\max} &= \min \{1, \max[\alpha_x(1), \alpha_x(N_x)], \max[\alpha_y(1), \alpha_y(N_y)], \max[\alpha_z(1), \alpha_z(N_z)]\} \end{aligned} \quad (4.10)$$

If α_{\max} is less than or equal to α_{\min} then it means that the ray does not intersect the voxel array.

Only certain intersected planes have α parametric value in the range of $[\alpha_{\min}, \alpha_{\max}]$.

These values are used to calculate the range of indices $(i_{\min}, i_{\max}), (j_{\min}, j_{\max})$ and (k_{\min}, k_{\max}) , which intersect the planes (Eq. (4.11)).

if $(X_2 - X_1) \geq 0$,

$$\begin{aligned} i_{\min} &= N_x - [X_{plane}(N_x) - \alpha_{\min}(X_2 - X_1) - X_1] / dx \\ i_{\max} &= 1 + [X_1 + \alpha_{\max}(X_2 - X_1) - X_{plane}(1)] / dx \end{aligned} \quad (4.11)$$

if $(X_2 - X_1) \leq 0$,

$$i_{\min} = N_x - \left[X_{plane}(N_x) - \alpha_{\max}(X_2 - X_1) - X_1 \right] / dx$$

$$i_{\max} = 1 + \left[X_1 + \alpha_{\min}(X_2 - X_1) - X_{plane}(1) \right] / dx$$

with similar notations hold for j_{\min} , j_{\max} , k_{\min} , and k_{\max} . The next step in the algorithm is to create the sets of parametric values ($\{\alpha_x\}$, $\{\alpha_y\}$, $\{\alpha_z\}$) which represent the intersections of the ray with the x, y, z planes can be written for intersected indices using the notation for $\{\alpha_x\}$, and with similar notations for $\{\alpha_y\}$, and $\{\alpha_z\}$;

if $(X_2 - X_1) > 0$,

$$\{\alpha_x\} = \{\alpha_x(i_{\min}), \dots, \alpha_x(i_{\max})\}$$

if $(X_2 - X_1) < 0$,

$$\{\alpha_x\} = \{\alpha_x(i_{\max}), \dots, \alpha_x(i_{\min})\}$$

(4.12)

where

$$\alpha_x(i) = \left[X_{plane}(i) - X_1 \right] / (X_2 - X_1) \quad (4.13)$$

It is seen that $\{\alpha_x\}$, $\{\alpha_y\}$, and $\{\alpha_z\}$ sets are in ascending or in descending order according to the sign of differences of the point 1 and point 2 for each dimensions.

The definite intersection points are found by merging the sets $\{\alpha_x\}$, $\{\alpha_y\}$, and $\{\alpha_z\}$ into one set considering the ending points of the ray can be inside the array, therefore the maximum and minimum values (α_{\min} and α_{\max}) are also added to the merged set.

The merged set which is the new $\{\alpha\}$ set has the form expressed as in (4.14).

$$\{\alpha\} = \{\alpha_{\min}, \text{merge}[\{\alpha_x\}, \{\alpha_y\}, \{\alpha_z\}], \alpha_{\max}\}$$

$$\{\alpha\} = \{\alpha(0), \alpha(1), \dots, \alpha(n)\}$$

(4.14)

The parameter set consists of $(n+1)$ element where n is given as in (4.15);

$$n = (i_{\max} - i_{\min} + 1) + (j_{\max} - j_{\min} + 1) + (k_{\max} - k_{\min} + 1) + 1 \quad (4.15)$$

The intersection length, which means the weighting factor of intersected voxels, can be defined in terms of the difference between the two adjacent terms in the set of α parameters. Once the $\{\alpha\}$ array has been formed it is possible to calculate the voxel that was hit and its intersection length with the ray as well. Then the intersection length formed by the $(m)^{th}$ and $(m-1)^{th}$ intersections of the $\{\alpha\}$ array, which are the weights of the intersected voxels, are calculated with (4.16).

$$l(m) = d_{12} [\alpha(m) - \alpha(m-1)] \quad \text{for } m = 1, 2, 3, \dots, n \quad (4.16)$$

where α is taken from the $\{\alpha\}$ array and d_{12} is the total length (the Euclidian distance) of the ray from point 1 to point 2 and is given by (4.17).

$$d_{12} = \sqrt{(X_2 - X_1)^2 + (Y_2 - Y_1)^2 + (Z_2 - Z_1)^2} \quad (4.17)$$

The voxel's indexes $[i(m), j(m), k(m)]$ which intersect the ray are related with the midpoint of the $(m)^{th}$ and $(m-1)^{th}$ that are two adjacent intersections and they are calculated as in (4.18).

$$\begin{aligned} i(m) &= 1 + \left[X_1 + \alpha_{mid} (X_2 - X_1) - X_{plane}(1) \right] / dx \\ j(m) &= 1 + \left[Y_1 + \alpha_{mid} (Y_2 - Y_1) - Y_{plane}(1) \right] / dy \\ k(m) &= 1 + \left[Z_1 + \alpha_{mid} (Z_2 - Z_1) - Z_{plane}(1) \right] / dz \end{aligned} \quad (4.18)$$

where the α_{mid} is the midpoint of the $(m-1)^{th}$ and the m^{th} intersections and is given by (4.19).

$$\alpha_{mid} = [\alpha(m) + \alpha(m-1)] / 2 \quad (4.19)$$

Finally the projection value P_θ (the radiological path) can be obtained by performing the sum over the n elements of the $\{\alpha\}$ array. This is achieved with (4.20).

$$P_{\theta} = \sum_{m=1}^n l(m) \rho[i(m), j(m), k(m)] \quad (4.20)$$

$$P_{\theta} = d_{12} \sum_{m=1}^n [\alpha(m) - \alpha(m-1)] \rho[i(m), j(m), k(m)]$$

where $\rho(i, j, k)$ defines the voxel intensity and n is given in (4.15).

Siddon's algorithm primarily provides evaluating the exact radiological path of a ray through a 3D CT array. One advantage of this algorithm is its computation time that is scaled with the proportional number of the planes (N) instead of the proportional number of voxels (N^3). Parametric values, which hit the voxels, define intersections of the ray with the planes. These intersections are weighting factor of total intersected length of the ray hits the 3D array for each voxel (Siddon, 1985).

4.2 Reconstruction Methods

There are several reconstruction methods to reconstruct the image from projections obtained from the objects (Figure 4.6). Two main techniques of the reconstruction methods are analytical (Fourier transform, filtered back projection) and algebraic (statistical e.g. ML: maximum-likelihood, EM: expectation-maximization; iterative e.g. algebraic reconstruction technique (ART), simultaneously algebraic reconstruction technique (SART), and simultaneous iterative reconstruction technique (SIRT)). Because of only ART is studied in this thesis, ART is examined in detail in Section 4.2.1.

4.2.1 Algebraic reconstruction technique (ART)

As mentioned in the previous sections, projections obtained from target object that will be re-projected are used to reconstruct the related target object in medical applications such as X-ray CT and DBT. The reconstruction algorithm can be classified into four major groups that are the summation methods, the convolution methods, the Fourier methods, and the summation expansion methods. Iterative reconstruction methods take part in the group of the summation expansion methods (Peterson et al., 1985).

Reconstruction methods can also be classified as analytical (Fourier transform and FBP) and algebraic (statistical and iterative) (see Figure 4.6).

Reconstruction Methods	Analytical	Fourier Transform	
		Filtered Back Projection	
	Algebraic	Statistical	ML-EM
		Iterative	ART, SART, SIRT

Figure 4.6 : Reconstruction methods

There are several different approaches with their references of iterative reconstruction techniques, which are written in Table A.1, in appendices (Beister et al., 2012).

In the first step of iterative reconstruction technique, a dummy raw data is created by forward projection of the estimated object. This data is compared to the real measured raw data to calculate a correction term in the second step. In the third and last step, the correction term is back-projected to estimate the object. Generally, an empty image estimation or a prior knowledge is used to initialize the iteration process. If approaching a constant number of iteration or the variation of the image estimation is small enough to update, the iterative process is ended (Beister et al., 2012).

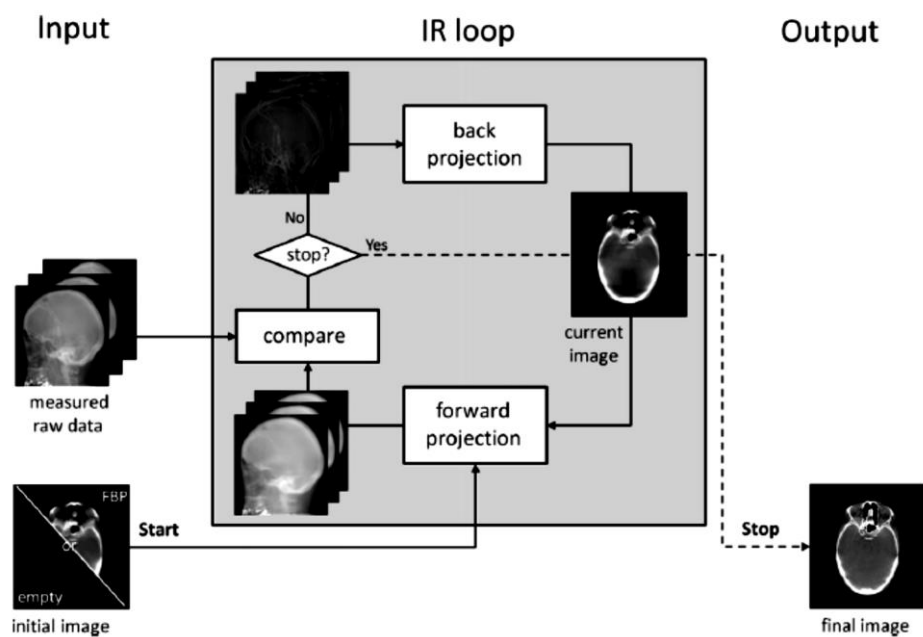


Figure 4.7 : A schematic view of the iterative reconstruction process (Beister et al., 2012).

These iterative reconstruction algorithms benefit from sparsity matrices to solve integral equation in matrix form using a relaxation coefficient. The rays through the object are assumed as non-refracting, straight, and having a full range of penetration angles. One of these techniques, ART, finds a wide use for the application of reconstruction problems, because it is favorable for different geometries and limited projection angles (Peterson et al., 1985).

The principle of ART is to solve \mathbf{X} of the equation system expressed in matrix form as $\mathbf{Y} = \mathbf{AX}$. Solving \mathbf{X} includes large, sparse arrays and linear algebra examines sparse matrices very well (Peterson et al., 1985).

ART, the common and basic form of iterative reconstruction, was used for the reconstruction of images in the first CT systems. Kaczmarz introduced ART principles for solving linear systems of equations $\mathbf{AX} = \mathbf{Y}$ in 1937 (Kaczmarz, 1937). First medical imaging application of ART was performed by Herman in 1980 (Herman, 1980).

Because of limited projections in low dose CT, the use of ART increases for the estimation from the missing views in recent works. Missing projections are initially set to zero to estimate projections for following CT reconstruction based on convolution-back projection in re-projection step. The computation accuracy of this step is very important for determining the quality of the final reconstructed image (Andersen, 1989; Beister et al., 2012).

The reconstruction problem becomes one of solving a linear algebraic equation of the form

$$\mathbf{A} \bullet \vec{\mathbf{X}} = \vec{\mathbf{Y}} \quad (4.21)$$

In the form $\mathbf{A} \bullet \vec{\mathbf{X}} = \vec{\mathbf{Y}}$; $\vec{\mathbf{X}}$ is the column vector of the object whose elements are the voxels (number m) of the 3D object to be reconstructed.

\mathbf{A} is the system matrix which includes the weighting factor of each voxel (number m) for each rays (number n) used for producing the raw data. It is a non-negative elements-2D matrix that describe the probability of a photon that hits a voxel. For each projection of the object, a system matrix $\mathbf{A}_{n \times m}$ is built up.

\vec{Y} is the detector (column vector) whose elements are the pixels of the measured raw data (projections) for every ray per angle.

To reconstruct an image mathematically, (4.21) can be written in an expanded form as linear system equations;

$$\begin{aligned}
 a_{11}x_1 + a_{12}x_2 + a_{13}x_3 + \dots + a_{1m}x_m &= y_1 \\
 a_{21}x_1 + a_{22}x_2 + a_{23}x_3 + \dots + a_{2m}x_m &= y_2 \\
 a_{31}x_1 + a_{32}x_2 + a_{33}x_3 + \dots + a_{3m}x_m &= y_3 \\
 \dots & \\
 a_{n1}x_1 + a_{n2}x_2 + a_{n3}x_3 + \dots + a_{nm}x_m &= y_n
 \end{aligned}
 \tag{4.22}$$

In Eq. (4.22);

m represents the number of voxels of the object

n represents the number of the ray within each projection

a_{ij} represents weight coefficients of A system matrix ($i=1,2,\dots,n; j=1,2,\dots,m$) (Andersen, 1989; Duarte, 2009; Tessa et al., 2004). The intensities of voxels (in 3D case) or pixels (in 2D case) are updated in the each iteration in the ART algorithm (see

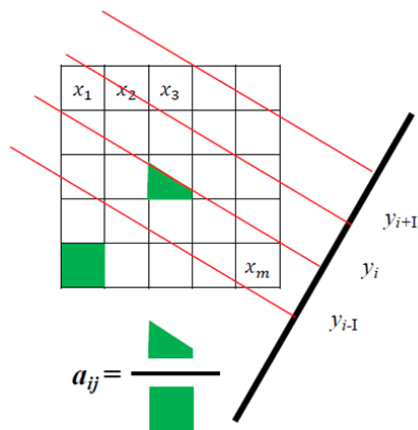


Figure 4.8 : The illustration of calculating of weight factor a_{ij} in ART algorithm (Tessa et al., 2004).

Figure 4.8). This updating process provides that the calculated projection comes close to the measured projection. ART implementation supplies that the change of the grayness of pixels when the ray intersect the pixel (Andersen, 1989; Tessa et al., 2004).

One of other approaches of ART is the estimation of an image provided by minimizing the difference between calculated and measured projections formulated as in (4.23).

$$\hat{X} = \underset{X}{\operatorname{arg\,min}} \left(\|Y - AX\|_2^2 \right) \quad (4.23)$$

\hat{X} represents the estimation of the image,

Y represents the measured data,

X is the image to be reconstructed,

A represents the system matrix or the weighting matrix.

The image X that will be estimated is updated in each iteration by using the mathematical formula stated in (4.24).

$$X_j^{(k+1)} = X_j^{(k)} + \frac{Y_i - \sum_{m=1}^M a_{im} X_m^{(k)}}{\sum_{m=1}^M a_{im}^2} a_{ij}, \quad \text{for } \begin{array}{l} i = 1, 2, 3, \dots, N \\ j = 1, 2, 3, \dots, M \end{array} \quad (4.24)$$

where N is the ray number, and M is the voxel number.

The Eq. (4.24) can be also written as below (Peterson et al., 1985);

$$X_j^{(k+1)} = X_j^{(k)} + \Delta X_{ij}^{(k+1)}, \quad \text{for } \begin{array}{l} i = 1, 2, 3, \dots, N \\ j = 1, 2, 3, \dots, M \end{array} \quad (4.25)$$

The term $\Delta X_{ij}^{(k+1)}$ in (4.25) is the correction term. The determination of this correction term is the basis of ART algorithm. The correction term is then applied to each pixel or voxel through which the ray i passes (Peterson et al., 1985). The explanations of the terms of (4.24) and (4.25) are listed below.

$X_j^{(k)}$ is previous image before $(k + 1)^{th}$ iteration

$X_j^{(k+1)}$ is updated image after $(k + 1)^{th}$ iteration

Y_i is the measured projection data corresponding to the i^{th} ray line integral

$\sum_{m=1}^M a_{im} X_m^{(k)}$ is the calculated projection data

$Y_i - \sum_{m=1}^M a_{im} X_m^{(k)}$ is the error value

$\sum_{m=1}^M a_{im}^2$ is the normalization factor

$\Delta X_{ij}^{(k+1)}$ is the correction term

a_{ij} represents weight coefficients of A-system matrix ($i=1,2,\dots,n; j=1,2,\dots,m$)

m represents the number of voxels of the object (j is voxel (m) indices)

n represents the number of the ray within each projection (i is ray (n) indices)

The contribution of j^{th} voxel on the i^{th} ray line integral is weighted by system coefficients a_{ij} . Since Siddon's algorithm calculates these coefficients, a_{ij} is also called Siddon's coefficients. A single iteration means that the updating is repeated for all projections (Ertas et al., 2013b; Peterson et al., 1985).

4.3 Improvement and Optimization Methods

Compressed sensing (CS) based approaches, especially total variation (TV) minimization, have drawn a great interest in limited view angle imaging problems such as DBT imaging (see Figure 4.9).

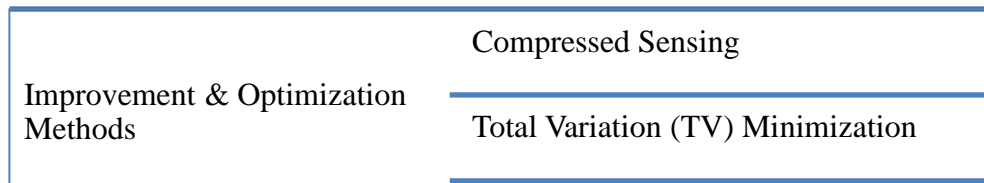


Figure 4.9 : Improvement and optimization methods.

4.3.1 Compressed sensing

The Shannon/Nyquist sampling theorem suggests that sampling frequency of a signal (f_{NYQ}) must be at least two times faster than its bandwidth (W) for loseless uniformly sampling ($f_{NYQ} \geq 2W$). Since images are not bandlimited, the sampling rate is specified by the desired spatial resolution not by the Shannon theorem. In the case of the number of sampling is much less than Nyquist rate ($f_{CS} \ll f_{NYQ}$) compressed sensing (CS) theory comes in view. CS theory affirms that perfectly reconstruction of an object from its far fewer samples or measurements under certain circumstances. To make this possible, CS relies on two principles: *sparsity* and *discrepancy*. The object being recovered must be either sparse or can be sparsified (Candes & Wakin, 2008; Park, et.al, 2015).

In a relatively recent study by Donoho, it was proved that a sparse signal can be recovered exactly from a small set of linear observations. The reason why it is called “compressed sensing” is that sparse signals can be sensed by taking far fewer measurements (Donoho, 2006). There are three important aspects on difference between CS and classical sampling theory. First, CS measures finite-dimensional vectors in \mathcal{R}^n in terms of mathematical theory; however, sampling theory focuses on infinite length and continuous-time signals. Second, in sampling theory, the signal is sampled at specific points in time, but the measurements acquired by CS systems are in the form of inner products between the signal and test functions (Eldar & Michaeli, 2009). Third, the signal recovery is done using highly nonlinear methods in CS, whereas the signal is reconstructed by interpolation in the sense of Nyquist frequency in sampling theory (Tropp & Wright, 2010).

In this Ph.D. thesis, we use CS theory to enhance the quality of reconstructed image obtained via ART. To be able to apply CS theory, the image must be sparse and reconstructed using a nonlinear method (Chen et. al., 2008; Donoho, 2006).

It was mentioned that ‘Radon says that a 3D object can be recovered perfectly by using its infinite number sets of 2D projections’ in Section 4.1.2. In this work, we intend to reconstruct 3D images from its 25 sets of 2D projections at maximum, which means that we have very underdetermined observations (projections) against to infinite numbers of projections.

The definition of the CS-based reconstruction algorithm is explained mathematically as follows. The original vector, $\mathbf{X}_{m \times 1}$, to be reconstructed and the measured projection vector, $\mathbf{Y}_{n \times 1}$, are represented by (4.26).

$$\mathbf{X}_{m \times 1} = \begin{bmatrix} x_1 \\ x_2 \\ \vdots \\ x_m \end{bmatrix}, \quad \mathbf{Y}_{n \times 1} = \begin{bmatrix} y_1 \\ y_2 \\ \vdots \\ y_n \end{bmatrix} \quad (4.26)$$

m-voxels of \mathbf{X} vector

n-observations of \mathbf{Y} vector

n-observations also means the number of sampling points in the projection data. \mathbf{A} -system matrix that contains the weighting of every voxel for all the rays in the projection data, relating \mathbf{X} and \mathbf{Y} , is defined as a matrix by (4.27).

$$\mathbf{A}_{n \times m} = \begin{bmatrix} a_{11} & a_{12} & \cdots & a_{1m} \\ a_{21} & a_{22} & \cdots & a_{2m} \\ \vdots & \vdots & \ddots & \vdots \\ a_{n1} & a_{n2} & \cdots & a_{nm} \end{bmatrix}, \quad (n\text{-rays}) \times (m\text{-voxels}) \quad (4.27)$$

Using these definitions, the measurement equation (inverse problem) is described by;

$$\mathbf{Y}_{n \times 1} = \mathbf{A}_{n \times m} \bullet \mathbf{X}_{m \times 1}; \quad \begin{bmatrix} y_1 \\ y_2 \\ \vdots \\ y_n \end{bmatrix} = \begin{bmatrix} a_{11} & a_{12} & \cdots & a_{1m} \\ a_{21} & a_{22} & \cdots & a_{2m} \\ \vdots & \vdots & \ddots & \vdots \\ a_{n1} & a_{n2} & \cdots & a_{nm} \end{bmatrix} \bullet \begin{bmatrix} x_1 \\ x_2 \\ \vdots \\ x_m \end{bmatrix} \quad (4.28)$$

Then, the problem becomes to recover \mathbf{X} from \mathbf{Y} . $\mathbf{X}_{m \times 1}$, m -voxels of the phantom, are described as unknowns in (4.28). The condition n -projections $<$ m -unknowns means the number of the projections/rays/observations (n) is less than the number of the voxels (m) of the phantom. For $n < m$, $\mathbf{Y} = \mathbf{A}\mathbf{X}$ is an underdetermined linear equation having infinite solutions of \mathbf{X} from the observed \mathbf{Y} . The main notion of the CS-based tomosynthesis image reconstruction is to take advantage of the sparsity of \mathbf{X} or being able to sparsify it.

Since the derivative of natural images is expected to become sparse, the gradient operator \mathbf{D} is often used as an effective sparsifying transform for common medical images. Thus to minimize ($\|\bullet\|_{l_0}$; l_0 norm) of an objective function $f(x)$, which is an optimization problem, recovers the original image vector \mathbf{X} , described in (4.29):

$$\hat{\mathbf{X}} = \arg \min_x \|f(x)\|_{l_0} \quad (4.29)$$

The Eq. (4.29) describes the general definition of compressed sensing (Donoho, 2006; Park, et.al, 2015). For linear transformation, and for a linear transform operator, Φ , compressed sensing shades into (4.30) that yields $\mathbf{Y} = \mathbf{A}\mathbf{X}$.

$$\hat{\mathbf{X}} = \arg \min_x \|\Phi \mathbf{X}\|_{l_0}, \quad \text{such that} \quad \mathbf{Y}^{cal} = \mathbf{A}\mathbf{X} \quad (4.30)$$

$\|\bullet\|_{l_0}$ provides compressed sensing based application, and φ -sparsifying operator, which guarantees the sparse solution of \mathbf{X} , sparsifies the image by transforming non-sparse image \mathbf{X} to the sparsified version. Other commonly used φ -sparsifying operators except the gradient operator \mathbf{D} are Wavelet transform and *Total Variation (TV)* operator. In this study, for φ , \mathbf{TV} was assigned as the sparsifying transform. The most components of $TV(\mathbf{X})$ are negligibly small. By using this property, the number of unknowns in (4.28) can be reduced from m to n so that (4.28) becomes uniquely solvable achieving accurate reconstruction. Therefore, CS-based application of a general cost function $f(x)$ can be expressed as in (4.31).

$$f(x) = \frac{1}{2} \|\mathbf{Y}^{meas} - \mathbf{Y}^{cal}\|_2^2 + \lambda \|TV(\mathbf{X})\|_2 \quad (4.31)$$

In the Eq. (4.31), $\frac{1}{2} \|\mathbf{Y}^{meas} - \mathbf{Y}^{cal}\|_2^2$ is the fidelity term whereas $\|TV(\mathbf{X})\|_2$ is the penalty or regularization term, which is an approximate solution to compressed sensing theory. λ is a regularization parameter that provides a balance between the fidelity term and the regularization term. \mathbf{Y}^{meas} is the measured data vector and \mathbf{Y}^{cal} is the calculated projection vector (Chen et. al, 2008; Donoho, 2006; Park, et.al, 2015; Polat et al., 2016; Polat & Yildirim, 2018).

4.3.2 Total Variation (TV) minimization

Rudin, Osher, and Fatemi (ROF) introduced first total variation as a regularizing criterion for solving inverse problems in 1992. ROF has achieved regularized images without smoothing the boundaries of the objects (Chambolle, 2004; Rudin, et.al, 1992). The regularization term of (4.31) can be expressed as

$$\|TV(\mathbf{X})\|_2 = \sum_{i=1}^N \|D_i \mathbf{X}\|_2 \quad (4.32)$$

where D_i is the forward difference approximation to the gradient at i^{th} voxel (Park, et.al, 2015). The Eq. (4.33) is the expanded form of (4.32) for l_2 -norm of 3D TV .

$$TV_{3D}(\mathbf{X}) = \sum_k^K \sum_j^J \sum_i^I \sqrt{(X_{i,j,k} - X_{i-1,j,k})^2 + (X_{i,j,k} - X_{i,j-1,k})^2 + (X_{i,j,k} - X_{i,j,k-1})^2} \quad (4.33)$$

Finally, in (4.34) that is called *TV* minimization reconstruction problem, l_2 -norm of 3D-*TV* minimization is applied to the compressed sensing formula (Eq. (4.30)) in an unconstrained minimization form to recover \mathbf{X} .

$$\hat{\mathbf{X}} = \underset{\mathbf{X}}{\text{arg min}} [\|\mathbf{Y}^{meas} - \mathbf{Y}^{cal}\|_2^2 + \lambda \|TV(\mathbf{X})\|_2] \quad (4.34)$$

λ regularization parameter that controls the effect of the sparsifying term *TV* on the cost function (Ertas, 2015; Park, et.al, 2015; Polat et al., 2016; Polat & Yildirim, 2018). *TV* term contains the sparsifying information of the image. This sparsifying information is used in the missing data problems caused by the few numbers of projections acquired from limited view angle imaging modality in DBT. The solution of *TV* minimization is performed by using the steepest descent algorithm. The gradient of the l_2 -norm of 3D-*TV*, which means the derivative of 3D-*TV*(\mathbf{X}) is expressed in (4.35).

$$\begin{aligned} \text{Grad}(\mathbf{X}) = \frac{dTV[X(i, j, k)]}{dX(i, j, k)} = & \\ & \frac{3X(i, j, k) - X(i+1, j, k) - X(i, j+1, k) - X(i, j, k+1)}{\sqrt{(X(i, j, k) - X(i+1, j, k))^2 + (X(i, j, k) - X(i, j+1, k))^2 + (X(i, j, k) - X(i, j, k+1))^2 + \varepsilon}} \\ & + \frac{X(i, j, k) - X(i-1, j, k)}{\sqrt{(X(i-1, j, k) - X(i, j, k))^2 + (X(i-1, j, k) - X(i-1, j+1, k))^2 + (X(i-1, j, k) - X(i-1, j, k+1))^2 + \varepsilon}} \quad (4.35) \\ & + \frac{X(i, j, k) - X(i, j-1, k)}{\sqrt{(X(i, j-1, k) - X(i+1, j-1, k))^2 + (X(i, j-1, k) - X(i, j, k))^2 + (X(i, j-1, k) - X(i, j-1, k+1))^2 + \varepsilon}} \\ & + \frac{X(i, j, k) - X(i, j, k-1)}{\sqrt{(X(i, j, k-1) - X(i+1, j, k-1))^2 + (X(i, j, k-1) - X(i, j+1, k-1))^2 + (X(i, j, k-1) - X(i, j, k))^2 + \varepsilon}} \end{aligned}$$

ε was chosen as 10^{-8} for the applications and algorithms, which avoids being zero-value of the denominators of (4.35).

The flowchart of the CS-based 3D image reconstruction (ART+TV_{3D}) in DBT image reconstruction is illustrated in Figure 4.10.

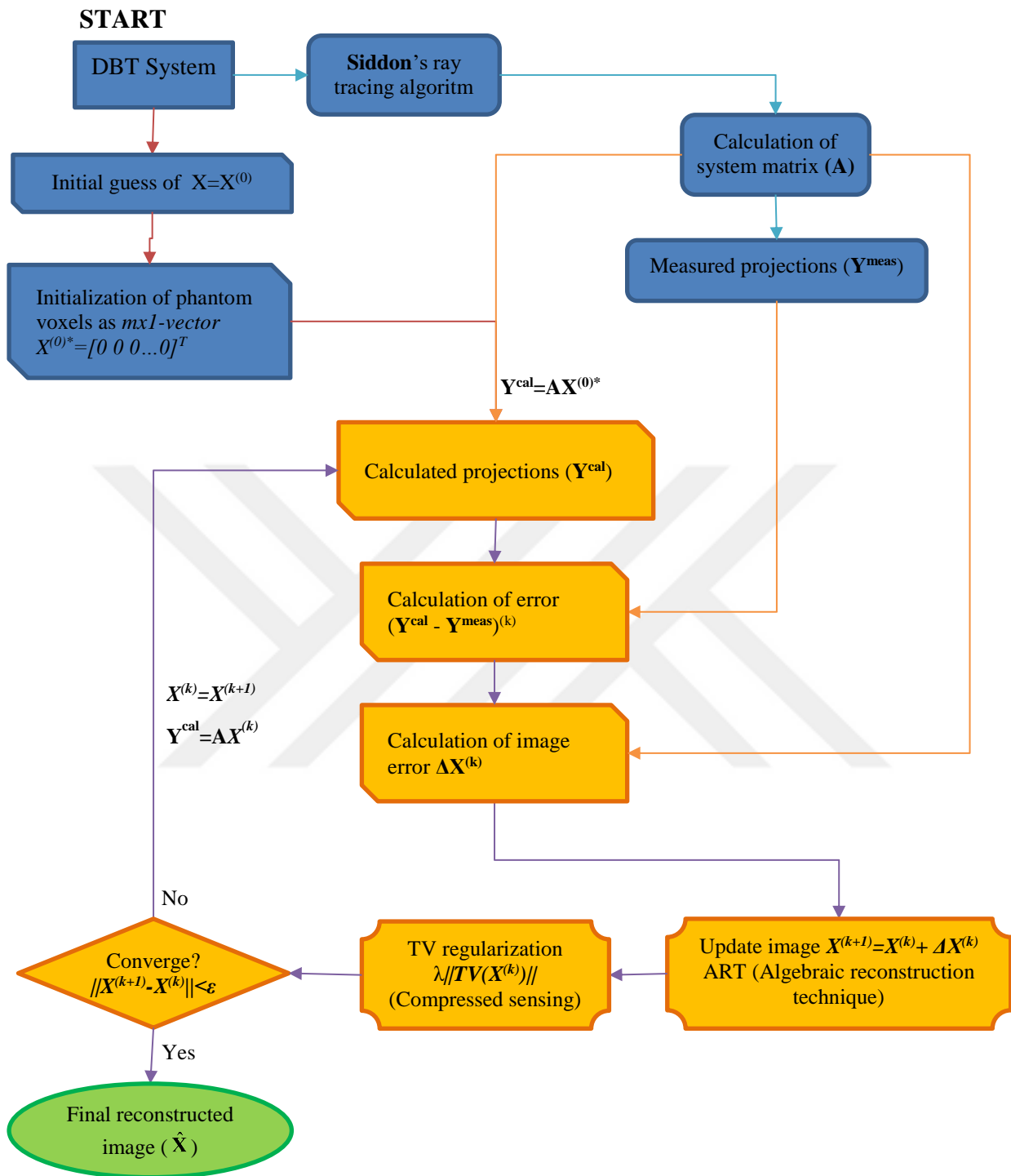


Figure 4.10 : Flowcart of the CS-based algorithm (ART+TV_{3D}) for DBT reconstruction.

4.3.3 Majorization-Minimization algorithm

Until recently, only a few studies mentioned 3D TV minimization, whereas the majority of them were concerned with 2D TV minimization (Ertas et al., 2013a; Polat et al., 2016; Polat & Yildirim, 2018). In addition, as used to TV denoising, a new algorithm majorization-minimization (MM) (Figueiredo et al., 2007) was introduced for a 1D signal and N-point $x(n)$ in the literature of signal processing (Selesnick, 2014). The MM algorithm finds the maxima or minima of a function by exploiting the convexity of the function to optimize a developed iterative algorithm (Figueiredo et al., 2007; Hunter & Lange, 2004; Polat & Yildirim, 2018; Selesnick, 2014).

Additionally, MM algorithm solves a sequence of optimization problems, for minimizing a convex cost function by using the following formulation (Figueiredo et al., 2007; Hunter & Lange, 2004; Polat & Yildirim, 2018; Selesnick, 2014).

$$x^{(k+1)} = \underset{x}{\operatorname{arg\,min}} G_k(x) \quad (4.36)$$

k is the number of iteration, and must be chosen as a majorizer of (4.37).

$$\begin{aligned} G_k(x) &\geq F(x), \forall x \\ G_k(x^{(k)}) &= F(x^{(k)}) \end{aligned} \quad (4.37)$$

As far as we know, in DBT studies, this MM algorithm has not yet been applied. However, in (Polat et al., 2016), our group performed the MM algorithm application to the 3D DBT imaging problem to demonstrate a proof-of-concept recently. This was the first application of the MM algorithm to the 3D DBT and has been performed for a 3D analytical phantom mimicking a breast and for a real breast phantom with 301x236 pixels with only one radiation dose (Polat et al., 2016).

In this study, using an analytical phantom and real data, we propose the implementation of the MM algorithm to the 3D DBT imaging problem. The proposed method ART+TV_{3D}+MM, ART+TV_{3D}, and ART are executed for a phantom that mimics 3D breast as in (Polat et al., 2016; Polat & Yildirim, 2018) by evaluating both qualitative and quantitative analyses. In ART+TV_{3D}+MM method, MM algorithm is applied to TV_{3D} (ART+TV_{3D}) volumes in each iteration (Polat et al., 2016; Polat & Yildirim, 2018).

We proposed to apply MM algorithm in our ART+TV_{3D}+MM method by adapting MM algorithm developed by Selesnick (2014) to our problem with five iterations. MM algorithm has another inner iteration process in itself. All algorithms were performed on MATLAB R2015b.

The convergence criterion for stopping the iteration of MM, $Variation(\%)$ in (4.38), was set for MM based on the difference of the mean value of a chosen region of interest (ROI) (μ_{ROI}) from one iteration (k) to the next (Oliveira et. al., 2016).

$$Variation(\%) = \frac{\mu_{ROI}(k) - \mu_{ROI}(k-1)}{\mu_{ROI}(k-1)} \times 100 \quad (4.38)$$

The iteration number of MM algorithm was chosen based on (4.38) (Oliveira et. al., 2016), whereas the iteration number of ART+TV_{3D} was chosen based on experimental trials. The graph of $Variation(\%)$ of the ROI for MM algorithm is shown in Figure 4.11. We decided the number of the inner iteration of MM what the values of the $Variation(\%)$ were under 5%. In our studies, we reached the $Variation(\%)$ value below 5% at the 3rd iteration; however, we preferred five iterations since the variation at the 4th iteration was higher than the 3rd iteration.

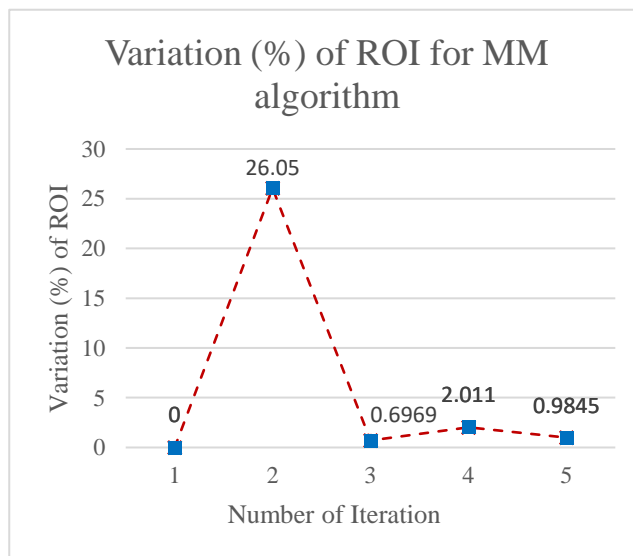


Figure 4.11 : Convergence criterion for inner iteration of MM algorithm.

5. DATA AND METHODOLOGY

5.1 Data and Methodology for Digital Breast Tomosynthesis (DBT)

The studies in DBT part of this Ph. D. thesis were performed at *Istanbul Technical University*, at *Instituto de Biofisica e Engenharia Biomedica, Faculdade de Ciencias, Universidade de Lisboa, Lisbon, Portugal* (from April 8, 2016 to July 8, 2016) and at *Harvard Medical School, Harvard-MIT Health Sciences and Technology, Massachusetts Institute of Technology, Cambridge, MA, USA* (from December 16, 2016 to December 15, 2017).

The methodology of DBT project had three sections as below;

- The implementation of a numeric matrix model ($2 \times 4 \times 3$)
- ART, ART+TV_{3D}, and ART+TV_{3D}+MM for an analytical phantom ($61 \times 61 \times 9$)
- FBP, ART, ART+TV_{3D}, and ART+TV_{3D}+MM for the real images of CD Pasmam 1054 breast phantom ($601 \times 472 \times 8$)

5.1.1 A numeric matrix model and an analytical phantom

A three-dimensional (3D) matrix model (numeric model - $2 \times 4 \times 3$) of a breast was created by Matlab R2014a software program. It was the basic code of Siddon and ART. Numeric model was a 3D phantom ($2 \times 4 \times 3$) that had both indices and voxel intensities of related indices as 1, 2, 3, 4, 5, 6, 7, 8, 9, 10, 11, 12, 13, 14, 15, 16, 17, 18, 19, 20, 21, 22, 23, and 24. The dimensions 2, 4, and 3 of the 3D phantom were rows (z-axis), columns (y-axis), and layers (x-axis), respectively. What was implemented in Matlab is illustrated in Figure 5.1. An X-ray source was placed at point (0,0,100) and 5x6-size detector was accepted as a plane, which placed parallel to xy -plane, at point $z = -2$, whereas the center of the 3D phantom ($2 \times 4 \times 3$) was placed at origin (0,0,0). In the first step, X-ray source was kept stable only at point (0,0,100).

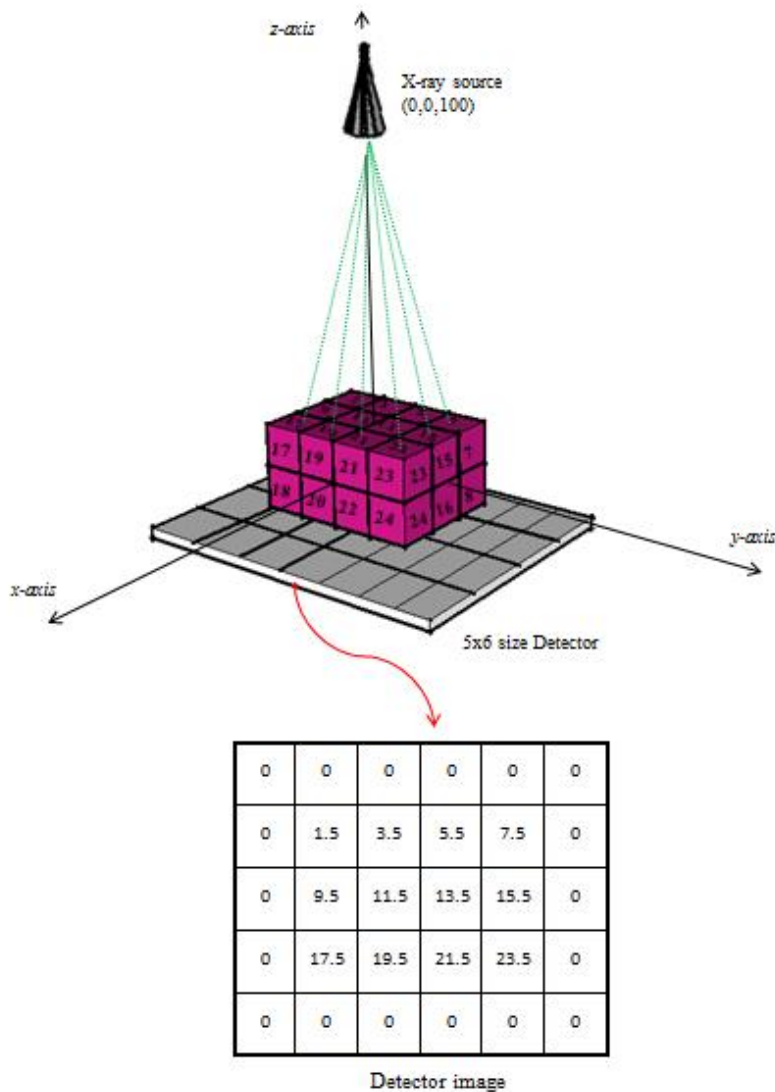


Figure 5.1 : The schematic of the simulation of Siddon’s matlab implementation.

Siddon algorithm was implemented to this model to obtain the projections of 2x4x3-dimensions breast model. These projections were acquired in a limited view angle between -45° and 45° with 5° angle step size as mimicing actual tomosynthesis systems. Under this scanning angle condition, 19 projections were acquired.

Each line of X-ray beam intersected the two rows of the phantom as equally weighting factor which was one. Because of the ratios of intersection length of each X-ray line were coequal, the contribution of voxel intensities, which were hit by the same X-ray line, were also similar. The values of detector pixels were computed by calculating voxel intensities taking into account weighting factor of intersections. Weighting factors were normalized and for this situation they were 0.5 value each.

5.1.2 Real breast phantom and images

In this section, using a real breast phantom, we proposed the implementation of the MM algorithm to the 3D DBT imaging problem, which was called MM based 3D TV regularized ART (ART+TV_{3D}+MM). ART, ART+TV_{3D}, and the proposed method ART+TV_{3D}+MM were executed for the real phantom (CD Pasmam 1054), which mimics a real 3D breast, scanned using Siemens MAMMOMAT. Experiments were evaluated both qualitatively and quantitatively by performing the tasks on MATLAB R2015b. We called iterative reconstruction techniques (IRT) for all ART, ART+TV_{3D}, and ART+TV_{3D}+MM.

Additionally, using 12 different radiation doses for the real breast phantom, we further investigate the effect of the radiation dose increase in DBT by applying IRT in comparison with Siemens MAMMOMAT's FBP method. Siemens MAMMOMAT reconstructs via its know-how unknown filtered back projection (FBP) method. The FBP method used in the comparisons in this thesis was Siemens MAMMOMAT's FBP method.

Using a Siemens MAMMOMAT Inspiration system (Siemens AG, Healthcare Sector, Erlangen, Germany), we acquired 25 projections of CD Pasmam 1054 phantom (Southern Scientific Ltd, West Sussex, United Kingdom). All acquisitions were performed at Hospital da Luz S.A., Lisbon, Portugal. The equipment acquired the projections with short X-ray pulses at angles of (-25.19°, -22.98°, -20.78°, -19.12°, -17.22°, -15.14°, -13.45°, -11.41°, -9.54°, -7.48°, -5.63°, -3.55°, -1.92°, 0.29°, 2.23°, 4.00°, 5.79°, 7.84°, 9.99°, 11.64°, 13.49°, 15.6°, 17.76°, 18.92°, 21.77°) with 28 kVp at 12 different levels of radiation doses in mAs values of 56, 63, 71, 80, 90, 100, 110, 125, 140, 160, 180 and 199.

We reconstructed the projections acquired via MAMMOMAT by performing ART with one iteration. The voxel values of the 3D image for each projection were updated ray by ray, and for all 25 projections the updating was repeated to complete a single iteration. Then we performed compressed sensing based image reconstructions (ART+TV_{3D}, and ART+TV_{3D}+MM). During each iteration, first 3D TV minimization (TV_{3D}) expressed in (4.34) (Ertas et al., 2013a; Polat & Yildirim, 2018; Sidky et al., 2008), was applied to the 3D image reconstructed by ART (ART+TV_{3D}), and then MM algorithm was applied to ART+TV_{3D}, called ART+TV_{3D}+MM as well.

The geometry of Siemens MAMMOMAT is illustrated in Figure 5.2. MAMMOMAT scans the breast over an angular range of approximately 47° to acquire 25 projections with short X-ray pulses. For more details about MAMMOMAT, see Siemens AG, 2016 and Siemens MAMMOMAT Inspiration, 2017. The real angular scanning system of Siemens MAMMOMAT was taken into consideration to design the ray geometry of the project.

As shown in Figure 5.2, a general DBT system has three major sections; a moving X-ray source, a pair of compression plates, and a static detector. In the Siemens MAMMOMAT, the distances between X-ray source to the detector, the rotation point of the source to the detector, and the bottom compression plate to the detector are 650 mm, 47 mm, and 17 mm, respectively. The XY-dimension of the detector is 3584x2816 pixels (Siemens AG, 2016; Siemens MAMMOMAT Inspiration, 2017).

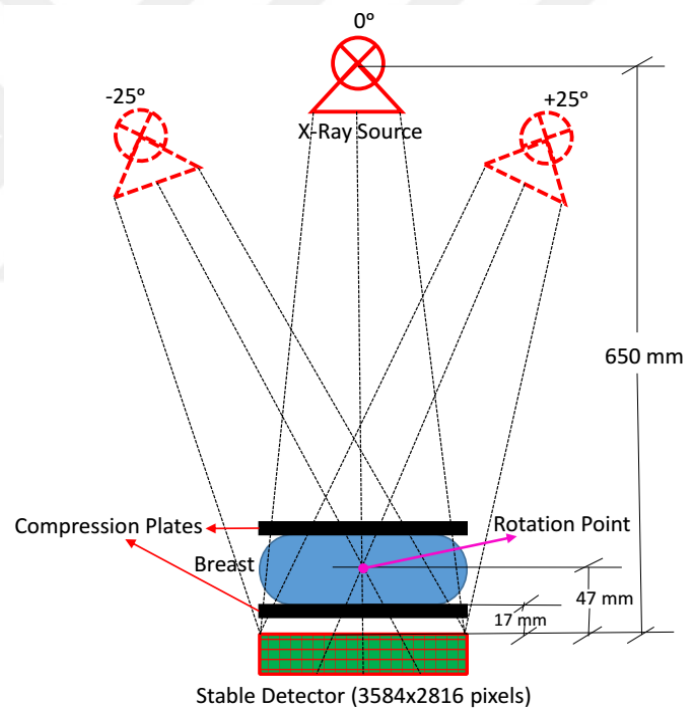


Figure 5.2 : The geometry of DBT system of Siemens MAMMOMAT (Polat et al., 2016; Polat & Yildirim, 2018).

ART was used to reconstruct these 25 projections by applying one iteration. In each projection, the values of the 3D image's voxels were updated ray by ray, and the updating was repeated for all 25 projections to complete a single iteration.

Due to the limitations of Matlab program, and computer capacity such as out of memory error and time cost, we run all algorithms for down-sampled projections as

601x472 pixels. We reconstructed 25 down-sampled projections of the real phantom CD Pasmam 1054 with dimensions 601x472 as 8 slices of third dimension in z-direction in this project. The results of these reconstructed images were compared for 12 dose levels by choosing layer-1 as the layer of interest (LOI). We chose the regularization coefficients (λ) of TV_{3D} as 5. A preset value for TV regularization term was used at all reconstructions. Ideally, it is well known that regularization term should be selected inverse proportional to signal to noise ratio (SNR) (Ahmed et. al., 2002; Yildirim et. al, 2009).

5.1.3 Algorithms to overcome out of memory and speed problems

We performed all tests using Matlab R2015b running on computer-1 that had Intel ® Core™ i7-4600U CPU@ 2.1 GHz, 2.70 processor, 8 GB RAM, and 64 bit processing Windows system, and on computer-2 that had two Intel Xeon E5_2660 CPUs@ 2.2 GHz with total of 16 cores, 64 GB RAM, two Tesla K20 NVIDIA cards and 64 bit CentOS 6.4 system. Our matlab code followed three main steps; the first step calculated the intersection lengths and their indices, the second step built the system matrix, and the third step performed ART, ART+TV_{3D} and ART+TV_{3D}+MM methods. Implementation of the pseudocode of the algorithm is given below.

1. Calculations of the intersection lengths and its indices via Siddon's algorithm (Siddon, 1985) for lattice structure of the 3D breast.
 - Describe parameters, dimensions of the lattice structure, rotation geometry, and ray geometry
 - Approach: use sparse allocation, cell and structure functions. Allocate the memory in column-wise to speed up calculations.

```
>> for 25 scanning angle
```

```
    >> for each row&column of detector pixel
```

```
        Run Siddon's algorithm
```

```
        Get "intersection lengths" and "voxel indices"
```

```
    >> end
```

```
>> end
```

2. Building the System Matrix-A

- Approach: use parfor parallel computing

```
>> parfor 25 scanning angle
```

```
Assign "intersection lengths" to "rays (i)" and "voxel indices (j)"
```

```
Get transpose of A-matrix with dimensions-(voxels x rays) (j x i)
```

```
>> end
```

3. Implementation of the ART, ART+TV_{3D} and ART+TV_{3D}+MM

- The study adopts the standard ART algorithm with a change in [6]. Perform ART formula in 5 steps.

```
>> for iterations
```

```
>> for 25 scanning angle
```

```
>> for i: each row&column of detector pixel
```

```
Get transpose of transpose of A-matrix with dimensions – (rays x voxels) A(i x j)
```

```
Calculate ART formula in 5 lines instead of 1 line
```

```
Norm=diag(A'*A);
```

```
AV=A(:,i); // transpose of A (j X i)
```

```
Q=Y(i)-AV*XR; // transpose of transpose of A
```

```
Constant=AV/Norm(i);
```

```
XR=XR+Q*Constant;
```

```
% XR=XR+(Y(i)-A(:,i)*XR)/Norm(i)*(AV');
```

```
>> end
```

```
>> end
```

```
Apply ART+TV3D and ART+TV3D+MM to ART
```

```
>>end
```

5.2 Data and Methodology for Micro-Bioimaging (MBI)

The studies in micro-bioimaging (MBI) part of this Ph. D. thesis were performed at *Harvard Medical School, Harvard-MIT Health Sciences and Technology, Massachusetts Institute of Technology, Cambridge, MA, USA* (from December 16, 2016 to December 15, 2017).

The methodology of MBI project had five sections as below;

- Creating manual scanning imaging tool
- Creating robotic scanning imaging tool
- Manufacturing biological phantoms
- Manufacturing a real bioreactor
- Performing ART+TV_{3D} for 3D image reconstruction of two biological phantoms (200x200x50)

5.2.1 Introduction to bioimaging

Bioimaging relates to methods that non-invasively visualise biological processes in real time. Bioimaging aims to interfere as little as possible with life processes. Moreover, it is often used to gain information on the 3D structure of the observed specimen from the outside, i.e. without physical interference. In a broader sense, bioimaging also includes methods visualising biological material that has been fixed for observation.

In cell biology, bioimaging can be used to follow cellular processes, quantify ion or metabolite levels and measure interactions of molecules live where they happen. Appropriate tracers, e.g., specific fluorochromes, and advanced microscopic instruments as e.g. confocal laser scanning microscopes (CLSM) are a prerequisite for most applications (Url-10, 2017).

Bioimaging is a term that covers the complex chain of acquiring, processing and visualizing structural or functional images of living objects or systems, including extraction and processing of image-related information. Examples of image modalities used in bioimaging are many, including: X-ray, CT, MRI and fMRI, PET and High Resolution Research Tomograph (HRRT) PET, SPECT, Magnetoencephalography (MEG) and so on. Medical imaging and microscope/fluorescence image processing

are important parts of bioimaging referring to the techniques and processes used to create images of the human body, anatomical areas, tissues, and so on, down to the molecular level, for clinical purposes, seeking to reveal, diagnose, or examine diseases, or medical science, including the study of normal anatomy and physiology. Image processing methods, such as denoising, segmentation, deconvolution and registration methods, feature recognition and classification represent an indispensable part of bioimaging, as well as related data analysis and statistical tools (Url-11, 2017).

5.2.2 Imaging system for micro-bioimaging (MBI)

In this section, we revised and adapted current algorithms that we have developed in DBT image reconstruction to compressed sensing based image reconstruction in 3D imaging systems for micro-bioimaging (MBI). Our aim by transforming of ART+TV_{3D} from DBT application to MBI application is illustrated in Figure 5.3. We revised our MATLAB code to reconstruct 3D images of biological samples with size 200x200x50.

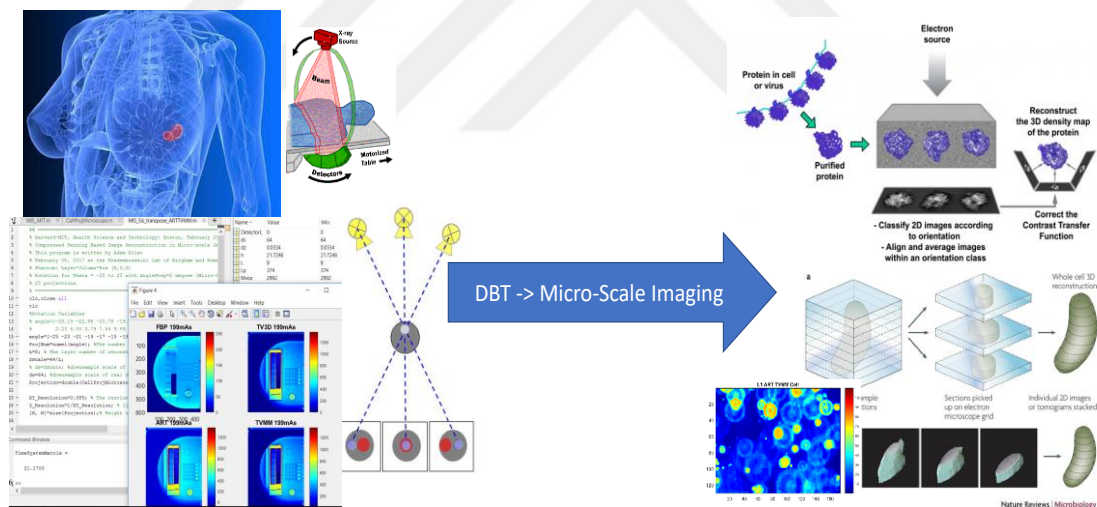


Figure 5.3 : 3D image reconstruction of biological applications.

To achieve the aims introduced above, we designed and created a 3D bioimaging system for biological applications. The concept of 3D bioimaging system is shown in Figure 5.4. It had mainly three parts as DBT: a complementary metal oxide semiconductor (CMOS) detector with a lens, a light source (can be a light emitted diode (LED)), and a holder for the biological sample. The design of optical imaging part which includes CMOS and lens is shown in Figure 5.5.

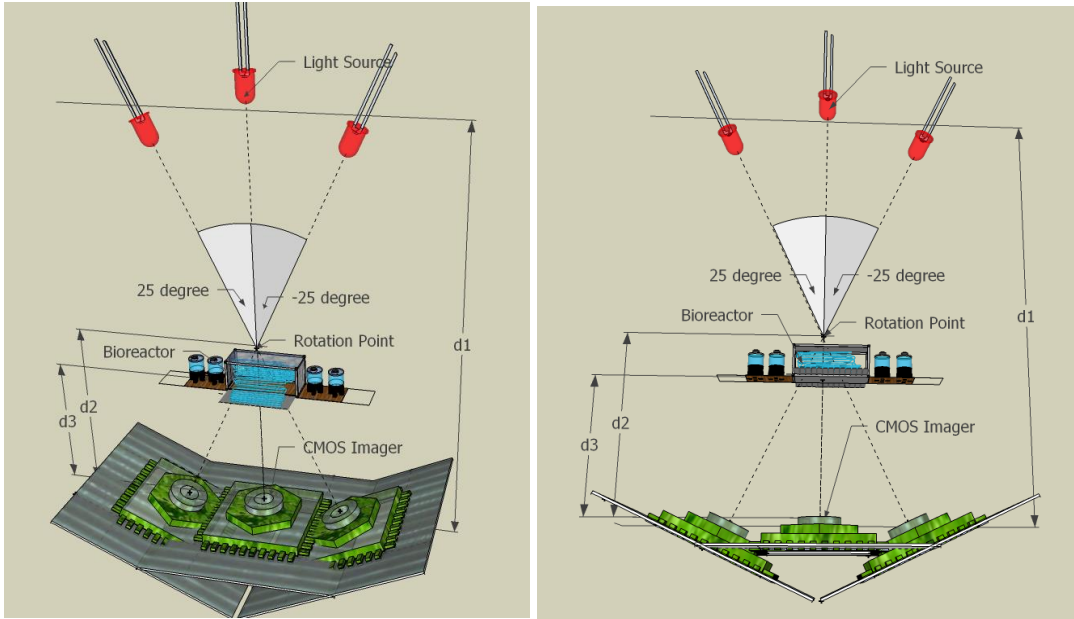


Figure 5.4 : The concept of 3D bioimaging system for micro-scale biological applications. The acquisition of projections was done between -25 and +25 degrees with 5-degree angle step.

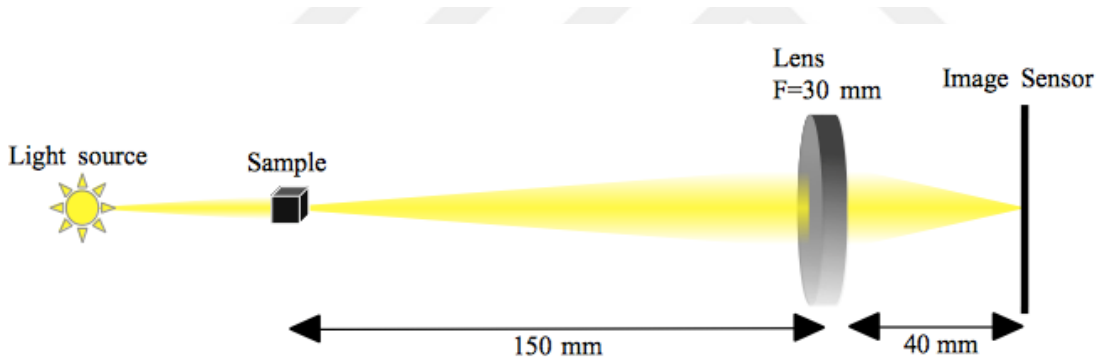


Figure 5.5 : Optical imaging design.

The distances from the sample to the lens and from the lens to the CMOS (image sensor) were setup as 150 mm and 40 mm, respectively. We utilized an achromatic lens with 10 mm diameter, 30 mm focal length, and visible-near infrared coated (Url-9, 2017) and it is illustrated in Figure 5.6. The basic specifications of the lens are given in Table 5.1. All specifications of the achromatic lens can be found in (Url-9, 2017).



Figure 5.6 : Achromatic lens.

Table 5.1 : The basic specifications of the lens.

Diameter	10.0 mm
Effective focal length (FL)	30.0 mm
Back focal length	27.47 mm
Center thickness 1 & Center thickness 2	3.5 mm & 2.0 mm
Radius 1 & Radius 2 & Radius 3	18.58 mm & -13.17 mm & -37.11 mm
Wavelength range	400-1000 nm
Focal length specification wavelength	587.6 nm

For image sensor Logitech C160 CMOS was used. The CMOS is shown in Figure 5.7 and its specifications are shown in Table 5.2.



Figure 5.7 : Logitech C160 CMOS.

Table 5.2 : The specifications of Logitech C160 CMOS.

Lens and sensor type	Plastic, CMOS
Focus type	Manual
Field of view (FOV)	50°
Focal length	40 cm (15.75 inch)
Optical resolution (true)	640x480 VGA
Image capture (4:3 SD)	320x240, 640x480, 1.3P
Frame rate (max)	15fps @ 640x480
Video capture (4:3 SD)	320x180, 360P

5.2.3 Creating the manual scanning 3D bioimaging tool

We designed and built a limited view manual scanning tool for 3D micro-bioimaging system using PMMA (polymethylmethacrylate) by CorelDRAW and laser cutter. The manual scanning tool which includes CMOS, lens, and light source is illustrated in Figure 5.8. It was able to manually rotated between maximum -45° and $+45^\circ$ with 5° angle steps, which means it was able to acquire maximum 19 projections in an examination.

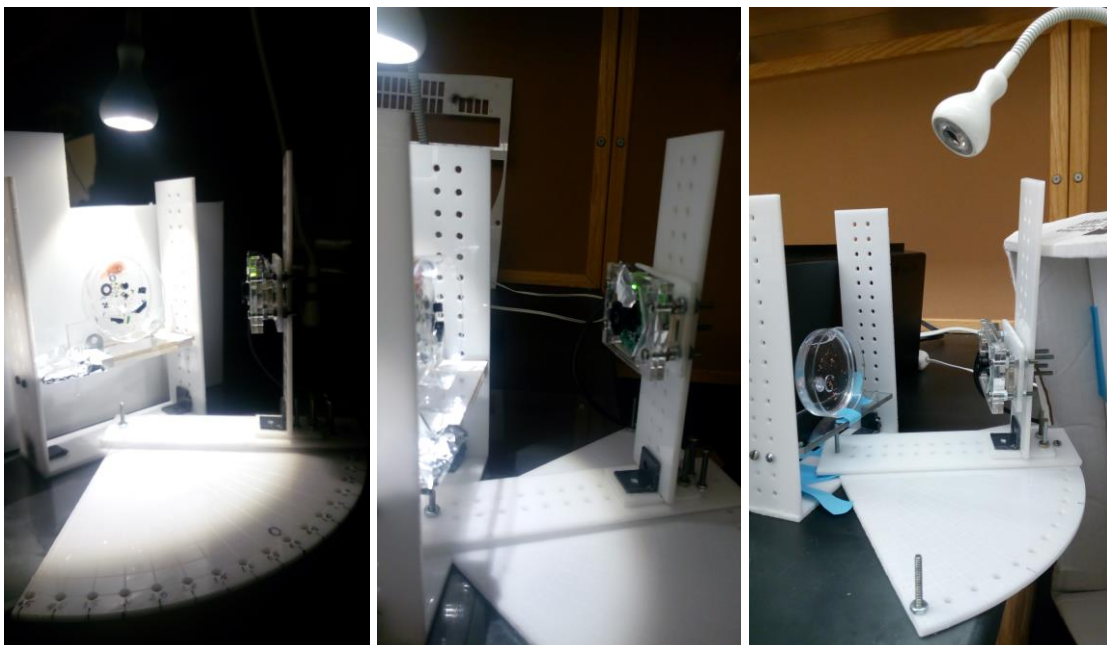


Figure 5.8 : Manual scanning tool. Between -45 and $+45$ degrees with 5 degree angle step.

5.2.4 Creating the robotic 3D micro-bioimaging (MBI) tool

After getting promising results via manual scanning imaging tool, we created an automatic image scanning tool controlled by robotic. The robotic 3D micro-bioimaging (MBI) tool was done by Arduino software and motor controls and is shown in Figure 5.9. We also designed a more advanced optical imaging setup using a combination of optical table and tools compared to that of manual scanning tool. By this tool, we improved the geometry of the projection acquisition and the quality of the images.

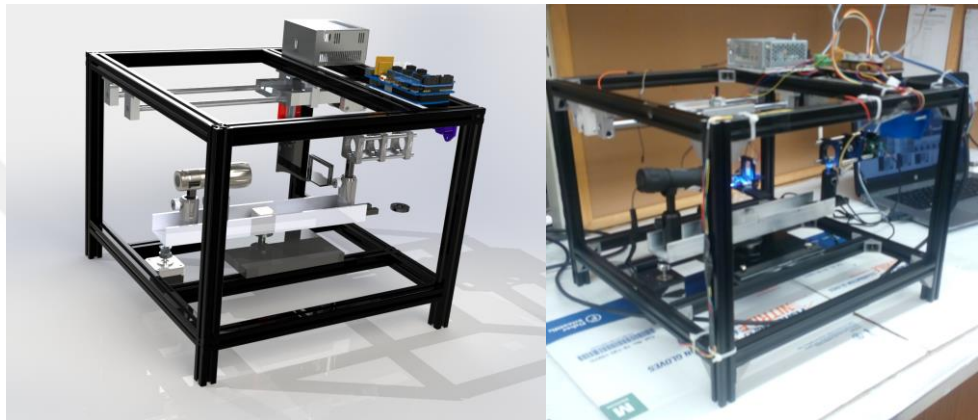


Figure 5.9 : The animation (left) and photo (right) of the robotic 3D micro-bioimaging (MBI) tool.

The size of the robotic 3D MBI tool was 35cmX35cmx30cm. It included one CMOS imager, one lens, one Arduino Mega 2560 R3 board, one RAMPS 1.4 board, three motor drivers, one light source, two stepper motors, one linear motor, and one power supply (see Figure 5.6, 7, 9-11).

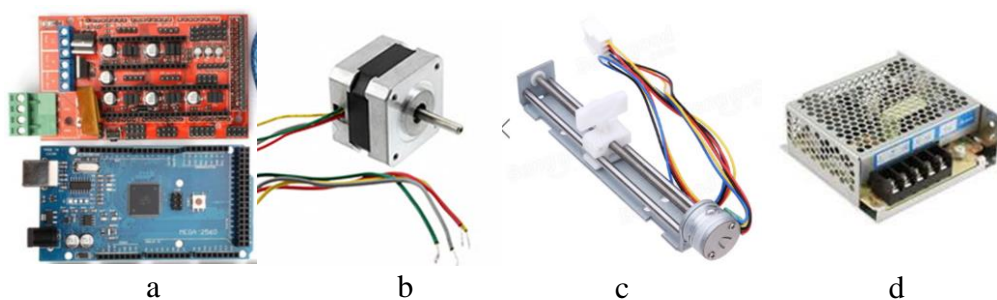


Figure 5.10 : a. Arduino Mega 2560 R3 (ATMEGA1280 combo) and RAMPS 1.4 board, b. stepper motor, c. linear motor and d. power supply.

5.2.4.1 Mechanical design

The robotic 3D MBI tool was built from scratch according to the specifications that were needed for a smooth and precise image acquisition. The chassis of the structure was built from 20mm T-slotted black anodized aluminum which provided enough support for the rotating axis. The T-slots were joint using aluminum corner brackets to ensure the integrity of the chassis and to have versatility in case the structure had to be changed. The design was based on a mix between a computer numerical control (CNC) machine and a 3D printer. A couple rails were used for the forward and backwards degree of motion of the platform that holds the bioreactor sample. On top of the rails a platform was set and adapted to it a fitting that carried another platform which in turn holds the sample to be scanned. In the lower part of the chassis a rotating axis was constructed, this to ensure that the CMOS-detector could have a range of degrees of freedom along this rotating axis, also the CMOS-detector was set in-line with the light source on top of a platform which was in turn set on top of the rotating axis as shown in Figure 5.9. The rotating axis was a swivel table-top which gave it the degrees of freedom needed. The platform on top of the rotating axis is a 1-foot aluminum U-shaped bar. Most of the fittings involved were custom made for the project using a filament (fused deposition modeling (FDM)) 3D printer.

For the locomotion steppers motors were chosen because of their characteristics of precision and stability. The two main motors were the ones used for rotating the swivel table and to move the platform on top of the couple of rails, NEMA 17 stepper motors with 12V of rated voltage were used for this purpose. To lower and raise the sample and to move the CMOS along the rotating axis, small micro-stepping linear motors with 9V of rated voltage were used, an additional motor was used depending on the sample with additional fittings. The versatility of having different kind of fittings at a very low cost was one of the advantages of the design.

5.2.4.2 Electronics design

To provide enough control and stabilization to the four to five stepper motors that were to be used it was imperative to have an electronics and control platform that was sufficient for this endeavor, as previously stated the design was based partially on CNC machines and 3D printers so to drive the steppers we used a RAMPS 1.4 board and ATMEGA1280 microcontroller combo (Figure 5.10) which is commonly used in 3D

printers. The RAMPS board was fitted with A4988 stepper motor drivers (Figure 5.11) and in the case of the ones controlling the micro-stepping linear motors the current was limited to 500mA with the in-built potentiometer of each driver. Everything was powered via a 12V power supply also adapted to the chassis with custom 3D printed fittings.

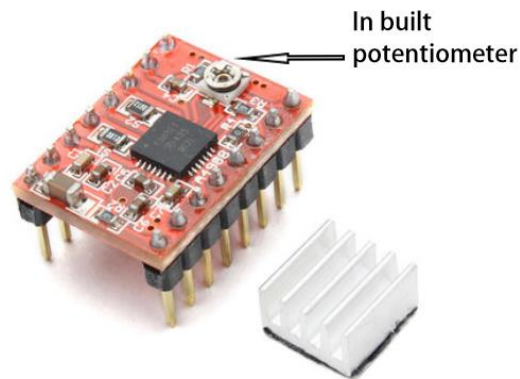


Figure 5.11 : A4988 stepper motor driver.

5.2.4.3 Software implementation

The microcontroller programming was done using a C++ code compiler. However, the control of the motors was implemented via a Matlab™ Graphical User Interface (GUI) in order to have versatility when controlling the device as the scanning software was also developed in this coding language. The communication was done via serial as the code in the microcontroller was made to respond to inputs via its serial port. This was preferred instead of managing all the control just from Matlab™ because as the motors require a very constant and specific signal to work properly as they are stepper motors, controlling directly through Matlab™ turns out to be too slow for the proper functionality of the motors. This because of the delays and the kind of processing that Matlab™ has to work under. Matlab™ takes a lot of time between signals as it has to process everything via software which depends on the computing power of each PC. Adding to this it must open and close the serial communications port, write to it and process all this information. All these processes make the use of signals through Matlab™ software too slow to be used with stepper motor which require a specific delay and a faster signal to work properly.

5.2.5 Lab-on-a-chip

The miniaturization of electronic components has attracted more attention in the field of advanced fabrication techniques for micro- and nano-scale devices. Lab-on-a-chip (LOC) is a device such as a microfluidic platform that integrates complex functions of the chemical systems and laboratory functions onto an integrated circuit. These are only from a few millimeters to a few square centimeters in size to achieve automation and high-throughput screening. LOCs are designed to be equipped with software and/or optical detection systems to enhance their function. One of the most important advantages of LOCs is to accomplish *in vitro* tests with portable devices instead of a real-sized laboratory with cost effective manufacturing and operations. LOCs are applied to in the fields of biomedical, biological, health science, space and atmospheric sciences (Ghallab & Badawy, 2004, Uri-8, 2017; Volpatti & Yetisen, 2014).

5.2.6 Biological phantoms

The biological phantoms and bioreactors are the elements of the lab-on-a-chip. We manufactured a variety of biological phantoms as the sample of biological applications to scan and acquire projections. First, we produced several transparent media with PDMS (polydimethylsiloxane) with soft-lithographic techniques including masses to mimic a biological system such as a cancerous tissue. A few biological phantoms manufactured by PDMS are illustrated in Figure 5.12.

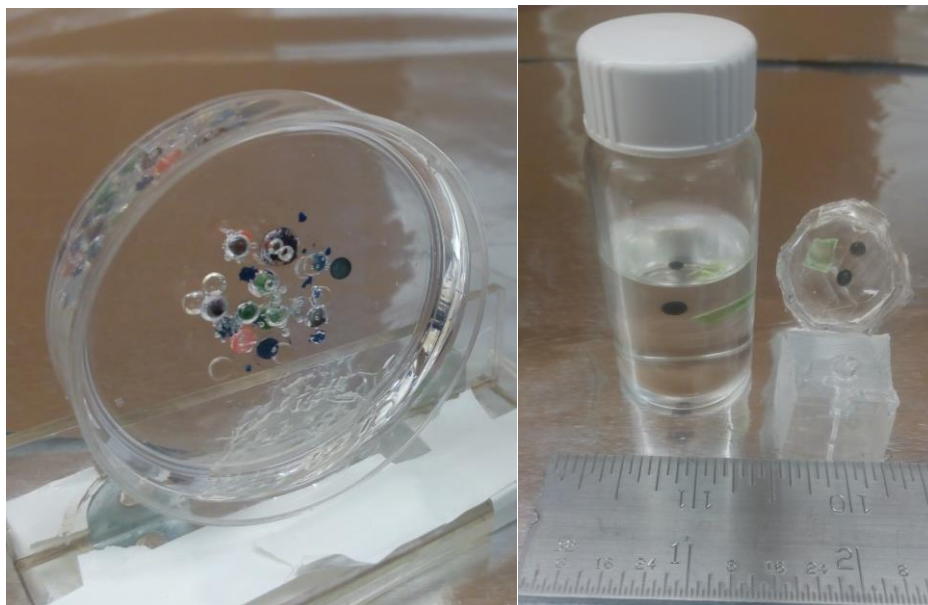


Figure 5.12 : A variety of biological phantoms in transparent media produced by PDMS.

PDMS is a low-density material used in the soft lithography for flow delivery in microfluidics chips. Hydrophobicity of the surface and high fracture toughness over a wide temperature range are among the important properties of PDMS. PDMS is also a transparent media having a refractive index of ~ 1.4 and an extinction coefficient of $< 10^{-10}$ in the visible range (240 nm – 1100 nm) which is convenient for optical absorption. Thanks to this feature of PDMS the light can pass through the media containing the object and acquire the images of that object on the CMOS (Whitesides & Tang, 2006).

Recently, most of the PDMS-based studies in nanotechnology and biomaterial applications have used Sylgard-184, which is commercially available two-component kit manufactured by Dow Corning. The picture of two components of Sylgard-184, silicone elastomer curing agent and silicone elastomer base, is illustrated in Figure 5.13. This material has opened up many doors on soft lithography so that made it as one of the indispensable material in this field.



Figure 5.13 : Sylgard-184 kit.

5.3 The Metrics for Quantitative Evaluation

For quantitative assessment of the 3D reconstructed images, metrics such as signal to noise ratio (SNR), structural similarity (SSIM), contrast to noise ratio (CNR) and 1-dimensional (1D) profile were used in this Ph. D. thesis. The definitions of these metrics are below.

SNR measures the ratio of the level of a desired signal and the level of background noise and expressed as in (5.1) (Ertas et al., 2013b).

$$SNR = 10 \log \left(\frac{\sqrt{\sum_{ijk}^{IJK} |\hat{X}_{ijk}^{IJK}|^2}}{\sqrt{\sum_{ijk}^{IJK} |X_{ijk} - \hat{X}_{ijk}^{IJK}|^2}} \right) \quad (5.1)$$

where X_{ijk} is original image, and \hat{X}_{ijk} is the reconstructed image. i, j, k are the number of the elements in the xyz directions, respectively.

SSIM, introduced by Wang et al. (2004) as a novel metric, measures the similarity between two images; in other words, *SSIM* index is the quality measure of one of the images being compared, provided that the other image is regarded as of perfect quality. Wang (2016) presented the MATLAB code for *SSIM*. The formulation of *SSIM* index is written in (5.2).

$$SSIM(x, y) = \frac{(2\mu_x\mu_y + C_1)(2\sigma_{xy} + C_2)}{(\mu_x^2 + \mu_y^2 + C_1)(\sigma_x^2 + \sigma_y^2 + C_2)} \quad (5.2)$$

In Eq. (5.2);

μ_x is the average of x

μ_y is the average of y

σ_x^2 is the variance of x

σ_y^2 is the variance of y

σ_{xy} is the covariance of x and y

C_1 and C_2 are defined in (5.2a) and (5.2b), respectively.

$$C_1 = (k_1 L)^2 \quad (5.2a)$$

$$C_2 = (k_2 L)^2 \quad (5.2b)$$

Where L is the dynamic range of the pixels (typically $(2^b - 1)$, b is the number of bits per pixel), $k_1 \ll 1$, $k_2 \ll 1$.

CNR is a metric, used in medical imaging, to determine image quality by distinguishing between intensities of an image. It is formulated by (5.3).

$$CNR = \frac{(\mu_{ROI} - \mu_{bgd})}{\sigma_{bgd}} \quad (5.3)$$

where μ_{ROI} and μ_{bgd} are the mean value of region of interest (ROI) and the mean value of background. σ_{bgd} is the standard deviation of background.



6. RESULTS AND DISCUSSION

The results of reconstructions for both digital breast tomosynthesis (DBT) and microbioimaging (MBI) studies are presented in this Chapter.

6.1 Results and Discussion for Digital Breast Tomosynthesis (DBT)

6.1.1 The results of IRT methods (ART, ART+TV_{3D}, and ART+TV_{3D}+MM) for an analytical phantom

The proposed method ART+TV_{3D}+MM was implemented for an analytical phantom with dimensions 61x61x9 that simulates a 3D breast roughly. Nine slices of analytical phantom with dimensions 61x61 that simulates a 3D breast are illustrated in Figure 6.1. Layer-3 was chosen as the layer of interest (LOI) due to the existence of fine details in this layer (Polat et al., 2016).

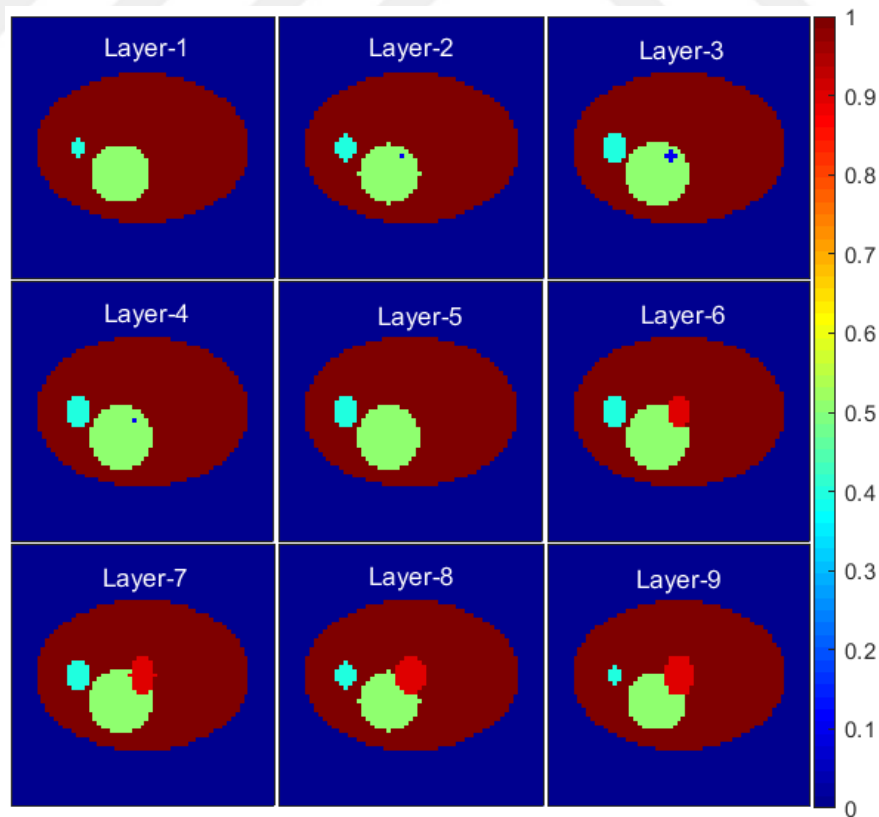


Figure 6.1 : Nine layers of the mimic of a 3D breast (61x61x9) (Polat et al., 2016).

In ART+TV_{3D}+MM method, we applied MM algorithm after 3D TV minimization step at each iteration. Here, 3D data was reshaped to 1D as input of MM algorithm after 3D TV minimization. MM algorithm has another inner iteration process in itself. We adapted the MM algorithm developed by (Selesnick, 2014) to our problem with five iterations.

The number of MM iteration was chosen as 5 based on the convergence criterion for stopping the iteration, *Variation* (%) expressed in (4.38).

The results of LOI (3th Layer) of ART, ART+TV_{3D} and ART+TV_{3D}+MM can be visually compared in Figure 6.2. The visual interpretation can be done by focusing on two objects of interest (OOI-A and OOI-B). While obtaining similar results in both ART+TV_{3D} and ART+TV_{3D}+MM, both methods outperformed ART. Among all methods, ART+TV_{3D}+MM has the lowest background noise level.

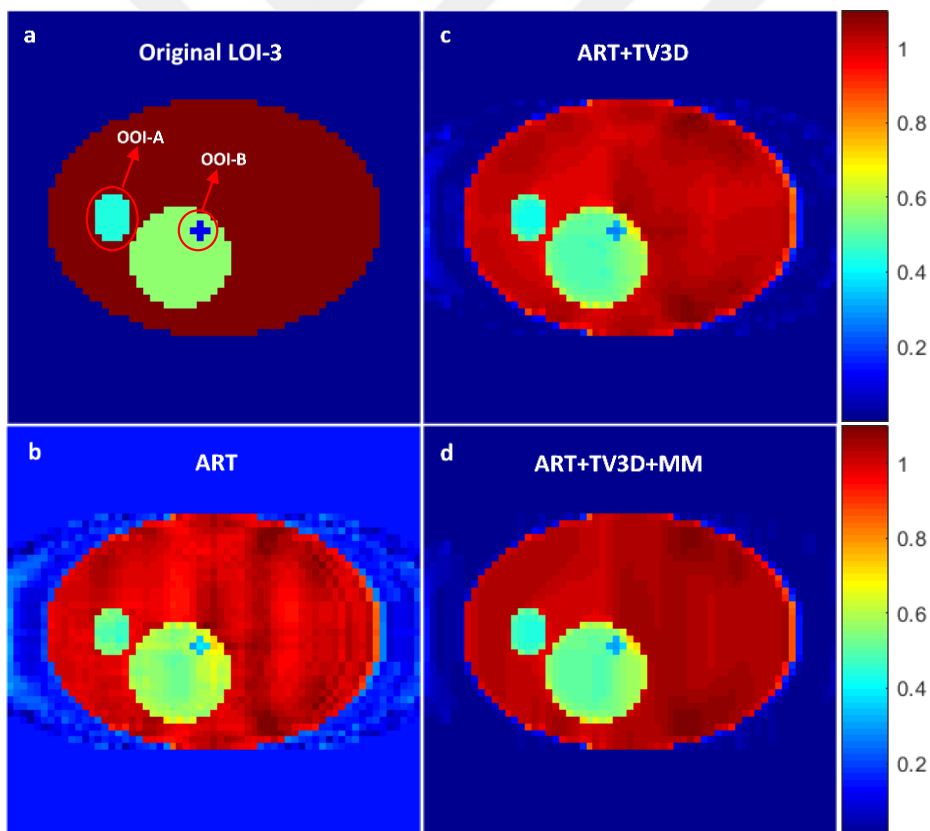


Figure 6.2 : a. Original LOI, b. the reconstructed LOI via ART, c. the reconstructed LOI via ART+TV_{3D}, and d. the reconstructed LOI via ART+TV_{3D}+MM.

Signal to noise ratio (SNR) and structural similarity (SSIM) of the LOI were examined as quantitative metrics to evaluate the performance of ART+TV_{3D}+MM method by comparing to ART+TV_{3D} and ART as well. The pilots of SNR and SSIM versus the number of iteration are given in Figure 6.3 and in Figure 6.4, respectively.

SSIM offers a metric which has a closer match with the human vision. Matlab code for SSIM can be accessed on (Wang, 2016).

While ART+TV_{3D}+MM reached to 0.9814 SSIM value at the end of the 10th iteration, SSIM values of ART+TV_{3D}, and ART were 0.9771 and 0.9208, respectively. Additionally, SNR (dB) values of ART+TV_{3D}+MM, ART+TV_{3D}, and ART were 24.56, 24.32, and 22.48, respectively. ART performed the poorest results for both metrics. In conclusion, the proposed method ART+TV_{3D}+MM helps in obtaining superior results in terms of SNR and SSIM values compared to ART+TV_{3D}.

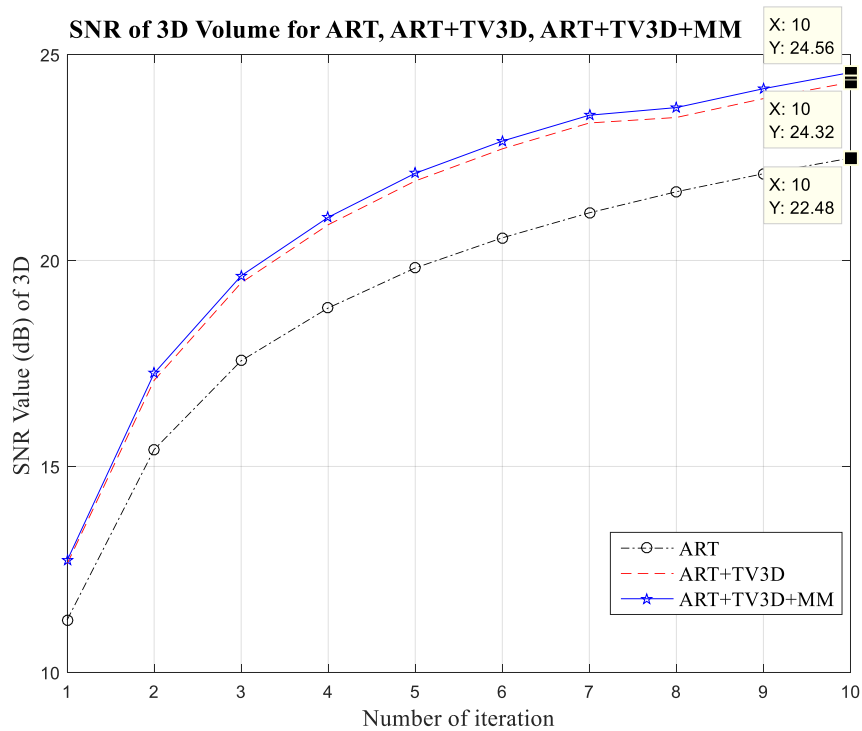


Figure 6.3 : SNR values (dB) of 3D volume for ART, ART+TV_{3D}, and ART+TV_{3D}+MM.

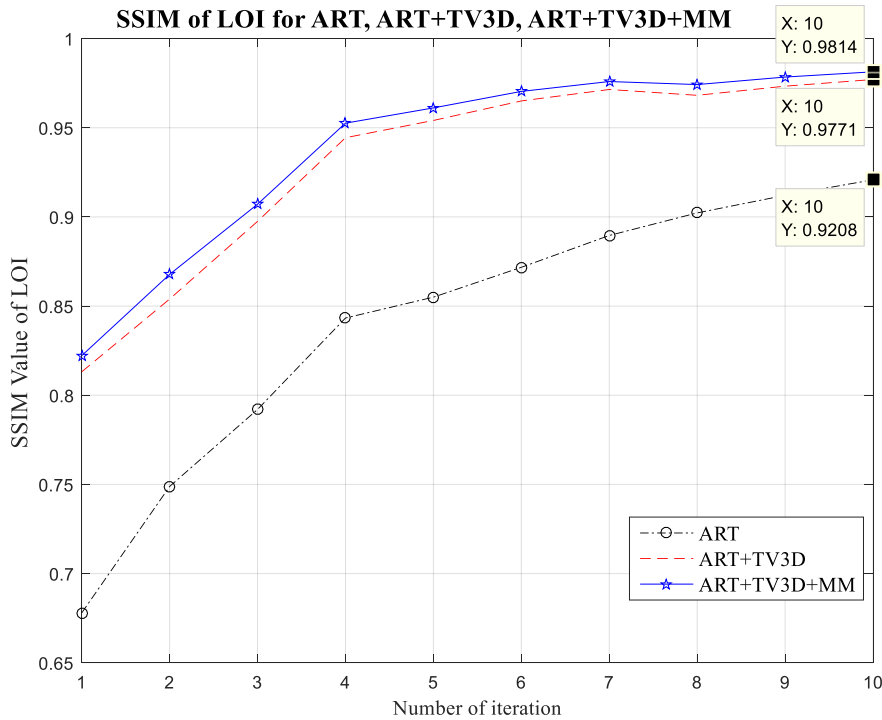


Figure 6.4 : SSIM values of ART, ART+TV_{3D}, and ART+TV_{3D}+MM.

6.1.2 The results of IRT methods (ART, ART+TV_{3D}, ART+TV_{3D}+MM) and FBP for the real breast phantom images

The effects of the dose and the reconstruction methods, which are ART, ART+TV_{3D}, ART+TV_{3D}+MM (iterative reconstruction techniques (IRT)), and MAMMOMAT's FBP on the quality of the reconstructed images of the real breast phantom (CD Pasmam 1054) were assessed both quantitatively and qualitatively using MATLAB R2015b at 12 different dose levels.

6.1.2.1 Reconstruction of 100 mAs-dose images

In this sub-section we analyzed only reconstruction of 100 mAs-dose image, evaluated qualitative and quantitative assessments for IRT and MAMMOMAT's FBP to compare the methods in detail for the same dose level chosen within the mid-range. The reference projection at 100 mAs-dose level at angle of 0.29° (center of moving arm) is shown in Figure 6.5. It includes OOI-1 (Object of Interest-1), OOI-2, OOI-3, OOI-4, 1D profile-A, and 1D profile-B which were used in quantitative analysis.

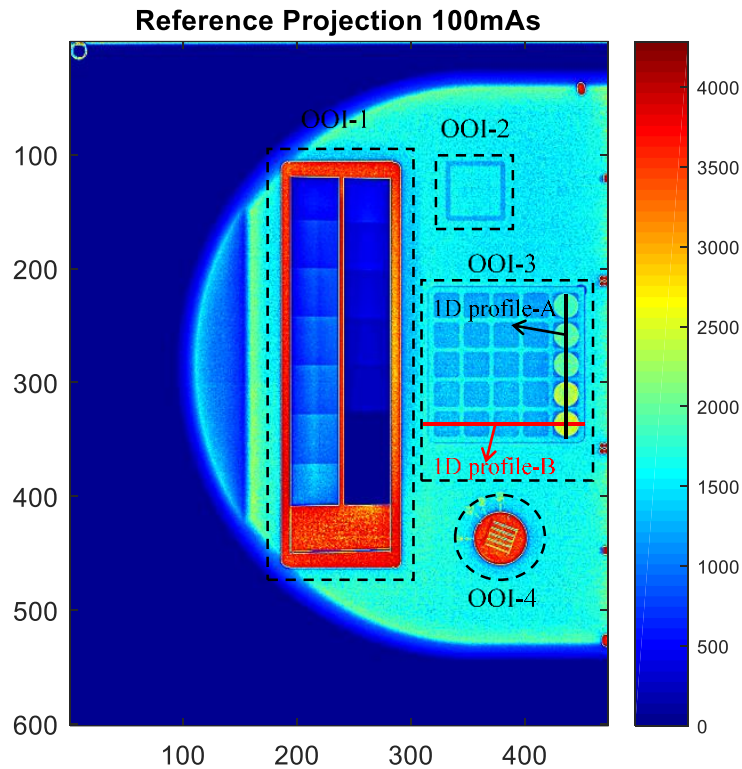


Figure 6.5 : The reference projection (601x472 pixels), the four OOIs and 1D profiles at 100 mAs-dose level at the angle of 0.29° .

In Figure 6.6, three projections; 1st projection at angle of -25.19° , 14th projection at angle of 0.29° (center), and 25th projection at angle of 21.77° are illustrated. If we draw a red line over the center of the circle-shape of the center projection, the images of projections on the detector shift versus the scanning angle from -25.19° to 21.77° can be seen clearly. This shifting causes a blurring effect on the reconstructed images.

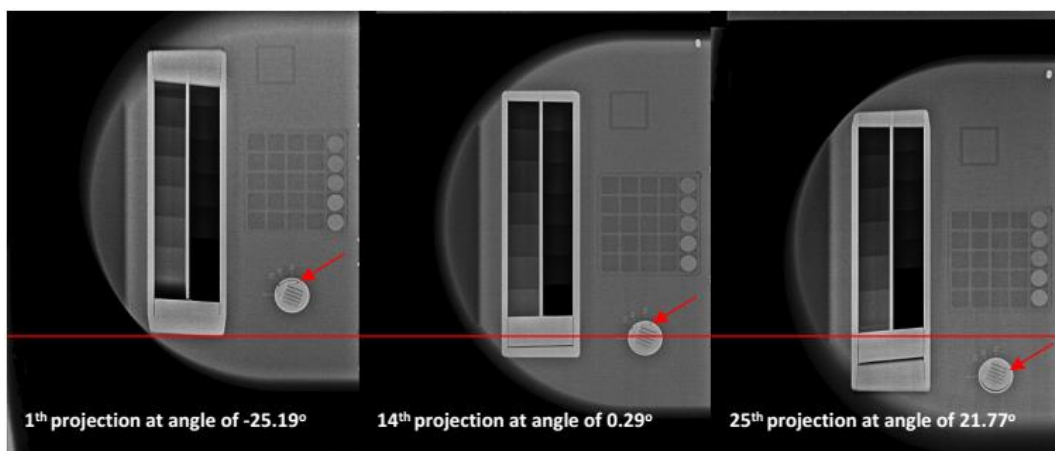


Figure 6.6 : 1st projection at angle of -25.19° (left), 14th projection at angle of 0.29° (center), and 25th projection at angle of 21.77° (right).

6.1.2.2 Visual analysis of 100 mAS-dose images

In this section, we presented the comparison of the outcomes of the reconstructed images of 25 projections of the real breast phantom CD Pasmam 1054 for the algorithms IRT with one iteration and MAMMOMAT's FBP. This comparison was done for 100 mAs (middle dose level) and is illustrated in Figure 6.7.

We performed visual and metric analysis of the reconstructed images of the methods, and compared the the effect of dose changes focusing on OOI-1, OOI-2, OOI-3, and OOI-4.

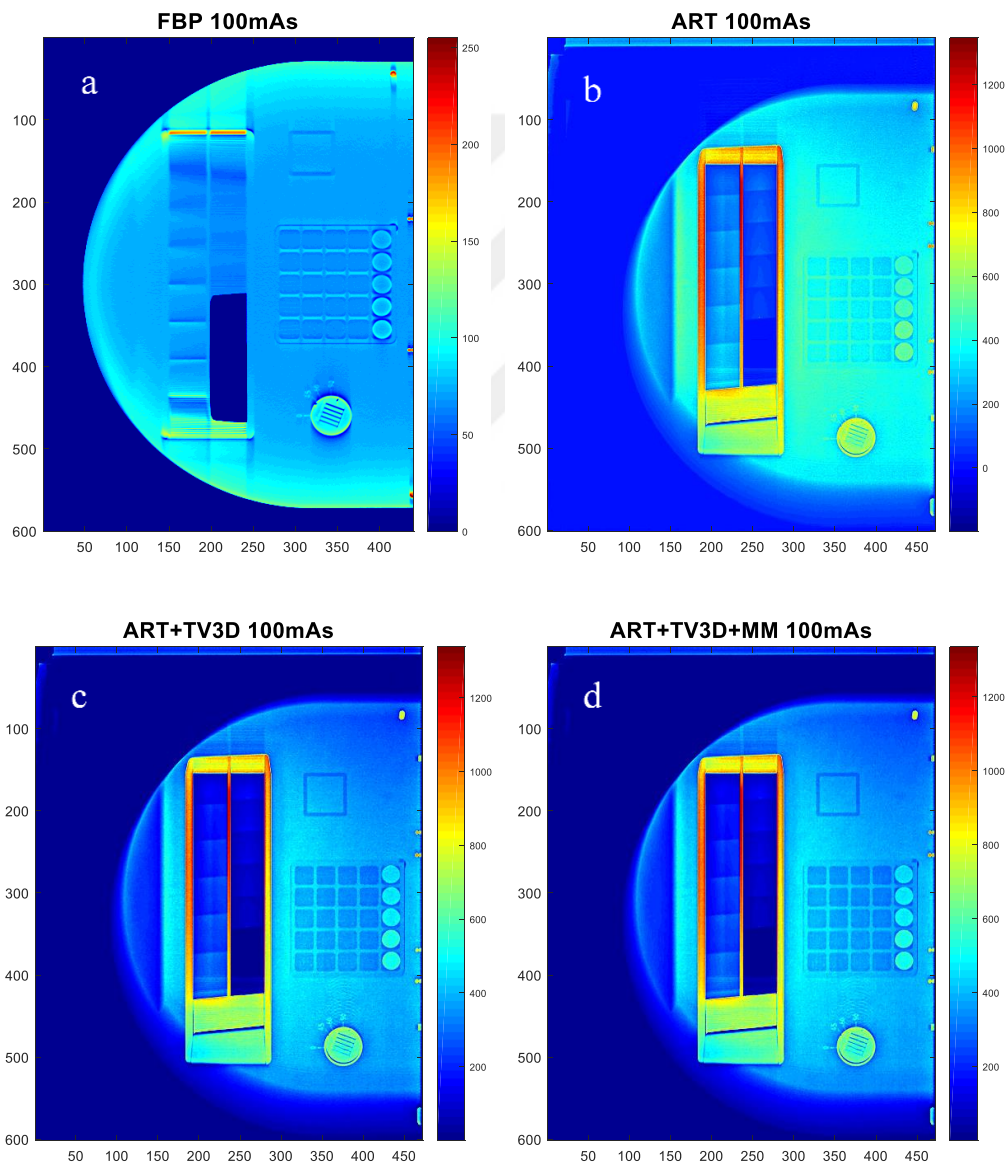


Figure 6.7 : a. FBP, b-d. IRT (b. ART, c. ART+TV_{3D}, and d. ART+TV_{3D}+MM) at 100 mAs.

When we evaluated the reconstructed images of four methods for 100 mAs in Figure 6.7, OOI-1 drawn on the reference projection in Figure 6.5 were visually similar for the three methods of IRT; however, they were better than FBP. Additionally, among IRT results for OOI-2, OOI-3, and OOI-4, ART+TV_{3D} and ART+TV_{3D}+MM gave improved results than ART. Moreover, although OOIs-1 of ART, ART+TV_{3D} and ART+TV_{3D}+MM showed no difference qualitatively, the metric analysis in next section proved that the result of ART+TV_{3D} and ART+TV_{3D}+MM was better than the result of ART. Enlargement of OOI-1 is illustrated in Figure 6.8. The enframed rectangular window shape clearly could be distinguished in the three methods of IRT, whereas the same shape was too unclear in FBP.

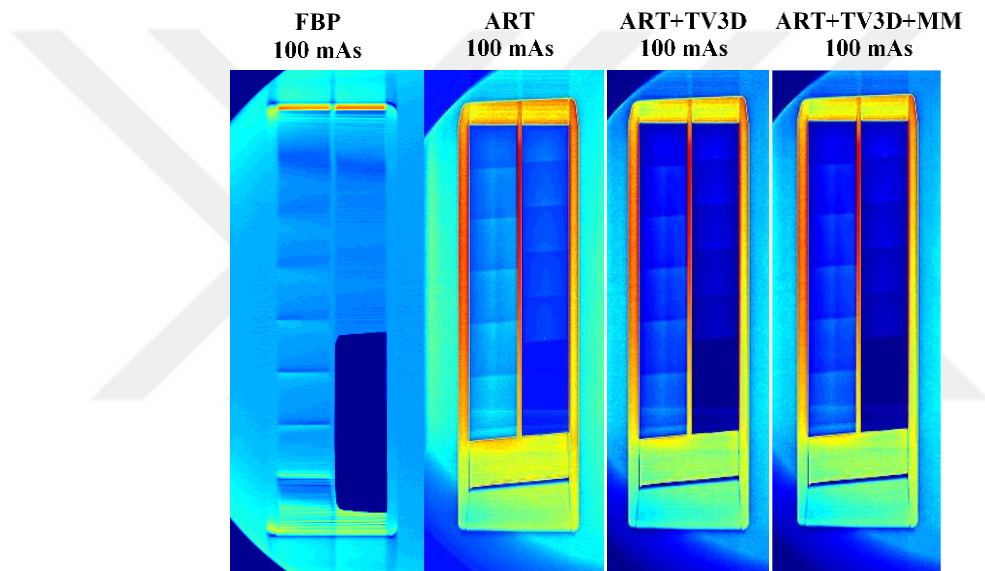


Figure 6.8 : Zoom in OOI-1 at 100 mAs-reconstructed images; FBP and IRT (ART, ART+TV_{3D}, and ART+TV_{3D}+MM).

In the same way, in the enlargement of OOI-2 in Figure 6.9, ART+TV_{3D} and ART+TV_{3D}+MM provided better images in terms of preserving the edges than the FBP and ART methods.

Our proposed method ART+TV_{3D}+MM increased the sharpness of OOI-2. Additionally, it was clear that the quality of detectability of the square-shape was much better for the three methods of IRT than FBP. In IRT methods, ART+TV_{3D}+MM that we proposed had similar quality as ART+TV_{3D}. Moreover, it was quite obvious that ART+TV_{3D}+MM was much better quality than ART.

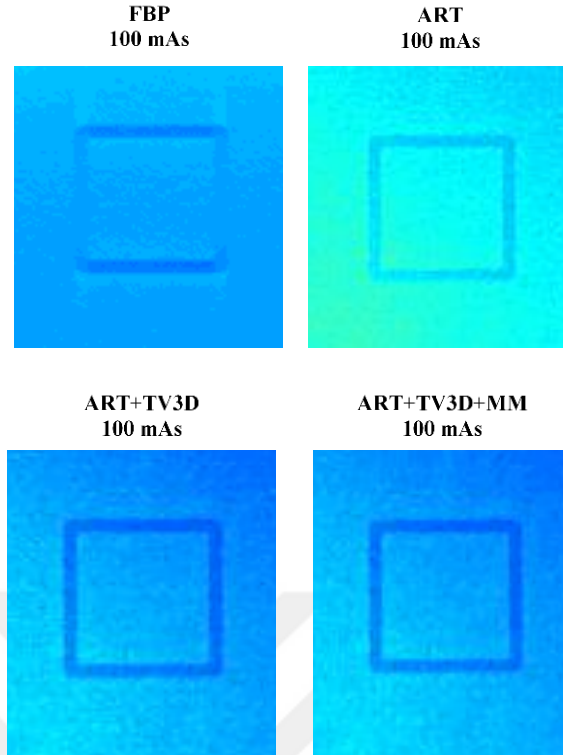


Figure 6.9 : Zoom in OOI-2 at 100 mAs-reconstructed images; FBP and IRT (ART, ART+TV_{3D}, and ART+TV_{3D}+MM).

6.1.2.3 Metric analysis of 100 mAs-dose images

To evaluate the performance of IRT comparing to FBP apart from qualitative assessment, quantitative metrics such as CNR defined in (5.3) and 1D profile of the LOI were examined as well.

ROI-1 (in OOI-1), ROI-2 (in OOI-2) and their background areas of ART+TV_{3D}+MM at 100 mAs are illustrated in Figure 6.10. The CNRs of the same ROI-1 and the same ROI-2 of four methods (three of IRT and FBP) are compared at 100 mAs in Table 6.1.

Table 6.1 : The CNR values of FBP and the three methods of IRT at 100 mAs.

	FBP	ART	ART+TV _{3D}	ART+TV _{3D} +MM
CNR of ROI-1	1.075	48.949	51.191	52.439
CNR of ROI-2	2.011	2.152	1.989	1.949

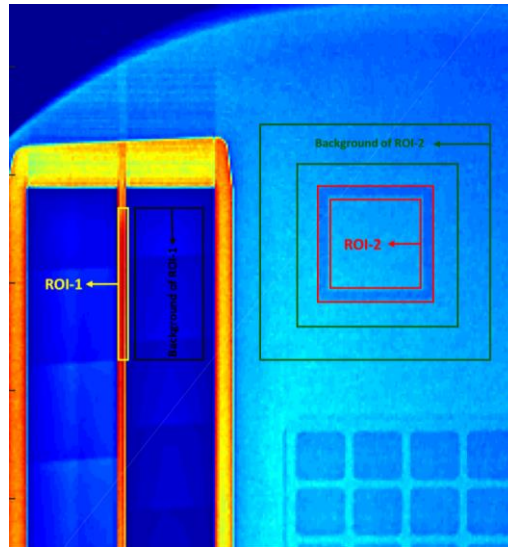


Figure 6.10 : ROI-1 (yellow), background of ROI-1 (black), ROI-2 (red), and background of ROI-2 (green).

In Table 6.1, the CNR values of ROI-1 for FBP, ART, ART+TV_{3D}, and ART+TV_{3D}+MM were 1.075, 48.949, 51.191, and 52.439, respectively. It could be seen that ART, ART+TV_{3D}, and our proposed method ART+TV_{3D}+MM had approximately 45-55 times better results when compared to FBP with ROI-1 evaluating with the CNR. The CNR values of ROI-2 of ART+TV_{3D} and ART+TV_{3D}+MM were less than the value of the FBP. This can be explained by the effect of down-sampling, applied to the images reconstructed by the FBP, in smoothing the background.

When we evaluated these CNR values of ROI-2 with Table 6.1 and Figure 6.9, although the values of CNR of ROI-2 (in OOI-2) for FBP and ART were better than the values of CNR of ROI-2 (in OOI-2) for ART+TV_{3D} and ART+TV_{3D}+MM, in visual assessment of OOI-2 for ART+TV_{3D} and ART+TV_{3D}+MM were better than FBP and ART qualitatively by giving better contrast and creating sharper edges.

For 1D profile comparison of IRT and FBP at 100 mAs, 1D profile-A shown in Figure 6.5 was chosen. 1D profile-A of four methods are given in Figure 6.11. ART+TV_{3D}+MM showed better performance than ART+TV_{3D}, ART+TV_{3D} showed better performance than FBP and FBP showed better performance than ART in terms of amplitudes indicating distinguishability of the circles in the reconstructed images.

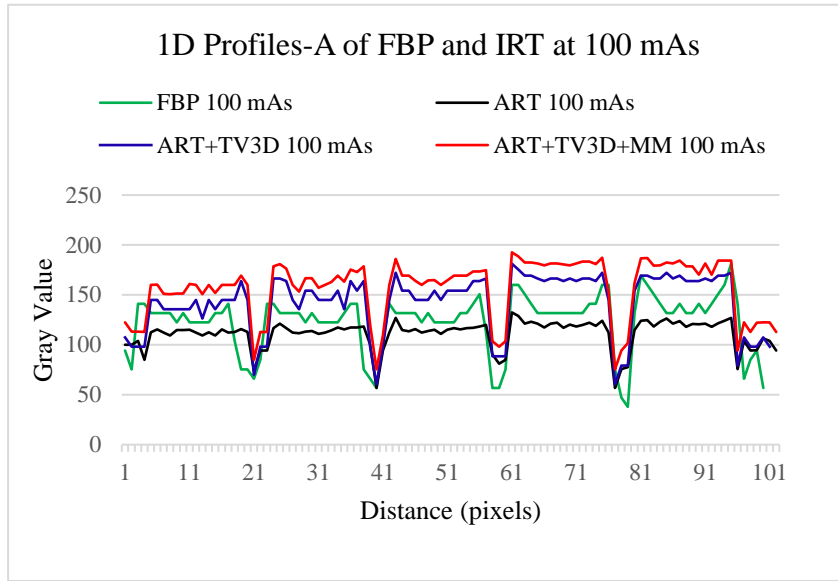


Figure 6.11 : 1D profiles-A of FBP and IRT (ART, ART+TV_{3D}, and ART+TV_{3D}+MM).

6.1.2.4 Reconstruction of 12 dose-level-images

After evaluating 100 mAs-dose images (the middle dose level), we also applied the reconstruction methods to all images of 12 different levels of radiation doses in mAs values of (56, 63, 71, 80, 90, 100, 110, 125, 140, 160, 180 and 199). In Figures A.1, A.2, A.3, and A.4 (Appendix A), we presented and compared the three methods of IRT (ART, ART+TV_{3D}, and ART+TV_{3D}+MM) and MAMMOMAT's FBP for all dose levels. Afterwards, to see more details we presented the results of IRT and FBP at 56 mAs (lowest dose level) and 199 mAs (highest dose level) with larger images as well.

6.1.2.5 Visual analysis of 12 dose-level-images

In this section, we also compared the results of the reconstructed images of 25 projections of the real breast phantom CD Pasmam 1054 for IRT with one iteration and FBP. This comparison was done for values of 12-dose levels (56, 63, 71, 80, 90, 100, 110, 125, 140, 160, 180, and 199 in mAs) and shown in Appendix A.

Here, we repeated visual inspection for all 12-dose levels in the same way as we did for 100 mAs-reconstructed images earlier. To see how a dramatic dose increase affected the reconstructed images, we presented the results of IRT and FBP for 56 mAs (lowest dose) and 199 mAs (highest dose) in Figure 6.12.

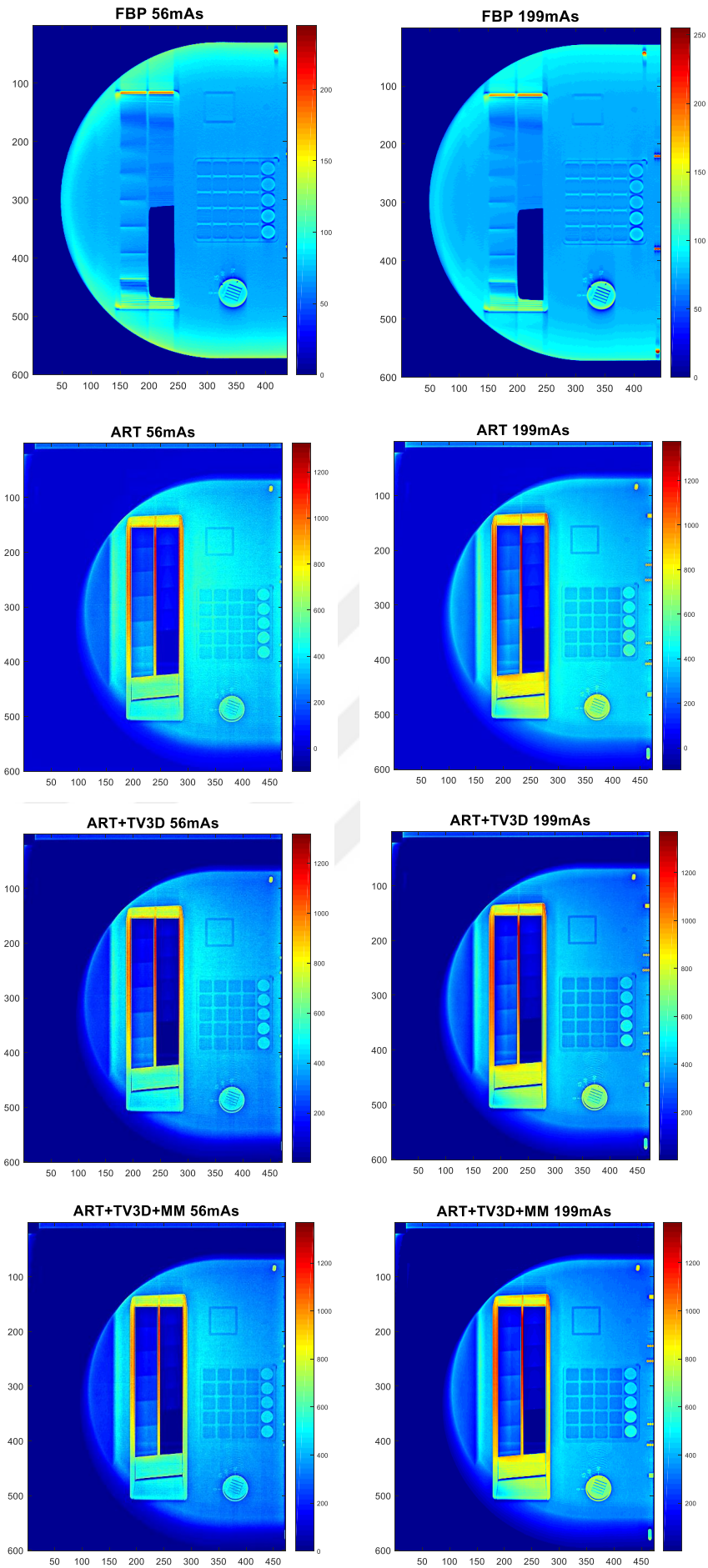


Figure 6.12 : FBP (1st row), ART (2nd row), ART+TV_{3D} (3rd row), and ART+TV_{3D}+MM (4th row) at 56 mAs (left column) and 199 mAs (right column).

It was clear that visual representations of all OOIs of ART+TV_{3D}+MM were better than ART+TV_{3D}, ART, and FBP when we qualitatively evaluated Figure 6.12, proven by smoother background, sharper edges, and better separable objects from the background. Furthermore, when the dose level increased the background noise decreased, and therefore fine details could be better distinguished as expected.

When we zoomed in the OOI-2 for all methods at 56 mAs (lowest dose), 100 mAs (middle dose), and 199 mAs (highest dose), the rectangular frames were distinguishable at all dose levels by ART+TV_{3D}+MM and ART+TV_{3D} whereas it was clearly distinguishable by ART at only the highest dose level (Figure 6.13), which was a clear evidence of how ART+TV_{3D}+MM might attribute to the reduction of the dose level.

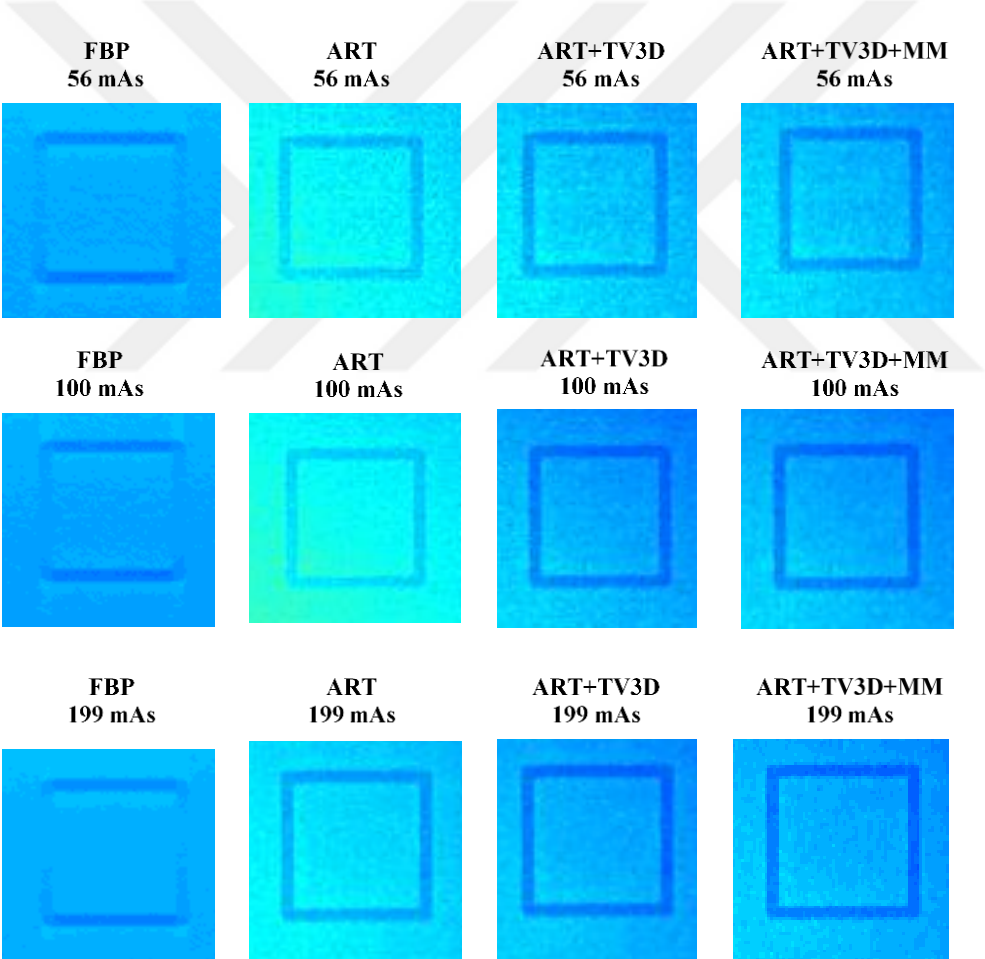


Figure 6.13 : Enlarged views of OOIs-2; FBP (1st column), ART (2nd column), ART+TV_{3D} (3rd column), and ART+TV_{3D}+MM (4th column) at three dose levels in mAs values of (56 (1st row), 100 (2nd row), and 199 (3rd row)).

The same analysis was also performed for OOIs-4 (Figure 6.14). It was observed that FBP reconstructed grids in the circle better than IRT. However, we were able to read clearly the angle degrees 0, 45, 60, and 90 in ART+TV_{3D} and ART+TV_{3D}+MM at dose levels 100 mAs or higher. On the contrary, they were not readable in ART at even the highest dose level, which means that our proposed method ART+TV_{3D}+MM could provide better results than ART at even half dose.

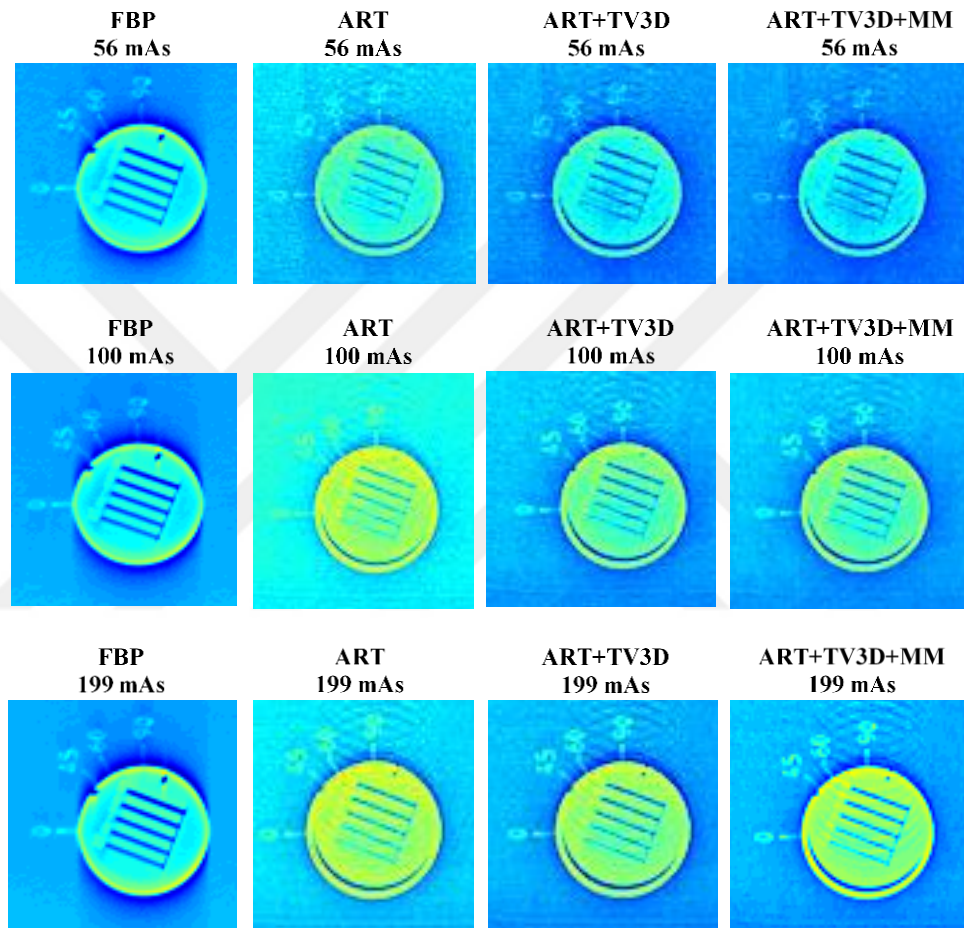


Figure 6.14 : Enlarged views of OOIs-4; FBP (1st column), ART (2nd column), ART+TV_{3D} (3rd column), and ART+TV_{3D}+MM (4th column) at three dose levels in mAs values of (56 (1st row), 100 (2nd row), and 199 (3rd row)).

6.1.2.6 Metric analysis of 12 dose-level-images

We next compared the CNR values of IRT and FBP methods for all dose levels for ROI-1 and ROI-2 in Figure 6.15 and Figure 6.16, respectively. Additionally, 1D profiles-B of the methods for doses at 56 mAs, 100 mAs, and 199 mAs were compared.

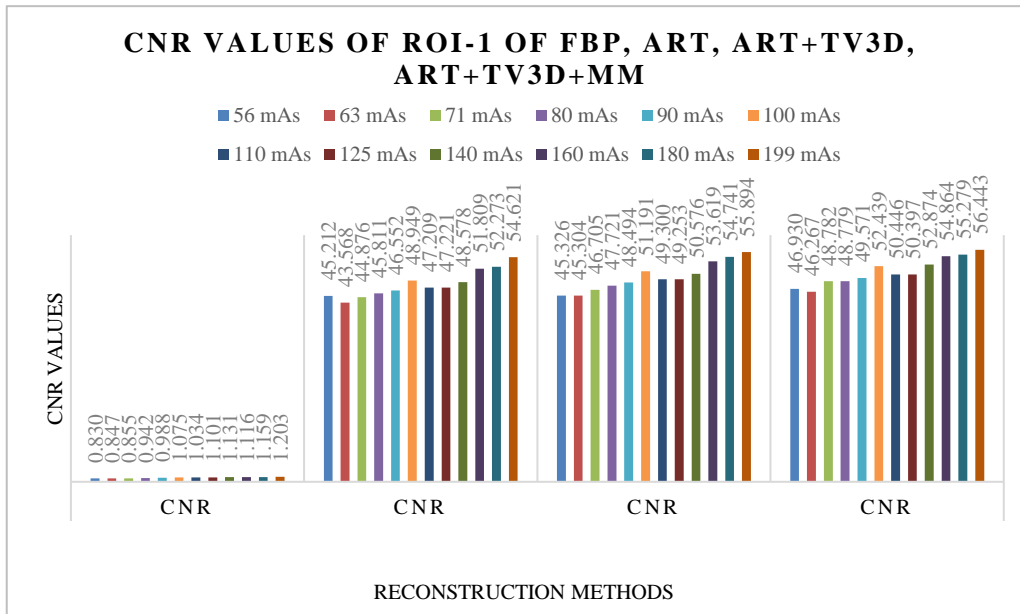


Figure 6.15 : CNR values of ROI-1 of FBP, ART, ART+TV_{3D}, and ART+TV_{3D}+MM at 12 dose levels.

From the CNR values in Figure 6.15, It could be seen that ART, ART+TV_{3D}, and our proposed method ART+TV_{3D}+MM had approximately 45-55 times better results when compared to FBP with ROI-1 evaluating with the CNR. On the other hand, analyzing ROI-2 using the CNR values (Figure 6.16) produced results that were too close to each other to meaningfully draw conclusions; however, visual inspection suggested that ART+TV_{3D}+MM provided the best reconstructed images (see Figure 6.13).

In addition, as the CNR values of ROI-1 of ART+TV_{3D} and ART+TV_{3D}+MM supported very strongly, the image quality of our proposed method was much better than FBP when analyzed qualitatively. For instance, while the CNR value of ROI-1 of FBP at 100 mAs was 1.075, the CNR value of ROI-1 of ART+TV_{3D}+MM at 100 mAs was 52.439, which means 48.78 times better.

At all doses, ART+TV_{3D}+MM showed better results than ART+TV_{3D}, ART+TV_{3D} showed better result than ART, and ART showed better result than FBP in general trend except at 56 mAs and 100 mAs for both ROIs in terms of giving higher CNR values. The reason of why ART results were higher than other three methods at 56 mAs and 100 mAs might be because of shining effect during the acquisition. Additionally, when the dose increased, the values of CNR increased for IRT and FBP. For example, at 63 mAs, 110 mAs, and at 199 mAs the CNR values of

ART+TV_{3D}+MM for ROI-2 were 1.610, 2.053, and 2.473, respectively. The CNR values of FBP for ROI-2 at the same doses were 1.356, 1.822, and 2.188, respectively. As a result, ART+TV_{3D}+MM tended to have the best image quality.

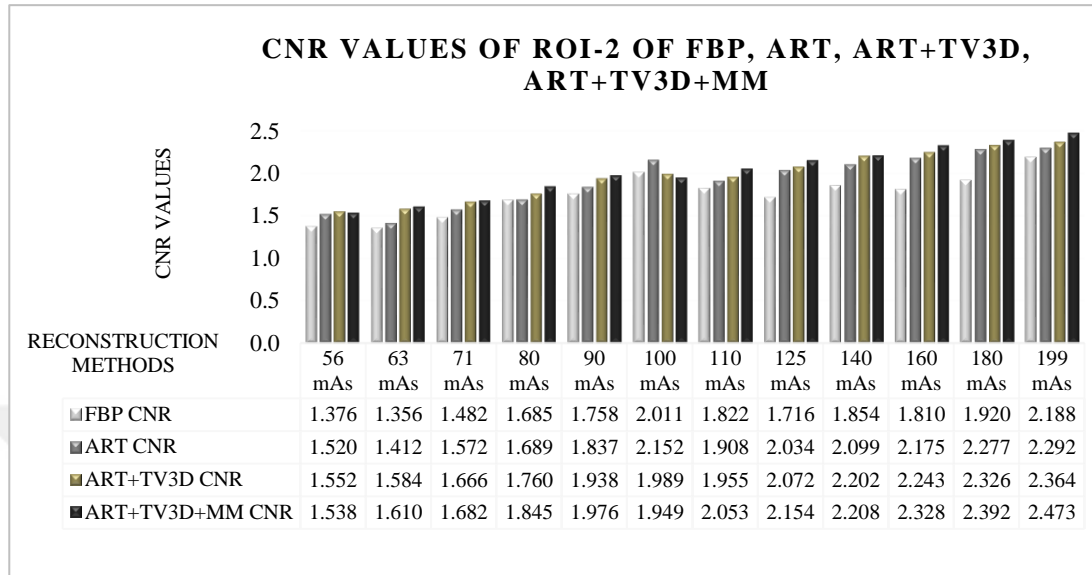


Figure 6.16 : CNR values of ROI-2 of FBP, ART, ART+TV_{3D}, and ART+TV_{3D}+MM at 12 dose levels.

To analyze how 1D profile-B in the OOI-3 shown in Figure 6.5 was effected by the level of dose for the reconstruction methods, we studied the lowest (56 mAs), highest (199 mAs), and middle (100 mAs) dose levels.

For 1D profile-B comparison of IRT and FBP at 12 doses, we preferred and presented the plots of 1D profile-B at 56 mAs, 100 mAs, and 199 mAs dose levels. 1D profiles-B of ART and ART+TV_{3D} methods are given in Figure 6.17 and 1D profiles-B of FBP and ART+TV_{3D}+MM methods are given in Figure 6.18. It was clear that ART+TV_{3D}+MM showed the best performance in terms of amplitudes indicating distinguishability of one circle and four squares in the reconstructed images.

From Figure 6.17, it was clear that as the dose increased the amplitude of the 1D profile-B increased for both methods. In addition, the amplitude of the 1D profile-B generated by ART+TV_{3D} at the lowest dose level even exceeded the one generated by ART at the highest dose level, which was a sign of how ART+TV_{3D} could be used to lower the dose level in DBT imaging.

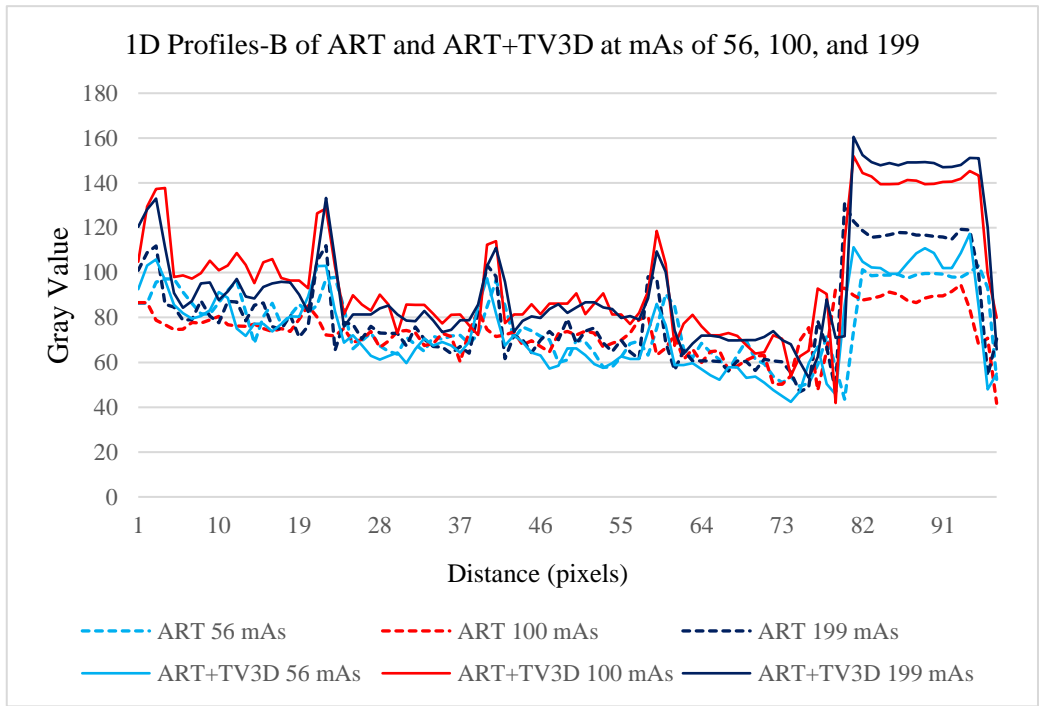


Figure 6.17 : 1D profiles-B at three dose levels for ART (dash) and ART+TV_{3D} (solid); highest dose-199 mAs (dark blue), lowest dose-56 mAs (light blue), and middle dose-100 mAs (red).

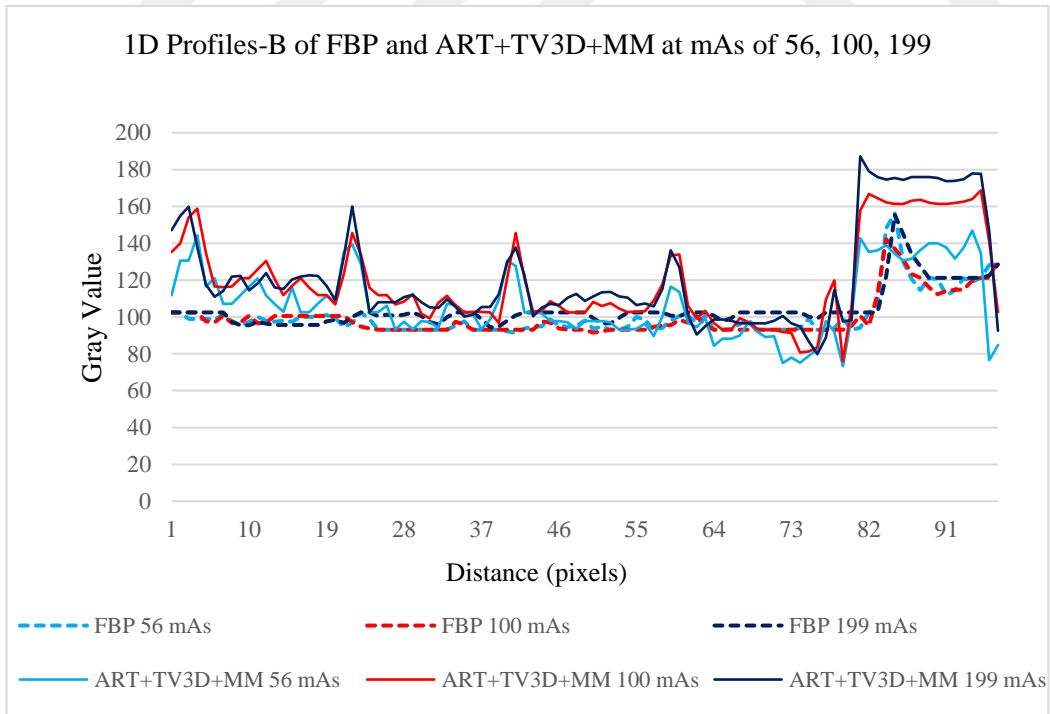


Figure 6.18 : 1D profiles-B at three dose levels for FBP (dash) and ART+TV_{3D}+MM (solid); highest dose-199 mAs (dark blue), lowest dose-56 mAs (light blue), and middle dose-100 mAs (red).

6.2 Results and Discussion for Micro-Bioimaging (MBI)

6.2.1 Reconstruction by manual scanning 3D bioimaging tool

In this section, we presented the reconstructed images of a biological phantom manufactured by PDMS. The projections of the PDMS phantom were acquired via manual scanning 3D bioimaging tool. The dimensions of the PDMS phantom and of its projection in xy -directions were 2cmx2cm and 200x200 pixels, respectively. The resolution of each pixel was 100 $\mu\text{m}/\text{pixel}$. The reference projection is illustrated in Figure 6.19. The regions colored by red and yellow were the anomalies detected from the different layers of the phantom. The diameter and the height of the cylindrical phantom were approximately 2 cm and 2.8 cm respectively (see Figure 6.20).

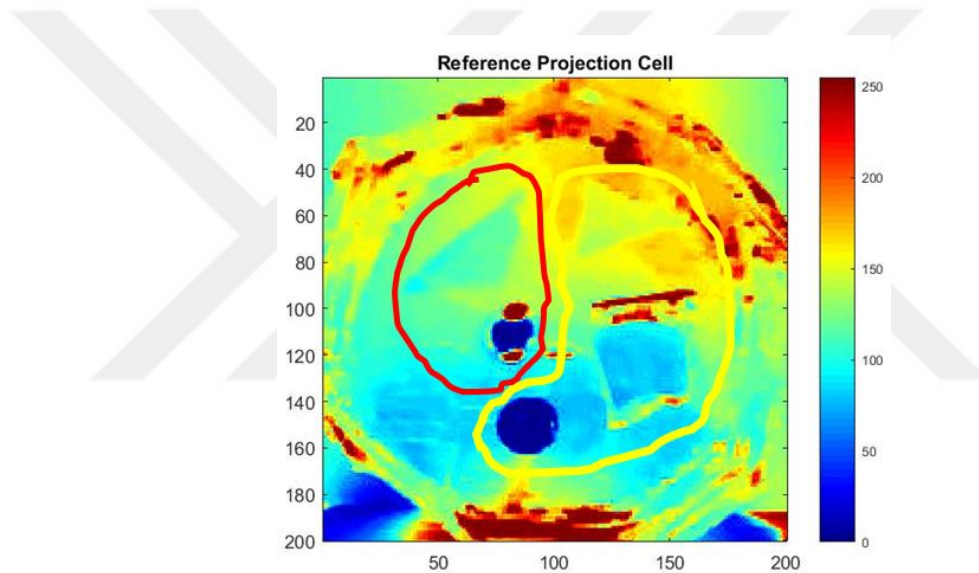


Figure 6.19 : Reference projection of the PDMS phantom.

11 projections were acquired between -25° and $+25^\circ$ with 5° angle step and reconstructed as 50 layers. The dimensions of the reconstructed 3D image were 200x200x50. The layers including the masses were chosen as layers of interest (LOIs). Layer-3 and layer-38 were matched with the real positions in the phantom and demonstrated in Figure 6.20. The matching of reconstruction image and real phantom for layer-3 was signed by red color, whereas for layer-38 was signed by yellow color. It could be seen by these results that we could be able to distinguish the structures and morphology of different layers of a biological structure by the manual scanning 3D bioimaging tool.

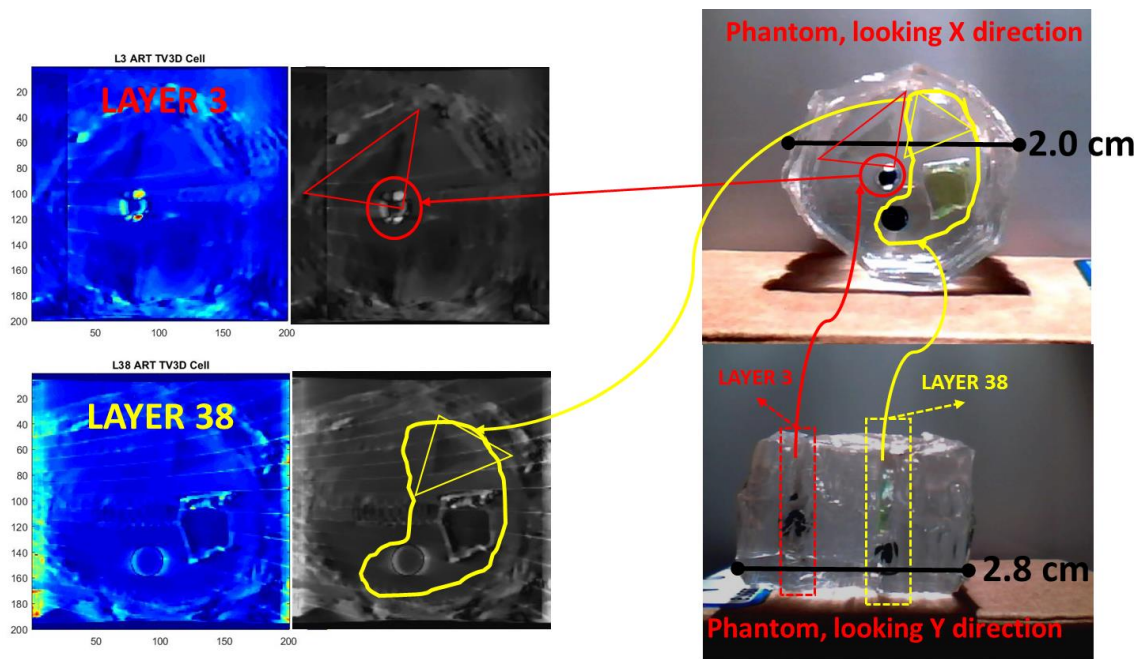


Figure 6.20 : Phantom looking from two different directions. Layer-3 and layer-38 of reconstructed images of the PDMS phantom.

6.2.2 Reconstruction by robotic 3D micro-bioimaging (MBI) tool

The reference projection of the phantom which was acquired via the robotic 3D micro-bioimaging (MBI) tool is illustrated in Figure 6.21. The projection on the left was acquired via CMOS with a mounted lens and ambient light; however, the projection on the right was acquired via CMOS with a separate lens and a light source (the optical imaging design), which was illustrated in Figure 5.5.

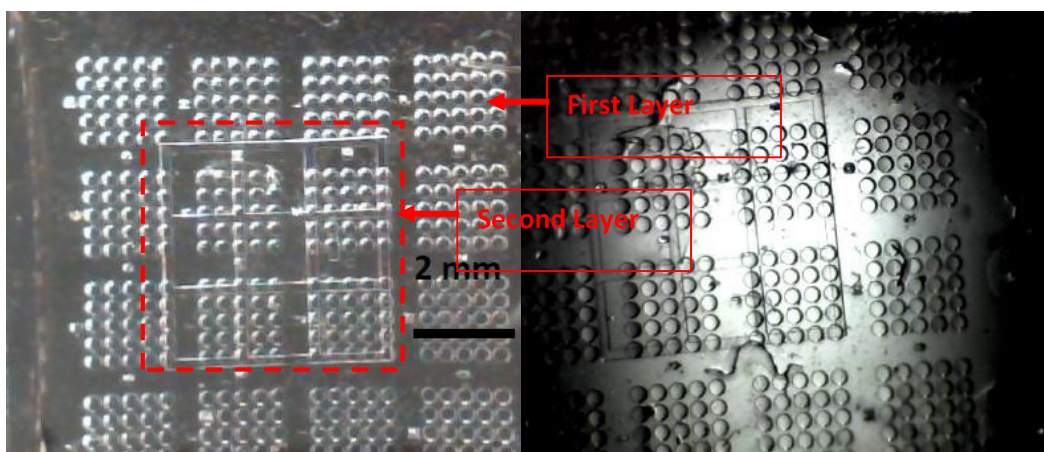


Figure 6.21 : A biological phantom consisting of two different layers. Left: acquisition via CMOS with a mounted lens and ambient light; right: acquisition via CMOS with a separate lens and a light source.

In Figure 6.21, the phantom had 6mmx6mmx1mm-dimensions; second layer included 3x3 squares-grid with 5mmx5mmx0.5mm size and first layer included wells with 300 μm diameter and 100 μm distance between two wells. The length of one edge of the area located each 25 wells (5x5) was 2 mm.

Like the previous experiment, 11 projections were acquired between -25° and $+25^\circ$ with 5° angle step and reconstructed as 50 layers. The dimensions of the reconstructed 3D image were 200x200x50. The resolution of each pixel was 25 $\mu\text{m}/\text{pixel}$. Layers 22 and 34 of the reconstructed images are illustrated in Figure 6.22. 3D models of reconstructed images are shown in Figure 6.23. It could be seen by these results that we could be able to distinguish the structures and morphology of different layers of a biological structure by the robotic 3D MBI tool.

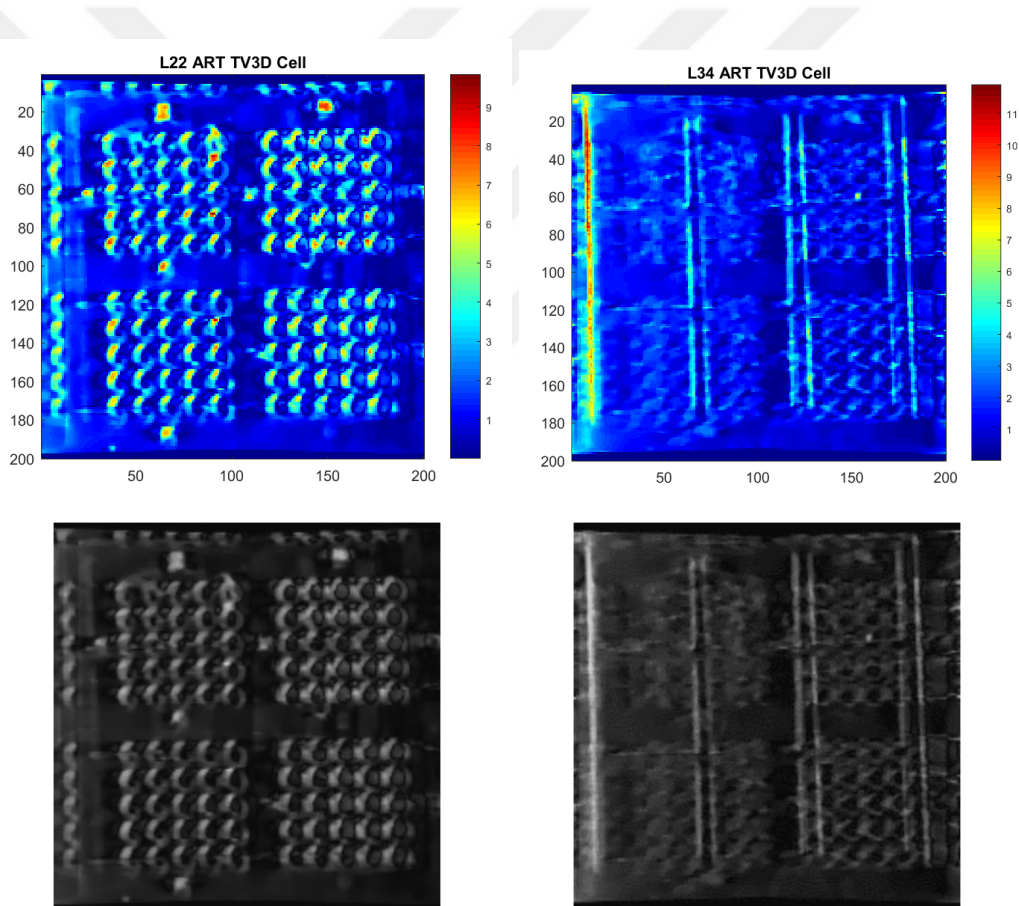


Figure 6.22 : Layer 22 (left column) and Layer 34 (right column) of the reconstructed images of the biological phantom. Figures in the first row are the results of Matlab, in the second row are the results of ImageJ.

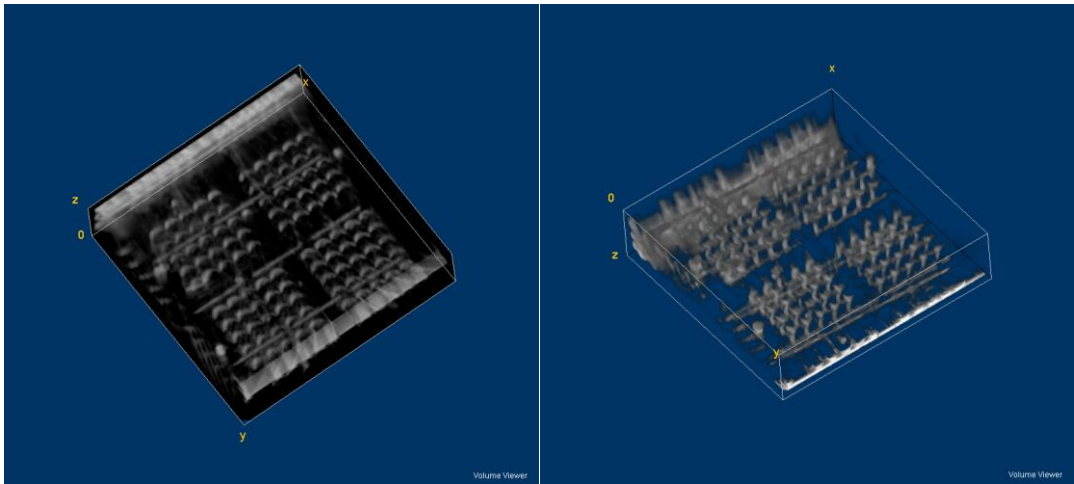


Figure 6.23: 3D models of the reconstructed images of the biological phantom.



7. CONCLUSION

In the literature of digital breast tomosynthesis (DBT) image reconstruction, iterative reconstruction techniques (IRTs) such as algebraic reconstruction technique (ART) and analytical methods such as FBP (filtered back projection) are applied to obtain the reconstructed 3D images of the breast. A compressed sensing based application, TV_{3D} (3-dimensional total variation), is applied to ART to enhance the quality of the reconstructed image.

In this thesis, we mainly studied two major projects. First, we proposed an iterative image reconstruction that is majorization-minimization (MM) based on 3D total variation (TV_{3D}), ($ART+TV_{3D}+MM$) as a novel application in digital breast tomosynthesis (DBT) imaging, and compared its performance with ART and $ART+TV_{3D}$ for an analytical phantom using structural similarity (SSIM) and signal to noise ratio (SNR) metrics. While the value of SSIM of $ART+TV_{3D}+MM$ reached to 0.9814 at the end of the 10th iteration, SSIM values of $ART+TV_{3D}$ and ART were 0.9771 and 0.9208, respectively. Additionally, SNR (dB) values of $ART+TV_{3D}+MM$, $ART+TV_{3D}$, and ART were 24.56, 24.32, and 22.48, respectively. ART performed the poorest results for both metrics. In conclusion, the proposed method $ART+TV_{3D}+MM$ helped to obtain superior results in terms of SNR and SSIM values compared to $ART+TV_{3D}$ and ART.

The radiation dose level applied to patient is one of the most critical limitations of DBT imaging. For this purpose, we further investigated, if a compressed sensing based iterative image reconstruction, MM based 3D TV regularized ART ($ART+TV_{3D}+MM$), could help decrease the radiation dose of patient comparing to MAMMOMAT's FBP using a real breast phantom (CD Pasmam 1054) at 12 different dose levels ranging from 56 to 199 mAs. Moreover, to compare $ART+TV_{3D}+MM$, $ART+TV_{3D}$, ART, and FBP, the analysis of visual inspection for qualitative assessment and CNR values for quantitative assessment were studied by focusing on objects of interest (OOIs) and regions of interest (ROIs). When the dose increased, the values of CNR increased for all methods as expected. Additionally, the CNR values of $ART+TV_{3D}+MM$ were the highest and the CNR values of $ART+TV_{3D}$ were higher

than the CNR values of ART and FBP in general trend. For example, at 71 mAs, at 140 mAs, and at 199 mAs, while the CNR values of ART for ROI-2 were 1.572, 2.099, and 2.292, the CNR values of ART+TV_{3D} for ROI-2 were 1.666, 2.202, and 2.364, and the CNR values of ART+TV_{3D}+MM for ROI-2 were 1.682, 2.208, and 2.473, respectively. The results showed that compressed sensing based image reconstruction techniques (ART+TV_{3D} and ART+TV_{3D}+MM) could efficiently decrease the radiation dose level by providing better reconstructed images in terms of obtaining fine details and generating higher CNR values.

The second project was to adapt the software algorithms for 3D image reconstruction and to create a robotic scanning tool for 3D imaging system in micro-bioimaging (MBI). For this purpose, we created the robotic 3D MBI tool, which was comprised of two main parts: hardware (mechanical, electronics, and optical) and software (robotic scanning control software and 3D bioimaging reconstruction software). To test the ability of the acquisition of the projections and reconstructing these projections via ART+TV_{3D} reconstruction algorithm of the robotic 3D MBI tool, we manufactured a few biological phantoms. The tool could be able to acquire the projections between -45° and +45° with 5° angle step, which means 19 projections.

We proved that the robotic 3D MBI tool we created could reconstruct 3D images of various biological samples slice by slice, which means the layers of a biological sample such as a PDMS phantom that mimics a cancerous tumor could be distinguished successfully.

8. FUTURE WORKS

The future studies in digital breast tomosynthesis (DBT) will address developing patient specific low dose 3D breast imaging. The ultimate goal of this research in micro-bioimaging (MBI) project by developing advanced robotic 3D micro-bioimaging (MBI) tool will be to investigate how morphology differentiation and proliferation of the tumor is attained by cells after putting in the hydrogel. We will study the changes that happen on a morphological level after the interaction of the tumor tissue with drugs inside a gel as well. The future purpose of this project can be demonstrated in Figure 8. 1.

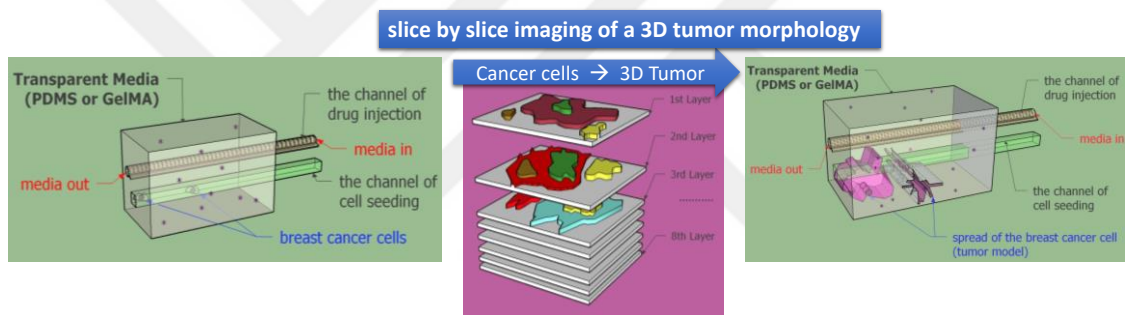


Figure 8.1 : The demonstration of the ultimate goal of the project in MBI.

It is final goal of the advanced robotic 3D MBI tool project that when a user/scientist presses just a button of computer, the robotic 3D MBI tool will scan a biological system such as bioreactor, lab-on-a-chip system, spheroid or tumor to acquire projections, the algorithm will run automatically, and the results will be 3D reconstructed images of the object desired to visualize layer by layer.



REFERENCES

- Ahmed M. N., Yamany S. M., Mohamed N., Farag A. A., & Moriarty T.** (2002). A Modified Fuzzy C-Means Algorithm for Bias Field Estimation and Segmentation of MRI Data. *IEEE Transactions On Medical Imaging*, 21(?), 193-199.
- American Cancer Society (ACS).** (2014). Breast Cancer Prevention and Early Detection, Toll-free number: 1-800-232-4636 (1-800-CDC-INFO), Last Revised: 9/10/2014. Date retrieved 13.01.2015, address: www.cancer.org
- Andersen, A. H.** (1989). Algebraic Reconstruction in CT from Limited Views. *IEEE Transactions on Medical Imaging*, 8(1), 50-55.
- Baker, J. A., & Lo, J. Y.** (2011). Breast tomosynthesis: state-of-the-art and review of the literature. *Academic Radiology*, 18(10), 1298-1310.
- Beister, M., Kolditz, D., & Kalender, W. A.** (2012). Iterative reconstruction methods in X-ray CT. *Physica Medica*, 28(?), 94-108.
- Can, E.** (2011). *Comparison of two different ray tracing algorithms for Tomosynthesis* (Master's thesis). Istanbul Technical University, Istanbul.
- Candes, E. J. & Wakin, M. B.** (2008). An Introduction to Compressive Sampling. *IEEE Signal Processing Magazine*, 1053-5888/08/\$25.00, 21-30.
- Chambolle, A.** (2004). An Algorithm for Total Variation Minimization and Applications. *Journal of Mathematical Imaging and Vision*, 20(?), 89-97.
- Chen G.H., Tang J., & Leng S.** (2008). Prior Image Constrained Compressed Sensing (PICCS): A Method to Accurately Reconstruct Dynamic CT Images from Highly Undersampled Data Sets. *Med. Phys.*, 35(3), 660-663.
- Dale, S, Edholm, P. E., Hellstrom L. G., & Larsson S.** (1980). Ectomography-a tomographic method for gamma camera imaging. *Physics in Medicine & Biology*, 30(11), 1237-1249.
- Digital Breast Tomosynthesis.** (2013): Overview of the evidence and issues for its use in screening for breast cancer.
- Dobbins, J. T.** (2009). Tomosynthesis imaging: At a translational crossroads. *Medical Physics*, 36(6), 1956-1967.
- Dobbins, J. T. III & Godfrey, D.J.** (2003). Digital X-ray tomosynthesis: current state of the art and clinical potential. *Physics in Medicine and Biology*, 48(?), R65-R106.
- Donoho D. L.** (2006). Compressed Sensing, *IEEE Trans. on Inform. Theo.*, 52(4), 1289-1306.

- Duarte, I. C.** (2009). *3D Medical Image Reconstruction on Digital Breast Tomosynthesis* (Master's thesis). Faculty of Sciences and Technology of University of Coimbra.
- Ekstrom, M. P.** (1984). *Digital Image Processing Techniques*. Orlando-Florida, Academic Press, 142-166.
- Eldar Y. C. & Michaeli T.** (2009). Beyond bandlimited sampling. *IEEE Signal Processing Mag.*, 26(3), 48-68.
- Ertas, M.** (2015). *Reduction of out-of-focus slice blur in tomosynthesis images* (Ph.D. Thesis). Istanbul University, Istanbul.
- Ertas, M., Akan, A., Cengiz, K., Kamasak, M., Seyyedi, S., & Yildirim, I.** (2012). 3-D tomosynthesis image reconstruction using total variation. *2012 ASE International Conference on Social Informatics (SocialInformatics 2012) / 2012 ASE International Conference on Cyber Security (CyberSecurity 2012) / 2012 ASE International Conference on BioMedical Computing*.
- Ertas, M, Yildirim, I., Kamasak, M., & Akan, A.** (2013a). Digital breast tomosynthesis image reconstruction using 2D and 3D total variation minimization. *BioMedical Engineering OnLine*, 12(1), 112.
- Ertas, M, Yildirim, I., Kamasak, M., & Akan, A.** (2013b). An iterative tomosynthesis reconstruction using total variation combined with non-local means filtering. *BioMedical Engineering OnLine*, 13(65), 1-13.
- Figueiredo, M., Bioucas-Dias, J., & Nowak R.** (2007). Majorization- Minimization Algorithms for Wavelet-Based Image Restoration. *IEEE Transactions on Image Processing*, 16(12), 2980-2991.
- Garrett, J., Tang, J., Zhang, Y., Ruth, C., Jing, Z., & Chen, G.** (2012). Dose Reduction in Digital Breast Tomosynthesis with the Dose Reduction Prior Image Constrained Compressed Sensing (DR-PICCS) Algorithm. *Medical Physics*, 39(6Part24), 3916.
- Ghallab, Y. & Badawy, W.** (2004). Sensing methods for dielectrophoresis phenomenon: from bulky instruments to lab-on-a-chip. *IEEE Circuits and Systems Magazine*, 4(3), 5-15.
- Gur D., Zuley M. L., Anello M. I., Rathfon G. Y., Chough D. M., Ganott M. A., ... Bandos A. I.** (2012). Dose reduction in digital breast tomosynthesis (DBT) screening using synthetically reconstructed projection images: an observer performance study. *Acad Radiology*, 19(2), 166–171.
- Helvie, M. A.** (2010). Digital mammography imaging: breast tomosynthesis and advanced applications. *Radiol Clin North Am.*, 48(5), 917–929.
- Herman, G. T.** (1980). *Image reconstruction from projections: the fundamentals of computerized tomography*, in: *Computer science and applied mathematics*. Academic Press, San Francisco, p.xiv.316 p.
- Hunter D. & Lange K.** (2004). A Tutorial on MM Algorithms. *The American Statistician*, 58(1), 30-37.
- Kaczmarz, S.** (1937). "Angenäherte Auflösung von Systemen linearer Gleichungen", *Bulletin International de l'Académie Polonaise des Sciences et des*

Lettres. *Classe des Sciences Mathématiques et Naturelles. Série A, Sciences Mathématiques*, 35(?), 355–357.

- Kopans, D. B.** (2014). Digital Breast Tomosynthesis: From Concept to Clinical Care. *AJR Am J Roentgenology*, 202(2), 299-308.
- Lewin, J. M., & Niklason, L.** (2007). Advanced Applications of Digital Mammography: Tomosynthesis and Contrast-Enhanced Digital Mammography. *Seminars in Roentgenology*, 42(4), 243-252.
- National Cancer Institute.** (2014). *Mammograms*. Retrieved from <http://www.cancer.gov/cancertopics/factsheet/detection/mammogram>, retrieval date 15.12.2014.
- Ntalampeki, S.** (2007). *Dynamic computed tomography, an algebraic reconstruction method with deformation compensation* (Master's thesis). University Joseph Fourier, France and University of Crete, Greece.
- Oliveira N., Mota A. M., Matela N., Janeiro L., & Almeida P.** (2016). Dynamic relaxation in algebraic reconstruction technique (ART) for breast tomosynthesis imaging. *Computer Methods and Programs in Biomedicine*, 132(?), 189-196.
- Park, Y., Cho, H., Je, U., Cho, H., Park, C., Lim, H., ... Choi, S.** (2015). Evaluation of the image quality in digital breast tomosynthesis (DBT) employed with a compressed-sensing (CS)-based reconstruction algorithm by using the mammographic accreditation phantom. *Nuclear Instruments and Methods in Physics Research A* 804(?), 72-78.
- Peterson, J. E., Paulsson, B. N. P., & McEvelly, T. V.** (1985). Applications of algebraic reconstruction techniques to crosshole seismic data. *Geophysics*, 50(10), 1566-1580.
- Polat A. & Yildirim I.** (2018). An Iterative Reconstruction Algorithm for Digital Breast Tomosynthesis Imaging Using Real Data at Three Radiation Doses. *Journal of X-Ray Science and Technology*, doi: 10.3233/XST-17320 (Accepted on December 24, 2017).
- Polat A., Matela N., Mota A. M., & Yildirim I.** (2016). Implementation of Majorization-Minimization (MM) Algorithm for 3D Total Variation Minimization in DBT Image Reconstruction. *IEEE Nuclear Science Symposium & Medical Imaging Conference* October 29 – November 06, 2016 Strasbourg. *This work has been supported in part by TUBITAK, The Scientific and Research Council of Turkey, under the grant 111E086 and Fundação para a Ciência e a Tecnologia - Portugal (Project Pest-OE/SAU/IU0645/2013).*
- Rudin, L.I., Osher S., & Fatemi E.** (1992). Nonlinear total variation based noise removal algorithms. *Physica D*, 60(?), 259-268. North-Holland.
- Selesnick, I.** (2014). Total Variation Denoising (MM Algorithm), Eeweb.poly.edu, 2014. [Online]. Retrieved from http://eeweb.poly.edu/iselesni/lecture_notes/TVDmm. [retrieval date: April 2016].
- Sener, N.** (2013). *Tomosentez görüntüleme de Siddon algoritması kullanılarak ART ve SART yöntemlerinin karşılaştırılması* (Master's thesis). Istanbul Technical University, Istanbul.

- Siddon, R. L.** (1985). Fast calculation of the exact radiological path for a three-dimensional CT array. *Medical Physics*, 12(2), 252-255.
- Sidky E. Y., Reiser I., Nishikawa R. W., Pana X., Chartrand C., Kopans D. B. & Moore R. H.** (2008). Practical iterative image reconstruction in digital breast tomosynthesis by non-convex TpV optimization. *Proc SPIE*, 6913(?), 6913-6928.
- Siemens AG.** (2016). "MAMMOMAT Inspiration-Tomosynthesis Option", Vol. January 2016 Retrieved from http://www.accessdata.fda.gov/cdrh_docs/pdf14/P140011c.pdf. [retrieval date: January 2016].
- Siemens MAMMOMAT Inspiration.** (2017). Retrieved from <http://www.delta-medicalsystems.com/DeltaMedicalSystems/media/ProductDetails/TomoData-Sheet.pdf> [retrieval date: November 2017].
- Smith, A.** (2012). Fundamentals of Breast Tomosynthesis. 78967-12_WP-00007 *Fundmntls- Tomo*.
- Southern Scientific Ltd**, "CD PASMAM 1054 Datasheet ".
- Sree, S. V., Yin-Kwee, E. N., Acharya, R. U., & Faust, O.** (2011). Breast imaging: A survey. *World J Clin Oncol*, 2(65), 171-178.
- Stein, J., Smith, A. P., Jing, Z., & Ni, L.** (2014). US Patent No. 20140044230 A1.
- Svahna, T. M., Houssamia N., Sechopoulos I., & Mattsone S.** (2015). Review of radiation dose estimates in digital breast tomosynthesis relative to those in two-view full-field digital mammography. *Breast*, 24(2), 93–99.
- Tessa, V. H., Sarah, W., Maggie, G., Joost, B. K., & Jan, S.** (2004). The implementation of iterative reconstruction algorithms in MATLAB. Universiteit Antwerpen.
- Tingberg, A., Förnvik, D., Mattsson, S., Svahn, T., Timberg, T., & Zackrisson, S.** (2011). Breast cancer screening with tomosynthesis: initial experiences. *Radiation Protection Dosimetry*, 147(1-2), 180-183.
- Tropp J. & Wright S.** (2010). Computational methods for sparse solution of linear inverse problems, *Proc. IEEE*, 98(6), 948-958.
- Turbell, H.** (2001). *Cone-beam reconstruction using filtered backprojection* (Ph.D. thesis). Linköpings University, Institute of Technology, Linköping, Sweden.
- Url-1** <<http://yale.edu/imaging/contents.html>>, date retrieved 22.06.2015.
- Url-2** <<http://www.imaginis.com/ct-scan/brief-history-of-ct>>, date retrieved 20.12.2014.
- Url-3** <<http://www.fda.gov/RadiationEmittingProducts/RadiationEmittingProductsand/Procedures/MedicalImaging/MedicalXRays/ucm115317.htm#1>>, date retrieved 20.12.2014.
- Url-4** <http://en.wikipedia.org/wiki/X-ray_computed_tomography#cite_note-ref1>, date retrieved 20.12.2014.
- Url-5** <http://en.wikipedia.org/wiki/Mammography#cite_note-15>, date retrieved 15.12.2014.

- Url-6** <<http://www.radiologyinfo.org/en/info.cfm?pg=mammo>>, date retrieved 12.12.2014.
- Url-7** <http://en.wikipedia.org/wiki/File:Tomographic_fig1.png>, date retrieved 25.12.2014.
- Url-8** <http://me.bilkent.edu.tr/?page_id=1045&nvaf_id=9>, date retrieved 06.06.2017.
- Url-9** <<https://www.edmundoptics.com/optics/optical-lenses/achromatic-lenses/10mm-dia.-x-30mm-fl-vis-nir-coated-achromatic-lens/>>, date retrieved 29.06.2017
- Url-10** <http://cab.ku.dk/what_is_bioimaging/>, date retrieved 12.10.2017
- Url-11** <<http://www.bioimaging.biostec.org/>>, date retrieved 12.10.2017
- Veldkamp, W. G., Kraft, L. J., & Jacob, G. E.** (2009). Dose and perceived image quality in chest radiography. *European Journal of Radiology*, 72(2), 209-217.
- Volpatti, L. R. & Yetisen, A. K.** (2014). Commercialization of microfluidic devices. *Trends in Biotechnology*, 32(7), 347–350.
- Wang, Z.** (2016). [Online]. Available: <https://ece.uwaterloo.ca/~z70wang/research/ssim/>, retrieval date 12- Apr- 2016.
- Wang Z., Bovik A., Sheikh H. & Simoncelli, E.** (2004). Image Quality Assessment: From Error Visibility to Structural Similarity. *IEEE Transactions on Image Processing*, 13(4), 600-612.
- Wu, G., Mainprize, J. G., & Yaffe, M. J.** (2012). Dose reduction for digital breast tomosynthesis by patch-based denoising in reconstruction. *IWDM'12 Proceedings of the 11th international conference on Breast Imaging*, (pp. 721-728). Springer-Verlag Berlin, Heidelberg.
- Wu T., Moore R. H., Rafferty E. A., & Kopans D. B.** (2004). A comparison of reconstruction algorithms for breast tomosynthesis. *Med. Phys.*, 31(?), 2636-2647.
- Yıldırım, I. (Project Coordinator), & Kamasak, M. (Researcher).** (2014). Tomosentez Görüntülerinde Odak Dışı Dilim Bulanıklığının Giderilmesi. *TUBITAK, Program Code.1001, Project No.111E086*, Istanbul.
- Yildirim I., Ansari R., Wanek J., Yetik I. S., & Shahidi M.** (2009). Regularized Estimation of Retinal Vascular Oxygen Tension From Phosphorescence Images. *IEEE transactions on bio-medical engineering*, 56(8), 1989–1995.
- Zhao, B. & Zhao W.** (2008). Imaging performance of an amorphous selenium digital mammography detector in a breast tomosynthesis system. *Medical Physics*, 35(5), 1978-1987.



APPENDICES

APPENDIX A : FBP, ART, ART+TV_{3D}, and ART+TV_{3D}+MM at 12 doses.





APPENDIX A

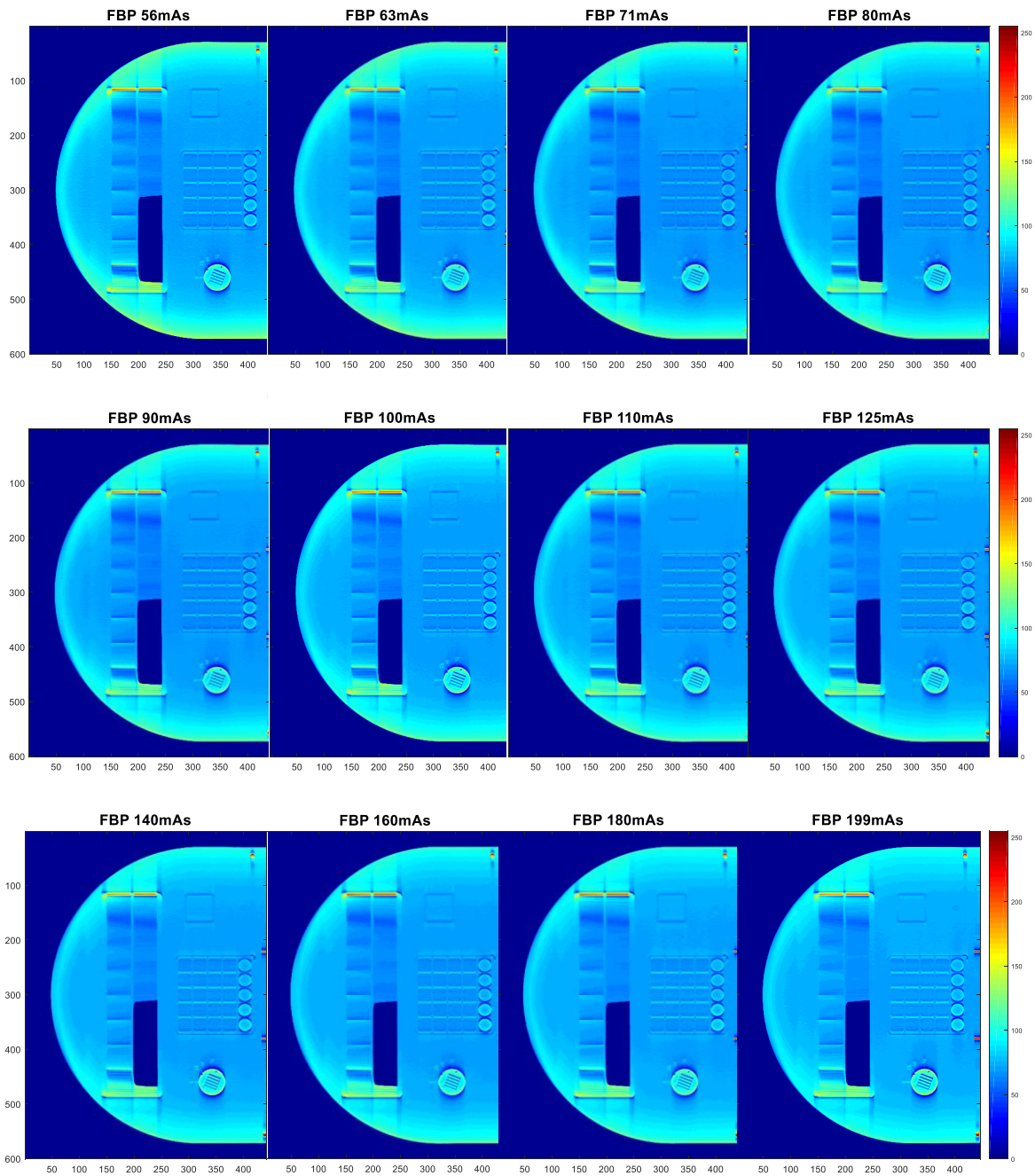


Figure A.1 : FBP at 12 doses.

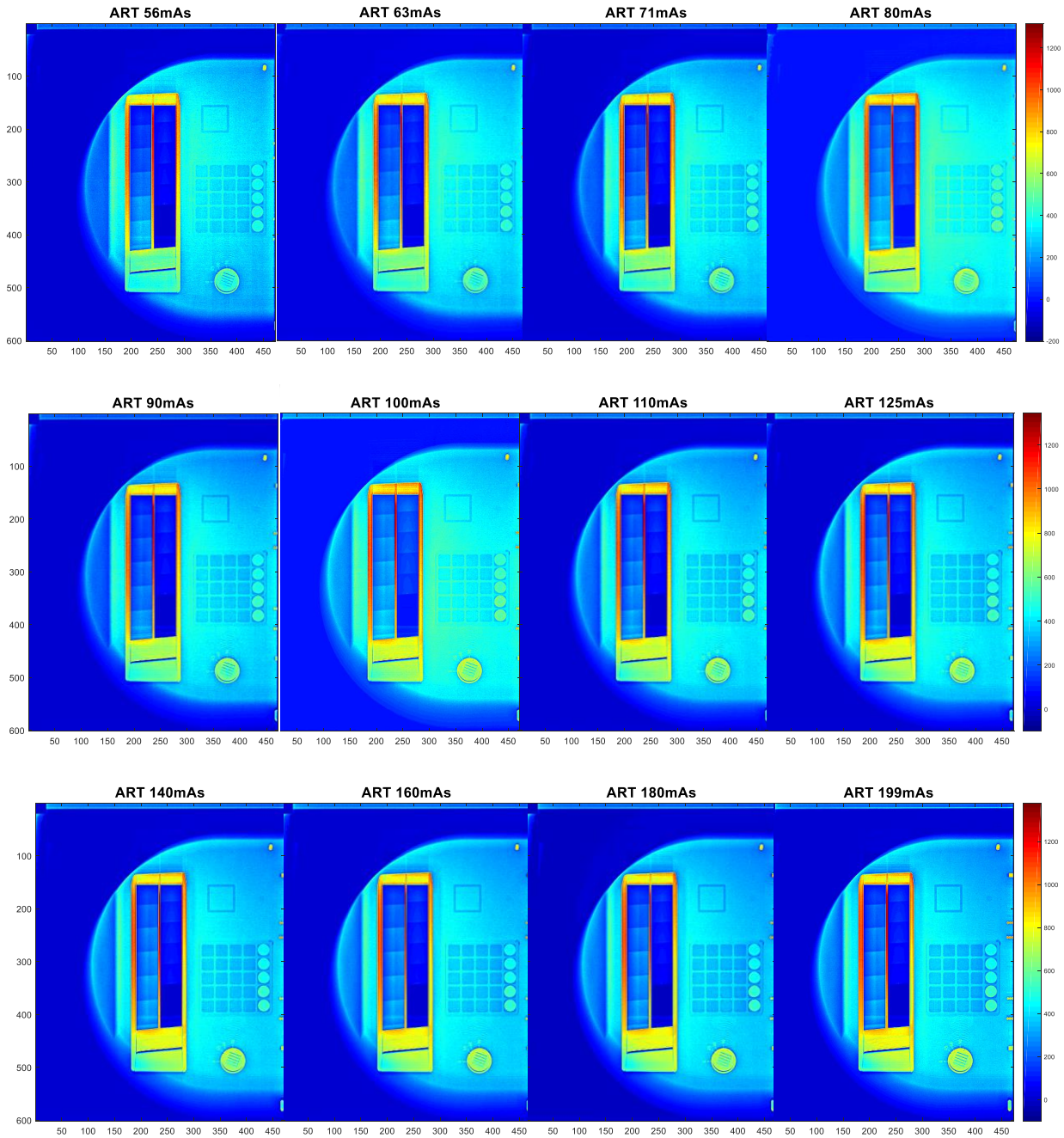


Figure A.2 : ART at 12 doses.

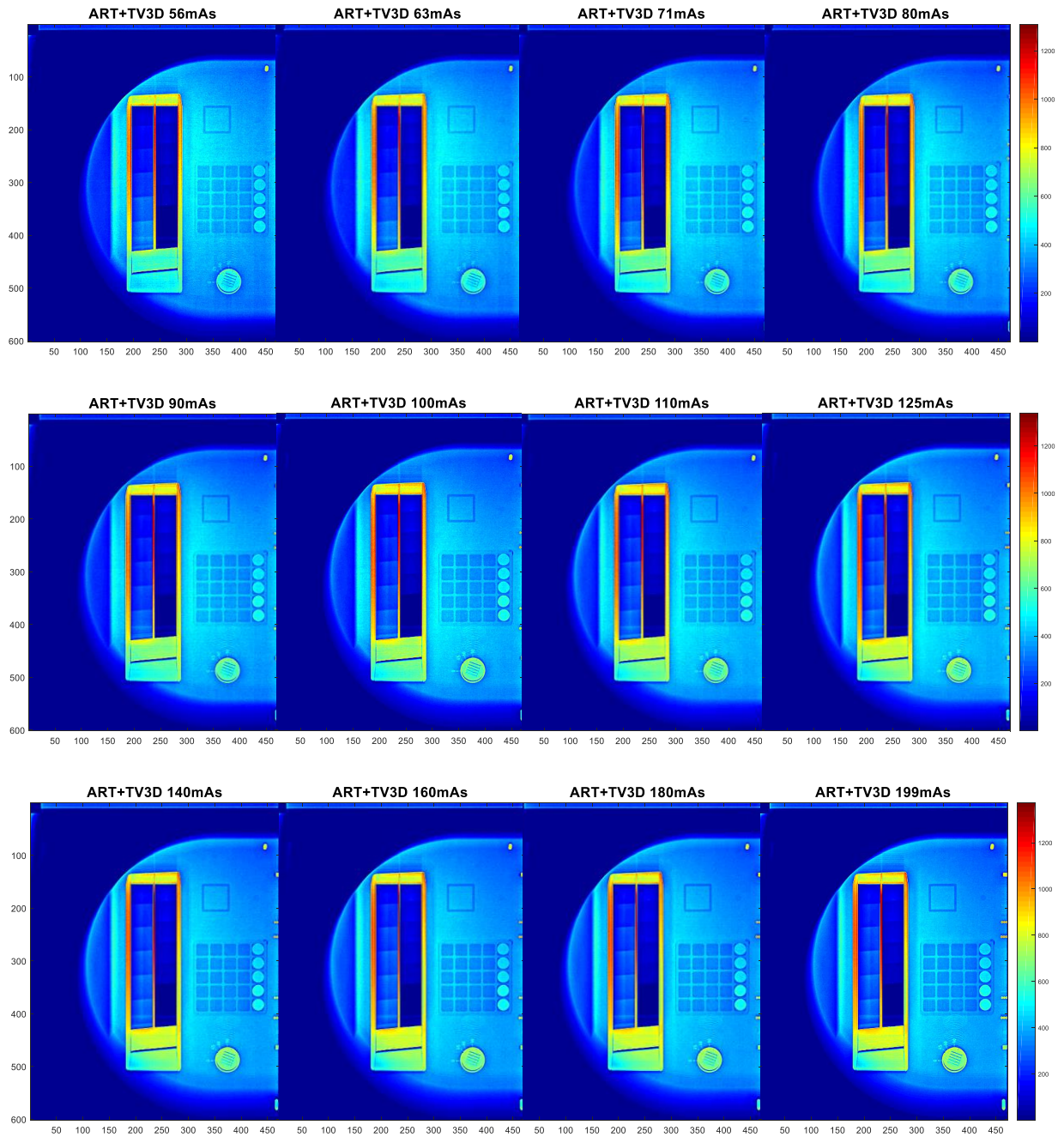


Figure A.3 : ART+TV_{3D} at 12 doses.

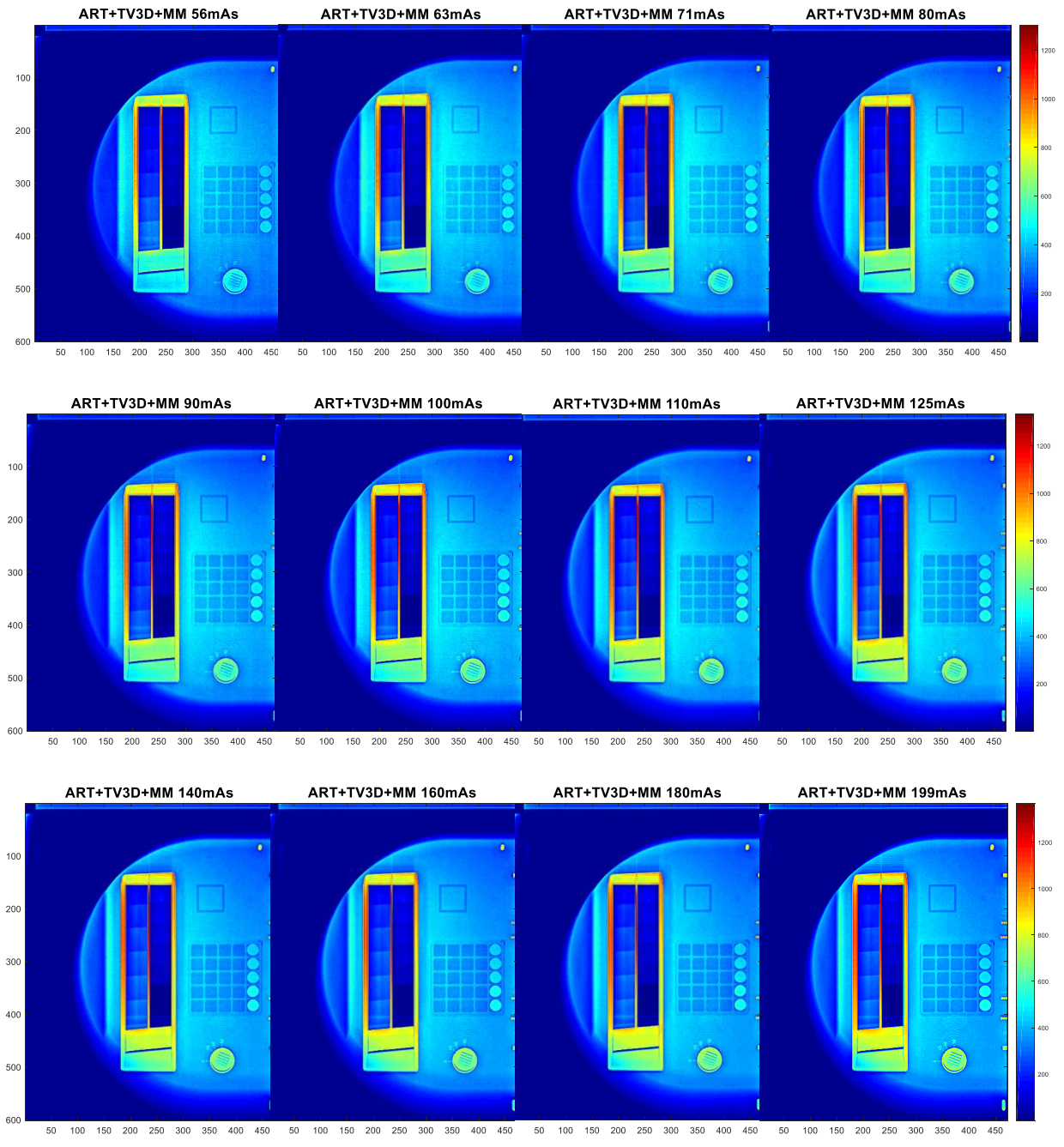


Figure A.4 : ART+TV_{3D}+MM at 12 doses.

Table A.1 : The types of iterative reconstruction techniques (Beister et al., 2012).

Abbreviation	Meaning	Reference
ART	Algebraic Reconstruction Technique	Gordon R, Bender R, Herman GT. Algebraic reconstruction techniques (ART) for three-dimensional electron microscopy and X-ray photography. <i>J Theor Biol</i> 1970; 29:471-482.
SART	Simultaneous ART	Andersen AH, Kak AC. Simultaneous algebraic reconstruction technique (SART): a superior implementation of the ART algorithm. <i>Ultrason Imaging</i> 1984; 6:81-94.
SIRT	Simultaneous Iterative Reconstruction Technique	Gilbert P. Iterative methods for the three-dimensional reconstruction of an object from projections. <i>Jl Theor Biol</i> 1972; 36:105-117.
MART	Multiplicative Algebraic Reconstruction Technique	Gordon R, Bender R, Herman GT. Algebraic reconstruction techniques (ART) for three-dimensional electron microscopy and X-ray photography. <i>J Theor Biol</i> 1970; 29:471-482. Lent A, Censor Y. The primal-dual algorithm as a constraintset-manipulation device. <i>Math Programming</i> 1991; 50:343-357. Badea C, Gordon R. Experiments with the nonlinear and chaotic behavior of the multiplicative algebraic reconstruction technique (MART) algorithm for computed tomography. <i>Phys Med Biol</i> 2004; 49:1455-1474.
OS-SIRT	Ordered Subset SIRT	Gilbert P. Iterative methods for the three-dimensional reconstruction of an object from projections. <i>Jl Theor Biol</i> 1972; 36:105-117. Xu F, Xu W, Jones M, Keszthelyi B, Sedat J, Agard D, et al. On the efficiency of iterative ordered subset reconstruction algorithms for acceleration on GPUs. <i>Comput Methods Programs Biomed</i> 2010; 98:261-270.
ML-EM	Maximum Likelihood Expectation Maximization	Lange K, Carson R. EM reconstruction algorithms for emission and transmission tomography. <i>J Comput Assist Tomogr</i> 1984; 8:306-316.
OS-EM	Ordered Subset Expectation Maximization	Manglos SH, Gagne GM, Krol A, Thomas FD, Narayanaswamy R. Transmission maximum-likelihood reconstruction with ordered subsets for cone beam CT. <i>Phys Med Biol</i> 1995;40:1225-1241.

Table A.1 (continued) : The types of iterative reconstruction techniques (Beister et al., 2012).

Abbreviation	Meaning	Reference
OSC	Ordered Subset Convex Algorithm	Kamphuis C, Beekman FJ. Accelerated iterative transmission CT reconstruction using an ordered subsets convex algorithm. <i>IEEE Trans Med Imaging</i> 1998; 17:1101-1105. Erdogan H, Fessler JA. Ordered subsets algorithms for transmission tomography. <i>Phys Med Biol</i> 1999; 44:2835-2851. Beekman FJ, Kamphuis C. Ordered subset reconstruction for X-ray CT. <i>Phys Med Biol</i> 2001; 46:1835-1844.
ICD	Iterative Coordinate Descent	Sauer K, Bouman C. A local update strategy for iterative reconstruction from projections. <i>IEEE Trans Sig Proc</i> 1993; 41(2):534-548. Bouman C, Sauer K. A unified approach to statistical tomography using coordinate descent optimization. <i>IEEE Trans Image Process</i> 1996; 5:480-492. Thibault J-B, Sauer KD, Bouman CA, Hsieh JA. Three-dimensional statistical approach to improved image quality for multislice helical CT. <i>Med Phys</i> 2007; 34:4526-4544.
OS-ICD	Ordered Subset ICD	Lee S-J. Accelerated coordinate descent methods for Bayesian reconstruction using ordered subsets of projection data. <i>Proc SPIE Conf Math Model</i> ; 2000. 4121, pp. 170-181. Zhu H, Shu H, Zhou J, Luo L. A weighted least squares PET image reconstruction method using iterative coordinate descent algorithms. <i>Proc. IEEE Nuclear Science Symp Conf Record</i> ; 2004. 6, pp. 3380-3384.
MBIR	Model-Based Iterative Reconstruction	Thibault J-B, Sauer KD, Bouman CA, Hsieh JA. Three-dimensional statistical approach to improved image quality for multislice helical CT. <i>Med Phys</i> 2007; 34:4526-4544. Yu Z, Thibault J-B, Bouman CA, Sauer KD, Hsieh J. Fast modelbased X-ray CT reconstruction using spatially nonhomogeneous ICD optimization. <i>IEEE Trans Image Process</i> 2011; 20:161-175.

CURRICULUM VITAE



Name Surname: Adem Polat

Place and Date of Birth: Maden 20.03.1978

E-Mail: apolat@mit.edu; polatadem1773@gmail.com;
polatadem@itu.edu.tr

EDUCATION: Ph.D.

B.Sc.: ITU Electronics and Communication Engineering

M.Sc.: ITU Satellite Communication and Remote Sensing

Ph.D.: ITU Satellite Communication and Remote Sensing

PROFESSIONAL EXPERIENCE AND REWARDS:

- **2016 IEEE NSS-MIC Trainee Grant**
IEEE Nuclear Science Symposium & Medical Imaging Conference
October 29 – November 06, 2016 Strasbourg, France
- **TUBITAK 2214-International Research Fellowship Program (for PhD Students) 2016/1**
Application Number: 1059B141600590
Harvard Medical School, Harvard-MIT Health Science and Technology
December 30, 2016 – December 30, 2017
- **ITU Support for PhD Projects of Scientific Research**
Project Number: 39806
- **ITU UHeM (The National Center for High Performance Computing) Support for PhD Projects of Scientific Research**
Project/Grant Number: 4004222016

PUBLICATIONS, PRESENTATIONS AND PATENTS ON THE THESIS:

- **Polat A., and Yildirim I., 2018: An Iterative Reconstruction Algorithm for Digital Breast Tomosynthesis Imaging Using Real Data at Three Radiation Doses. *Journal of X-Ray Science and Technology* (Accepted 24 December 2017, DOI 10.3233 / XST-17320).**

- **Polat A.**, Matela N., Mota A. M., Zhang Y. S., and Yildirim I., 2018: Digital Breast Tomosynthesis Imaging Using Compressed Sensing Based Reconstruction for 10 Radiation Doses Real Data. *Biomedical Signal Processing and Control* (In review).
- **Polat A.**, Matela N., Mota A. M., and Yildirim I., 2016: Implementation of Majorization-Minimization (MM) Algorithm for 3D Total Variation Minimization in DBT Image Reconstruction. *IEEE Nuclear Science Symposium & Medical Imaging Conference* October 29 – November 06, 2016 Strasbourg. **DOI: 10.1109/NSSMIC.2016.8069493**

This work has been supported in part by TUBITAK, The Scientific and Research Council of Turkey, under the grant 111E086 and Fundação para a Ciência e a Tecnologia - Portugal (Project Pest-OE/SAU/IU0645/2013).

OTHER PUBLICATIONS, PRESENTATIONS AND PATENTS:

- **Polat A.**, and Örmeci C., 2015: The Mapping of Hydrocarbon Seepages by Using Landsat TM Satellite Images: Adiyaman Case Study. 20th International Petroleum and Natural Gas Congress and Exhibition of Turkey, May 27-29, 2015 Ankara, Turkey.
- **Polat A.**, and Örmeci C., 2012: The Determination of Hydrocarbon Seepages by Using Landsat TM Satellite Images nearby Adiyaman. 8th International Soil Science Congress - Land Degradation and Challenges in Soil Management, May 15-17, 2012 Cesme-Izmir, Turkey.